Design of an Adaptive Transmitter for a Small Satellite in the Medium Earth Orbit

A thesis accepted by the Faculty of Aerospace Engineering and Geodesy of the University of Stuttgart in partial fulfillment of the requirements for the degree of Doctor of Engineering Sciences (Dr.-Ing.)

Submitted by

M. Sc. Susann Pätschke

born in

Lübeck, Germany

Main-referee: Hon.-Prof. Dr. Christoph Nöldeke

Co-referee: Prof. Dr. Sabine Klinkner

Co-referee: Prof. Dr. Stephan ten Brink

Day of examination: 27.01.2023

Institute of Space Systems

University of Stuttgart

2023

Contents

List of Figures

List of Tables

List of Abbreviations

ACM	Adaptive Coding and Modulation
ACP	Accelerator Coherency Port
ADC	Analogue to Digital Converter
ASIC	Application-Specific Integrated Circuit
ASM	Attached Synchronization Marker
ASTOS	Analysis, Simulation and Trajectory Optimization Software for Space Applications
AWG	Arbitrary Waveform Generator
AWGN	Additive White Gaussian Noise
AXI	Advanced eXtensible Interface
BBFRAME	Baseband Frame
BBHEADER	Baseband Header
BCH	Bose, Chaudhari and Hocquenghem
BER	Bit Error Ratio
BPSK	Binary Phase Shift Keying
BRAM	Block Random Access Memory
CAD	Computer Aided Design
CADU	Channel Access Synchronization Unit
CCM	Constant Coding and Modulation
CCSDS	Consultative Committee for Space Data Systems
CME	Coronal Mass Ejection
CNES	Centre National d'Études Spatiales
COTS	Components Off-the-Shelf
CSI	Channel State Information
DAC	Digital to Analogue Converter
DCO	Data Clock Output
DD	Displacement Damage

DDR	Double Data Rate
DFL	DATAFIELD length
DLL	Dynamic Link Library
DMA	Direct Memory Access
DPD	Digital Pre-Distortion
DSP	Digital Signal Processing
ECC	Error-Correcting Code
EDAC	Error Detection and Correction
EIRP	Equivalent Isotropically Radiated Power
EM	Engineering Model
EMC	Electromagnetic Compatibility
ENOB	Effective Number of Bits
ESA	European Space Agency
EVM	Error Vector Magnitude
FDIR	Failure Detection, Isolation and Recovery
FEC	Forward Error Correction
FEM	Finite Element Method
FF	Flip-Flops
XilFFS	AMD Xilinx fat file system
FIFO	First-In First-Out
FMC	FPGA Mezzanine Card
FPGA	Field Programmable Gate Arrays
FSS	Fixed-Satellite Services
GB	Gigabyte
Gb	Gigabit
GCR	Galactic Cosmic Rays
GEO	Geostationary Orbit
GNSS	Global Navigation Satellite System

GPIO	General Purpose Input Output
GS	Generic Stream
HAP	High Altitude Platforms
HDL	Hardware Description Language
HPBW	Half Power Beamwidth
IBO	Input Backoff
IC	Integrated Circuit
IEEE	Institute of Electrical and Electronics Engineers
IF	Intermediate Frequency
IO	Input/Output
IP	Intellectual Property
IRS	Institute of Space Systems, German: Institut für Raumfahrtsysteme
ISI	Intersymbol Interference
ISS	International Space Station
ITU	International Telecommunication Union
JTAG	Joint Test Action Group
LDPC	Low Density Parity Check
LEO	Low Earth Orbit
LET	Linear Energy Transfer
LHCP	Left Hand Circular Polarization
LO	Local Oscillator
LTAN	Local Time of the Ascending Node
LUT	Look-Up-Table
LVDS	Low-Voltage Differential Signaling
MAL	Malaysia ground station
MBU	Multi Bit Upset
MCD	MODCOD
MEO	Medium Earth Orbit

MER	Modulation Error Ratio
MGT	Magnet Torquer
MLFMM	Multilevel Fast Multipole Method
MM2S	Memory-Mapped to Stream
MMCM	Mixed-Mode Clock Manager
MODCOD	Modulation and Coding
MOM	Method of Moments
MOSFET	Metal Oxide Semiconductor Field-Effect Transistors
NASA	National Aeronautics and Space Administration
NCO	Numerically-Controlled Oscillator
OBC	On-Board Computer
OBDH	On-Board Data Handling
OBO	Output Backoff
PA	Power Amplifier
PAE	Power Added Efficiency
PCB	Printed Circuit Board
PCDU	Power Control and Distribution Unit
PER	Packet Error Rate
PG	Power Good signal
PL	Programmable Logic
PLFRAME	Physical Layer Frame
PLL	Phase-locked Loop
PO	Physical Optics
PROM	Programmable Read-Only Memory
PS	Processing System
PSK	Phase Shift Keying
PTME	Packet Telemetry Encoder
QEF	Quasi-Error Free

QPSK	Quaternary Phase Shift Keying
RAAN	Right Ascension of the Ascending Node
RAM	Random Access Memory
RF	Radio Frequency
RHCP	Right Hand Circular Polarization
RMS	Root Means Square
ROMEO	Research and Observation in the Medium Earth Orbit
RRC	Root Raised Cosine
RS	Reed-Solomon
RTL	Register Transfer Level
S2MM	Stream to Memory-Mapped
SAA	South Atlantic Anomaly
SCaN	Space Communications and Navigation
SCCC	Serially Concatenated Convolutional Code
SE	Spectral Efficiency
SEB	Single Event Burnout
SEE	Single Event Effects
SEFI	Single Event Functional Interrupt
SEGR	Single Event Gate Rupture
SEL	Single Event Latchup
SEP	Solar Energetic Particles
SET	Single Event Transient
SEU	Single Event Upset
SNORE	Signal to Noise Ratio Estimation
SNR	Signal to Noise Ratio
SOF	Start of Frame
SPE	Solar Particle Event
SRAM	Static Random Access Memory

SRRC	Square Root Raised Cosine
SSO	Sun-Synchronous Orbit
SSPA	Solid State Power Amplifier
STR	Stuttgart ground station
TC	Telecommand
TID	Total Ionizing Dose
TMR	Triple-Modular Redundancy
TWTA	Travelling Wave Tube Amplifiers
UHF	Ultra High frequency
UTD	Uniform Theory of Diffraction
VCM	Variable Coding and Modulation
VCO	Voltage Controlled Osillator
VHDL	Very High Speed Integrated Circuit Hardware Description Language
VHF	Very High Frequency
WLAN	Wireless Local Area Network
XFECFRAME	Complex FECFRAME
XTra-Pro	X-band Transmit Processor

List of Symbols

α	roll-off
a	semi-major axis
A_{cloud}	clouds attenuation
A_{gas}	gas attenuation
A_{rain}	rain attenuation
A_{total}	total atmospheric attenuation
B	bandwidth
C	Channel capacity
C/IM	intermodulation distortion ratio
C/IM3	third order intermodulation distortion ratio
c_0	velocity of the electromagnetic wave in free space
D	parabolic reflector diameter
d_x	distance between the patches in x-direction
d_y	distance between the patches in y-direction
e	eccentricity
E_b/N_0	Energy per bit to noise power density
ϵ_{eff}	effective dielectric constant of the substrate
f_c	centre frequency
f_{max}	maximum frequency
f_N	Nyquist frequency
f_r	resonant frequency
G/T	gain to noise temperature, ground station figure of merit
G_{abs}	absolute achievable gain of a patch array
G_R	receiving antenna gain
G_T	transmitting antenna gain
h	satellite altitude
h_S	altitude above sea level

i	inclination
I_{scint}	scintillation impairment
k	Boltzmann constant
k	antenna efficiency
L_a	atmospheric loss
L_{FS}	free space loss
L_S	distance between two antennas
M	number of patches in x-direction
n	number of data bits
ν	true anomaly
N	thermal noise
N	number of patches in y-direction
P_{error}	power of the error
P_R	power at the receiver
$P_{reference}$	error vector at the sampling time of the symbol
P_{signal}	power of the reference vector
P_T	output power at the transmitter
r	number of redundant bits
SNR	Signal-to-noise ratio
T	noise temperature
T_S	Symbol period
Ω	right ascension of the ascending node or longitude of the ascending node
ω	argument of perigee
θ	offset from antenna boresight
λ	wavelength

Acknowledgements

Puh – what a journey! When I started working at the Institute of Space Systems in 2018, I could not have ever imagined all the challenges, adventures, opportunities and projects this decision of pursuing a PhD would lead me. I just knew that I was curious of learning more about satellite communications, diving deep into a specific topic, and having the opportunity to work on all the ideas that came across my mind (this has not changed so much until today though!). Thus, I am so so thankful to Prof. Dr. Sabine Klinkner to ask me more than once if pursuing a PhD would not be the better option than directly starting to work in the space industry. I am thankful for the opportunity of working within the amazing small satellite department of the Institute of Space Systems, being involved in so many different satellite missions and being able to pursue my PhD.

I also want to thank Hon.-Prof. Dr. Christoph Nöldeke for not having the minimum doubt of saying “yes” to supervise my thesis after asking for it during my first month and to be my main referee. Special thanks for all the discussions and advices during the whole PhD and for providing me with so valuable feedback during the writing process. It was always a pleasure to also talk about our love for the northern countries and our language learning progresses.

Furthermore, I´d like to thank Prof. Dr. Stephan ten Brink for being my co-referee and providing the fastest feedback and responses.

I had such a great time at the Institute of Space Systems since I had the privilege to work with the best colleagues I could have ever imagined. Thanks for all the great discussions, for the coffee breaks, for all the activities we did outside of work, for making the Institute such a great place of work. Thanks to Jona Petri for our mutual motivation and discussions during our

traditional coffee and tea break. Thanks to Jonas Burgdorf for being the coolest office colleague that always matched my bad and good sense of humor and with whom I could always share beautiful ground station pictures and never feel weird about it. Thanks to Andreas Pahler for being not only an amazing colleague but also one of the best friends I could imagine. And generally, a big thank you to the whole small satellite department at the Institute.

Furthermore, this thesis was supported by many students writing their thesis about a specific topic of the transmitter, about one of the other thousands of projects I was involved, and helping me designing and building a new ground station – thanks for letting me show you the beautiful world of SatCom! I want to specially thank Lena Bötsch-Zavřel for supporting me with the antenna simulations, Lukas Kramer for supporting me with the prototype, and Patrick Keil for supporting me with the Zedboard testing setup.

Of course, there were many more people providing support and encouraging me during the whole PhD journey. I want to thank Mamen for our weekly calls, for always encouraging me to pursue my passion and to give this passion back to motivate and mentor others. I want to thank my parents for never having any doubt in me and for coming all the way from Spain to my defense! And last but not least I want to thank my partner Sandro. Thanks for supporting me during this intense journey – it was not only the PhD, it was all the other satellite projects, volunteering/mentoring activities and even co-founding a startup and you never had the minimum doubt and even encouraged me to run the extra mile. Definitely the biggest thank you goes to you!

Abstract

The volume of data generated by satellites, especially small satellites and CubeSats in the Low Earth Orbit, has drastically increased in the last years. Yet, the limited available RF bandwidth as well as limited resources on small satellite platforms limit the volume of data that can be sent. Thus, adapting the transmission to the current state is considered key since it offers a high level of flexibility.

The focus of this thesis lies in the design of an adaptive transmitter system for a small satellite mission whose orbit changes over the mission time. The adaptive transmitter operates in the 10.45-10.5 GHz frequency range with 50 MHz bandwidth. The design of the adaptive transmitter also includes the interaction between the space and the ground segment. In order to optimize the adaptive transmitter, different transmitter architectures, components for the digital and the analogue part, digital signal processing implementations and simulations for the power amplifier module and the antenna are investigated. This comprises the link budget analysis to determine the required Equivalent Isotropically Radiated Power considering the used protocols and standards as well as the evaluation of the link performance in terms of data throughput based on the respective orbit analysis.

The different tests for the digital signal processing implementation, for the analogue frontend prototype and for the whole transmitter chain, as well as the evaluation of signal distortions and non-linearities introduced by the analogue components show the feasibility of such an adaptive transmitter for small satellite applications.

Kurzfassung

Das erzeugte Datenvolumen von Satelliten, insbesondere von Kleinsatelliten und CubeSats in der erdnahen Umlaufbahn, hat in den letzten Jahren drastisch zugenommen. Die begrenzt verfügbare HF-Bandbreite sowie die begrenzten Ressourcen auf kleinen Satellitenplattformen begrenzen jedoch das Datenvolumen, das gesendet werden kann. Daher wird die Anpassung der Übertragungsparameter an den aktuellen Zustand als Schlüsseltechnologie angesehen, da dies ein hohes Maß an Flexibilität bietet.

Der Schwerpunkt dieser Arbeit liegt auf dem Entwurf eines adaptiven Sendersystems für eine Kleinsatellitenmission, deren Umlaufbahn sich im Laufe der Missionszeit stark ändert. Der adaptive Sender arbeitet im Frequenzbereich von 10.45-10.5 GHz mit einer Bandbreite von 50 MHz. Der Entwurf des adaptiven Sendersystems umfasst auch die Interaktion zwischen dem Raum- und dem Bodensegment. Um den adaptiven Sender zu optimieren, werden verschiedene Senderarchitekturen, Komponenten für den digitalen und den analogen Teil, digitale Signalverarbeitungsimplementierungen für die adaptive Anpassung und Simulationen für das Leistungsverstärkermodul und die Antenne untersucht. Dies umfasst auch die Link-Budget-Analyse zur Bestimmung der erforderlichen äquivalenten isotropen Strahlungsleistung unter Berücksichtigung der verwendeten Protokolle und Standards sowie die Bewertung der Link-Performance in Bezug auf den Datendurchsatz auf der Grundlage der jeweiligen Orbitanalyse.

Die verschiedenen Tests für die digitale Signalverarbeitungsimplementierung, für den analogen Frontend-Prototyp und für die gesamte Senderkette sowie die Bewertung der durch die analogen Komponenten verursachten Signalverzerrungen und Nichtlinearitäten zeigen die Machbarkeit eines solchen adaptiven Senders für Kleinsatellitenanwendungen.

xxx

1 Introduction

The last decades have seen an unparalleled growth in the number of launched satellites, especially for small satellite and CubeSat missions. This growth comes with the increased need for efficient data transmission, mainly in Low Earth Orbit (LEO). The enormous growth in the amount of data to be transmitted requires a significant increase in the transmission capabilities for those small satellite platforms. However, these platforms have limited available resources like mass, volume and power. Increasing parameters such as Radio Frequency (RF) power, antenna size, bandwidth and carrier frequency is challenging. Furthermore, the robustness and the reliability of the entire platform should be comparable to satellites with bigger platforms. To overcome these challenges, the use of adaptive transmission has been analysed. It is shown that it allows a greater data throughput and thus, higher mission return of a satellite mission. The success of a satellite mission characterizes the mission return, which is often linked to the quantity of data received.

Jeremiah F. Hayes proposed the first concept of adaptive transmission in 1968 [1]. Here, the channel state information (CSI) defines the transmission parameters, such as modulation, code rate and power. A feedback channel sends the received signal's CSI back to the transmission system, which then adapts its transmission parameters based on the CSI feedback. Examples of applications that use adaptive transmission nowadays are Wireless Local Area Network (WLAN) [2] and Satellite News Gathering [3]. These applications typically use established standards like the Digital Video Broadcast – Second Generation (DVB-S2). The classic DVB-S2 use case is for television and data broadcasting services, mainly from a satellite located in a geostationary orbit (GEO) to one or multiple end-users. Several studies showed the performance of

this use case based on different parameters. These comprise different geographical areas of the end-user [4], the rain influences [4]–[10], the Ka-band [5], [7], [9]–[11] and the Ku-band [8], [11] as well as the newer DVB-S2X standard [10]. On the basis of these studies, the International Telecommunication Union (ITU) recently developed the Recommendation ITU-R S.2131 [12], which is suitable for satellite systems using adaptive transmission [9]. But, this recommendation only is applicable to fixed-satellite services (FSS), i.e. GEO satellite applications, and to transmission systems above 20 GHz.

Non-GEO satellites applications, compared to GEO satellite applications, rarely use adaptive transmission. One example using the DVB-S2 standard is the satellite constellation of Planet [13]. Different case studies showed the potential of using adaptive transmission. These use cases cover LEO [13]–[23], Medium Earth Orbit (MEO) [24]–[27] and GEO [4]–[11], [28], [29] orbits. They cover different applications like airplanes [30], drone delivery [26] and high altitude platforms (HAP) [31]. Adaptive transmission is under test by various agencies, for example, National Aeronautics and Space Administration (NASA) with its Space Communications and Navigation (SCaN) program on the International Space Station (ISS). Here, NASA tested various adaptive transmissions schemes that are effective and compatible with their ground station network [17].

A recommendation for adaptive transmission currently does not exist for non-GEO satellite applications. Thus, the following issues are of interest:

- How can non-GEO satellite systems be adapted to adaptive transmission standards mainly defined for GEO use cases?
- What are the interdependencies for the different parameters? For example, orbit, dynamic properties of the link budget parameters, and frequency band?

- How do the space segment and ground segment interact during nominal operation?
- How does the adaptive transmission of payload data influence the reliability of telemetry and telecommand links?
- Is adaptive transmission always the most efficient solution?
- How can the feedback channel be implemented?
- How can the complexity of adaptive transmission be limited for small satellites? For example, regarding the geographical area of the ground segment, used protocol standard or satellite application?

This thesis on an adaptive transmission system concentrates on these questions. It assumes a 60 kg satellite mission whose orbit changes over the mission time. The main focus lies in defining the architecture of the transmission system. This includes the satellite's transmission system but also the receive function of the ground segment. It also includes the implementation of the digital part assuring adaption to the current transmission conditions. This transmission system is derived from a generic, non-mission specific architecture for adaptive communication. Still, the space environment with its thermal and radiation constraints affects the design process.

1.1 Constraints due to the space environment

The use of Components Off-the-Shelf (COTS) hardware and software in the space environment is not straightforward. Also, other restrictions pose a number of challenges.

A key design driver is the launch cost since it increases the higher the volume and the mass of the satellite is. This limits the mass, volume, and power resources on small satellite platforms. Furthermore, it is not possible to replace hardware once the satellite is in orbit. In the space environment, satellites

experience an exposure to a wide temperature range. Due to the lack of atmosphere and gravitation, heat transfer can only be done by conduction within the satellite and radiation into space since there is no heat convection. The thermal subsystem must ensure that all components are only exposed to their given operational temperature range. Tests in the thermal vacuum chamber ensure that components function in the expected temperature ranges and in vacuum. Furthermore, the components have to withstand the mission specific radiation environment. Ionizing radiation can degrade or lead to malfunctions or failure of electronic components. In the worst case it can even lead to mission loss.

A satellite is expensive, especially when space qualified components are used. However, these components are less power efficient and less flexible compared to COTS components. Yet, technological progress leads to advantages in various electronic components. For example, the integration density allows combining many functions onto a smaller single integrated circuit (IC). Also, the processing power of Field Programmable Gate Arrays (FPGA) and System on a Chip (SoC) is increasing continuously. Thus, design complexity reduction and more flexibility in the digital domain is possible.

The use of lightweight and highly integrated components cuts satellite mass and launch cost. Furthermore, it reduces design complexity, volume and power resources. But any malfunction or the failure has a higher negative impact on the platform, since they host several functions that could lead to the loss of the mission. Another risk is due to radiation. Electronic components can degrade due to ionizing radiation. The quantity of absorbed radiation is quantified by the total ionizing dose (TID), that generates a cumulative long-term ionizing damage due to protons and electrons. Typical TID effects are quasi-permanent device shifts, increased device leakage and power consumption, changes in timing, which can all lead to functional failure. Furthermore, single event effects

(SEE) cause instantaneous errors of the component. These can also lead to immediate loss of the component. Yet, an increase in robustness, both in hardware and in software, is possible. The use of shielding mitigates the risk of destructive latch-ups and memory upsets as well as the TID. Redundancy of components is also a method to mitigate the radiation risk if one of the components fails. However, redundancy is a significant cost and mass driver. Thus, a well-thought-out risk management is essential. Triple-modular redundancy (TMR) and configuration memory scrubbing are effective software SEE mitigation methods.

1.2 Overview and trends of adaptive transmission for space applications

The small satellite market has changed dramatically in the last decade. Euroconsult released in April 2021 a report [32] about the prospects of this market and in December 2021 a report analysing the satellites to be launched and built by 2030 [33]. Euroconsult expects more than 17000 launched satellites until 2030. This represents more than a fourfold increase compared to the decade from 2011 till 2020. This leads to 39% more satellite industry revenues for the decade 2021-2030 (320 billion $) than for the decade 2011-2022 (230 billion $). From these 17000 satellites, 81.8% are small satellites with a mass below 500 kg [32]. The authors of the reports conclude that the “satellite sector no longer evolves around the axis of New Space entrants challenging established legacy players. Instead, it has now shifted towards speed, and the ability to rapidly provide commercial services. New Space is no longer the driving force in the industry. It’s all about Fast Space now”[34]. Yet, Fast Space leads to several questions: how can a mission become more efficient, low-cost but competitive, faster by using technologies that were not particularly popular in the space sector up to now? And what risks can be the consequence of this trend?

This perspective leads to different implications for satellite transmission systems:

- The need for a disruptive technology shift towards producing at reduced satellite volume, mass, production time and cost
- No structured or qualified standard for “New Space” or “Fast Space” satellite hardware development
- Demanding payload requirements increase the need for high data rate transmission. This involves offering more flexibility, wider bandwidth, and bandwidth-efficient modulation and coding schemes. Key challenges are the development of power amplifiers, wider bandwidth devices, flexible components, reconfigurable digital signal processing as well as reconfigurable antennas. A well-thought combination of existing and emerging technologies can increase the mission and payload flexibility and the mission-return [35]
- The transmission system must ensure full functionality even under worst case conditions. This implies lower data throughput compared to the nominal or even the most favourable transmission conditions. Hence, the exploitation of the span between the worst and best case is not possible
- The advances in monolithic integration allow to perform more functions of the transmission system in the digital domain. This allows more flexibility and thus, increasing the data throughput. Furthermore, FPGAs or SoCs can perform functions that previously only were possible with complex analogue hardware. By shifting complex functions into the digital domain, the digital to analogue interface is shifted closer to the antenna. Hence, choosing the digital to analogue converter (DAC) and the following power amplifier takes special attention to not counteract the advantages digitalisation offers

These implications show that a significant improvement in the mission return is possible when using adaptive transmission. Yet, there is not a valid recommendation for non-GEO satellites and the adaptive transmission requires more complexity.

1.3 Aim of the thesis

The aim of this thesis is to design an adaptive transmitter system for a small satellite, which is capable to adapt to the current transmission conditions and to withstand the harsh space environment with its thermal, vacuum and radiation effects. The design of the architecture includes the interaction between the space and the ground segment. The software's flexibility should maximize the data throughput without reducing the system's efficiency. This thesis focuses on the following tasks:

- Definition of the overall architecture for the adaptive transmission system including space and ground segment and their interaction
- Definition of the adaptive transmitter high-level architecture based on the presented mission use case
- Link budget analysis to determine the required Equivalent Isotropically Radiated Power (EIRP) in connection with the used protocols and standards
- Evaluation of the adaptive transmitter link performance in terms of data throughput based on the respective orbit analysis
- Definition and analysis of different adaptive transmitter designs, including the influence of the analogue frontend with the linearity of its amplifier(s) and the antenna options
- Definition and implementation of the digital signal processing algorithms, which allow an adaptive transmission to the current link conditions

- Testing of the adaptive transmission system including the digital signal processing as well as the evaluation of signal distortions and non-linearities introduced by the analogue components
- Analysis of the concept to prove the feasibility of such an adaptive transmission system for small satellite applications

Chapter 2 gives an overview of the satellite communication channel. In this chapter various transmitter architectures and advantages of an increased digital implementation are examined. Moreover, different adaptive transmission protocols and standards as well as relevant link parameters and their influence on the link are presented.

Chapter 3 includes the use case, which is based on the ROMEO mission of the University of Stuttgart, with the derived requirements and constraints for the transmission system. Moreover, a detailed link budget analysis is performed in order to determine the influence of the atmosphere within the signal path and the minimum required EIRP. In this chapter a parametric link budget analysis for different parameters (orbit type, frequency band, atmospheric influence, noise influence and mutual interdependencies), and an adaptive transmission assessment is included. Lastly, the interaction of the space and the ground segment is defined.

In Chapter 4 the design of the adaptive transmission system is described. A high-level architecture overview is given before explaining the detailed architecture of the different subsystems in more detail.

In Chapter 5 the testing and verification of the designed and developed adaptive transmission system are described. This includes the evaluation of the chosen components on a prototype, the evaluation of the implemented software as well

as a test of the breadboard chain. Lastly, the test and measurement results are discussed.

Finally, Chapter 6 contains the conclusion and provides an outlook on possible further investigations. Moreover, the next steps required to build a system for the envisaged use case are outlined.

2 Transmission systems for space applications

The increased amount of data generated by satellites requires higher data rates for the communication link. Yet, the transmission should be as efficient as possible over the limited available bandwidth. The information rate (the bit rate at the input of the Forward Error Correction (FEC) encoder), e.g., the maximum throughput, over a given bandwidth is defined as spectral efficiency. The limited bandwidth implies ever more stringent demands and requirements for the transmission system components to achieve the maximum possible data throughput. In this chapter a generic communication channel between a transmitter and a receiver is described. Furthermore, state-of-the art technologies for transmitters are introduced. Also, an overview of the adaptive transmission standards and the influence of the relevant link parameters is given.

2.1 Communication channel

Figure 2-1 shows a generic communication system. It consists of three components: the transmitter, the transmission channel and the receiver. The transmitter encodes the data and then transports it through the transmission channel. The transmission channel presents various noise sources and other impairments like interference or multipath propagation that can corrupt the data. The receiver decodes the received data. The term channel capacity C is defined as the maximum rate over a communication channel at a defined bandwidth under the presence of noise. Shannon defined the channel capacity C with the following equation [36]:

$$C = B \cdot \log_2(1 + SNR) \qquad \textit{Eq. 2-1}$$

where C is the channel capacity excluding the error correction codes, expressed as bits per second; B is the bandwidth of the channel, expressed in Hertz; and SNR is the signal-to-noise ratio over the bandwidth, expressed as a power ratio. Considering a bandwidth of 10 MHz and a SNR of 0.7, the channel capacity is 7.66 Mbps. *Eq. 2-1* shows that the higher the SNR and the more available bandwidth, the higher the possible data rate. It defines the theoretical maximum data amount that can be transmitted over the channel without errors, which is not fully achieved in practice. *Eq. 2-1* does not make any limitation on the lowest achievable error rate, which depends on the used encoding scheme. With *Eq. 2-1*, the minimum required SNR for the data transmission can be calculated. This minimum is known as the Shannon limit and occurs as the available bandwidth goes towards infinity:

$$\frac{E_b}{N_0} = -1.6 \text{ dB} \qquad \text{Eq. 2-2}$$

where E_b is the energy per bit and N_0 is the noise power density in Watts/Hz. If E_b/N_0 is below -1.6 dB, there does not exist any modulation or FEC scheme allowing data transmission. This -1.6 dB limit only applies for the theoretical case of infinite bandwidth. The Shannon limit for signals with finite bandwidth is always higher. Advanced FEC encoding schemes nowadays allow operation close to the Shannon limit. Yet, this comes at the expense of higher computational performance requirements and complexity.

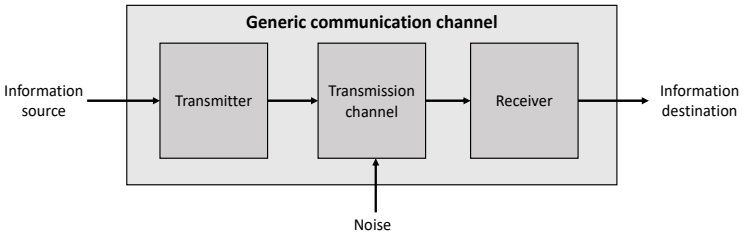

Figure 2-1: Generic communication system with transmitter, transmission channel and receiver

Filtering is a key process to be able to recover the data sent by the transmitter. Nyquist's theory describes the optimum signal filtering. When pulse shaping (baseband, without modulation) is used, intersymbol interference (ISI)-free transmission is possible by using a rectangular bandpass filter that corresponds to the minimum required bandwidth. This so-called Nyquist bandwidth is the inverse of the symbol period T_S. The Nyquist frequency is denoted as f_N and is defined as:

$$f_N = \frac{1}{2T_S} \qquad \textit{Eq. 2-3}$$

Yet, a filter with sharp transitions in the frequency domain is difficult to realize. In radio transmission, i.e., in RF modulated signal transmission, Nyquist filtering is distributed between the transmitter and at the receiver to limit the interference of out-of-band carriers. This is done by processing the transmitted signal with a square root raised cosine filters (SRRC) and applying the same filter in the receiver. ISI-free transmission is possible with filters that have smoother transitions in the frequency domain, fulfilling the Nyquist criteria. The bandwidth needed depends on the roll-off factor α as expressed in Eq. 2-4.

$$B = \frac{1+\alpha}{T_S}\,[Hz] \qquad \text{Eq. 2-4}$$

This equation is valid for modulated signals. If $\alpha = 0$, Eq. 2-4 is identical to *Eq. 2-3* since $B = 2f_N$. The roll-off factor determines the steepness of the frequency response. The case $\alpha = 0$ refers to a "brick wall" filter with amplitude 1 up to f_N and zero amplitude above f_N. When $0 \leq \alpha \leq 1$, a smaller α leads to a steeper filter edge and occupies less bandwidth. Yet, a smaller α, due to the steepening filter edge, leads to larger unwanted overshoots, that can lead to errors in the demodulation. The flatter edge for higher values leads to a faster decaying impulse response, with the disadvantage of bandwidth increase.

The progress in digital technologies allows to transfer part of the signal processing into the digital domain. This increases the possibility to replace analogue components with digital signal processing taking place in a processor, an FPGA, an Application-Specific Integrated Circuit (ASIC) or a SoC (which combines processor and FPGA). This reduces the complexity of the analogue part of the transmitter. Moreover, due to the use of less analogue components, the size of the transmitter is reduced. This increased use of the digital signal processing capabilities is achieved by moving the DAC closer to the power amplifier (PA) which reduces the number of analogue components used.

By moving more functions into the digital domain, more emphasis has to be taken on the sampler, in the transmission a DAC, that performs the sampling of the signal. Sampling is the process where a continuous signal is represented by a sequence of discrete data values. Signals have to be sampled in a way that the integrity of the signal is preserved. This is valid for digital to analogue conversion as well as for analogue to digital conversion. The selection of a sampling rate affects the reconstruction of the signal, the sampling rate has to be sufficiently high to assure the signal integrity but sufficiently low to relax the requirements for the sampling components. The Nyquist-Shannon sampling theorem defines the minimum required sampling rate that allows reconstructing the signal.

This theorem states that if the spectrum of a continuous real signal is symmetrical with respect to 0 Hz the spectral amplitude is zero above $+f_{max}$ and below $-f_{max}$ (which means that the signal is bandlimited to the maximum frequency value of a $\pm f_{max}$), the signal has to be sampled at a sampling rate f_S that is higher than or equal to twice the maximum frequency of the signal [37]:

$$f_S \geq 2f_{max} \qquad \text{Eq. 2-5}$$

If the sampling rate is much higher than needed, for example four times above the maximum frequency of the signal, the signal is said to be oversampled. The higher the needed sampling rate, the higher the requirements for the DAC. The parameters that determine the characteristics of a DAC are the following:

- Resolution: the number of output levels the DAC or Analogue to Digital Converter (ADC) is able to reproduce. The resolution is given as the binary logarithm of the number of levels, which then states the number of bits. For example, a DAC with a resolution of 8 bits has 2^8-1 possible output levels
- Effective Number of Bits (ENOB): the actual resolution. Due to quantization noise, non-linear characteristics as well as gain and offset errors, the actual resolution is reduced
- Maximum sampling rate
- Dynamic range: defines the range of signals a DAC can reproduce

In order to relax the DAC requirements, another sampling technique known as bandpass sampling can be used [38]. Bandpass sampling is used for sampling a continuous bandpass signal that is not centred at 0 Hz but at a centre frequency f_C. Consequently, the sampling rate is determined by the signal bandwidth and not by its highest frequency. In the frequency

spectrum, the original continuous bandpass signal is amended by a negative frequency component of the signal centred at $-f_C$ which is the mirror image of the positive frequency component. By sampling with a lower sampling rate, it is possible to use these spectral replicates avoiding to sample the signal at sampling rates at or above twice the maximum frequency f_{max}. An ideal sampling device like a DAC generates signal replicas at multiples of the sampling rate f_s, $2f_s$ … mf_s, where m is an integer number. The replicated spectra of the signal that are generated by the DAC are present at $-mf_S + f_C$ and the mirrored replicas at $(m + 1)f_S - f_C$. The replicated spectra of the signal are shown in *Figure 2-2*, for different bandpass sampling rates.

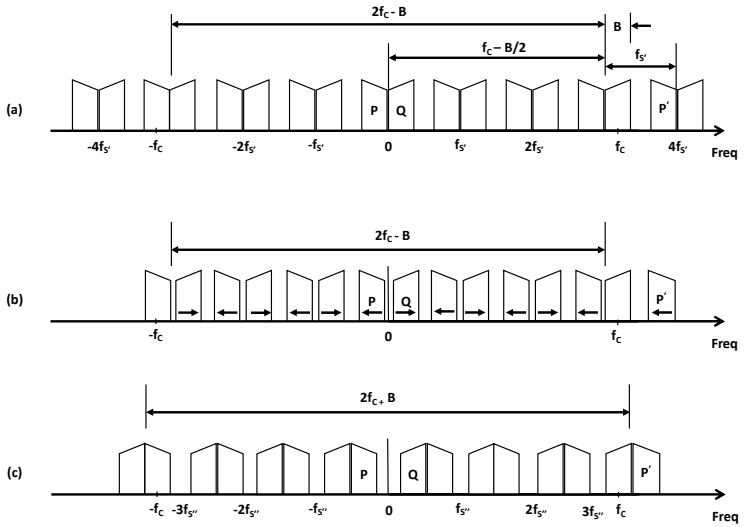

Figure 2-2: Bandpass sampling frequency limits: a) sample rate $f_{s'}=(2f_cB)/6$; b) sample rate less than $f_{s'}$; the arrows indicate the direction in which the replica shift if the sample rate is less than $f_{s'}$; c) minimum sampling rate $f_{s''}<f_{s'}$ [38]

The overlapping of the signal replicas is called aliasing. In order to choose a sampling rate where aliasing does not occur, the sampling rate limits have to be determined. By determining these limits, it is possible to sample a continuous signal at a sampling rate so the spectral replications of the positive and the negative bands, P and Q just butt against each other at baseband, e.g. at 0 Hz. In the range of $2fC$ − B, fS' can be defined as:

$$f_{S'} = \frac{2f_c - B}{m} \qquad \text{Eq. 2-6}$$

where B is the bandwidth and m is an arbitrary, positive integer describing the number of replication while ensuring the Nyquist-Shannon criterion: $f_s \geq 2B$. By increasing the sampling rate fS', the original spectrum of the signal does not change while the replicas will shift. At 0 Hz, the P band will shift to the right and the Q band shift to the left and overlapping and aliasing occur. By decreasing the sampling rate below fS', the P and the Q bands shift. Consequently, a range for the sampling rate results which guarantees to avoid aliasing is defined in the following equation, while still satisfying the Nyquist criterion $fs > 2B$:

$$\frac{2f_c - B}{m} \geq f_{S'} \geq \frac{2f_c + B}{m + 1} \qquad \text{Eq. 2-7}$$

Figure 2-3 shows the regions of acceptable bandpass sampling rates. Note that if m = 0, the acceptable bandpass sampling rate is equal to Eq. 2-5.

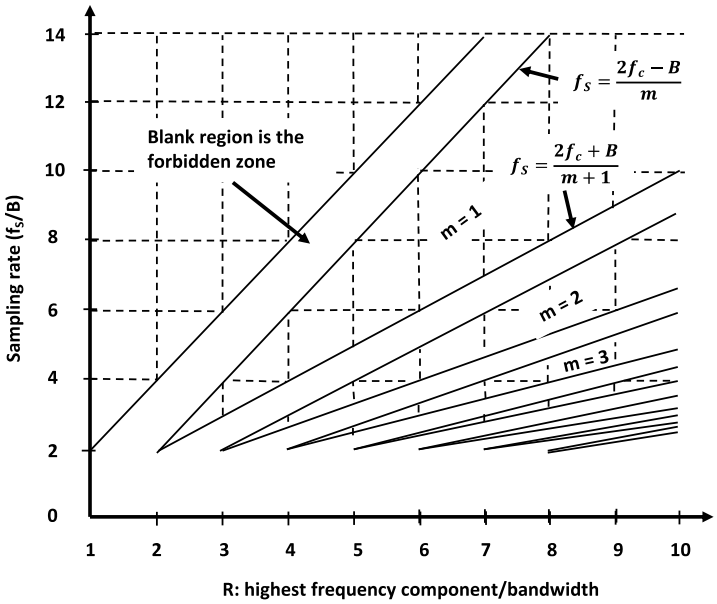

Figure 2-3: Regions of acceptable bandpass sampling rates from Eq. 2-7*, normalized to the sampling rate over the signal bandwidth (f_S/B) [38]*

2.2 Transmitter architectures

A transmitter is a component that radiates radio waves modulated with data. This term often also includes the antenna which radiates the radio waves. The data is split into two streams, the in-phase (I) and the quadrature (Q) component. Then, the digital I and Q signals are filtered with an SRRC filter. This filtering limits the amount of needed bandwidth to transmit the data. These filtered signals are then modulated on a carrier, the local oscillator (LO) generates two tones that are shifted 90° w.r.t. each other. The modulated I and Q signals are superimposed. This I/Q modulated signal at LO frequency can be upconverted in one or two steps. The signal can directly be upconverted to the desired RF frequency or the signal can be

upconverted first to an intermediate frequency (IF) and then to the desired RF frequency. The unwanted mixing products are filtered out and finally the signal is amplified. This signal is sent through an antenna over the transmission channel.

The digital to analogue conversion can be performed at several positions in the transmitter architecture. *Figure 2-4* shows the different possible positions of the DAC. The more the DAC is placed to the right in *Figure 2-4*, i.e. closer to the RF output, the more amount of signal processing can take place in the digital domain. On the other hand, the signal frequencies become higher towards the output and the faster the digital signal processing has to operate. This means that a higher sampling rate is necessary. Independent of the DAC position, the DAC has to provide sufficient resolution to achieve a high ENOB in order to overcome the quantization noise. In the following subsections, the different locations for the digital to analogue conversion are discussed with the respective requirements for the DAC.

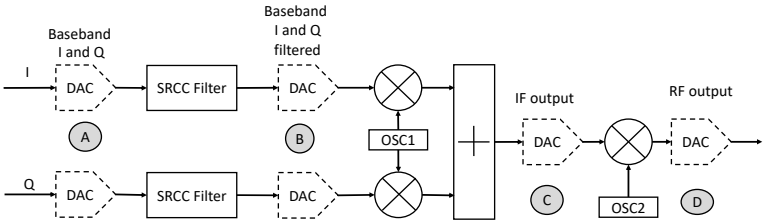

Figure 2-4: Alternative DAC positions for a transmitter

2.2.1 DAC before SRRC filter (A)

Here, the DACs are positioned directly after the data is split into I and Q channels. The requirements for the DAC characteristics on sampling rate are low. Yet, almost all signal processing (filtering, modulation and combination of I and Q channels) takes place in the analogue domain. An SRRC filter in the analogue domain is quite complex and the possible synchronization mismatch between the two DACs and mixers can cause I/Q offset and I/Q timing errors. Since this option does not allow to implement complex digital signal processing it is not considered further.

2.2.2 Zero-IF transmitter – analogue baseband (B)

In the position (B) the DAC is placed after the SRRC filter and before the first mixer stage. This architecture is also known as heterodyne zero-IF transmitter. Despite for the SRRC filter, all signal processing is performed in the analogue domain. Since the SRRC filters are transferred to the digital domain, the requirements of the DAC characteristics regarding sampling rate are still low but increased compared to (A). The possible synchronization mismatch between the two DACs and mixers can cause the same impairments as in (A) and reduce the signal quality if these become too large.

2.2.3 Low-IF transmitter – digital baseband (C)

Here, the DAC is placed after the combiner. This architecture is also known as low-IF transmitter. In this architecture the first oscillator (OSC1) is implemented in the digital domain, compared to the architecture in A and B. This type of oscillator is called numerically-controlled oscillator (NCO) and it creates a synchronous, discrete-time sinusoidal signal. This architecture requires a single DAC but the requirements on sampling rate are higher than for the zero-IF case. Since the IF can be hundreds of MHz or even several GHz, the sampling rate requirement is more difficult to fulfil. For example, if an IF of

1500 MHz is desired, the minimum sampling rate of the DAC has to be 3 Gsps. Furthermore, since the mixing and combination of the I and the Q channel is performed in the digital domain, mismatch between the I and Q channels is not present and other impairments like I/Q phase offset, I/Q timing errors are negligible. The requirements on the digital circuitry regarding complexity and digital signal processing speed increases w.r.t. the zero-IF transmitter.

2.2.4 At RF signal – direct transmitter (D)

The last possible location is positioning the DAC after the upconverter which converts the signal to the desired RF frequency. Here, all signal processing is performed in the digital domain. No analogue components before the PA are needed except for the DAC and a subsequent bandpass filter. Yet, this architecture has several drawbacks due to the sensitivity to imbalance between the mixer's amplitude and the phase errors of the LO signals and the accuracy of the 90° phase difference. This imbalance leads to LO leakage and reduced suppression of the image frequencies. Furthermore, the requirements on the required sampling rate and dynamic range to convert the signal are the highest. Especially for higher frequencies it can be difficult to find an adequate DAC that fulfills the requirements, especially a sampling rate in the order of several Gsps.

2.2.5 Advantages of an increased digitization

Legacy transmitter systems for space applications are not flexible to changes in operating parameters. This results in mainly two drawbacks. First, an available, standardized transmitter without mission-specific optimization is used. Second, an adaptation of the system quickly leads to long project durations and non-negligible costs for the development and the qualification of the adaptation. Adjustments in orbit are not possible or very difficult to achieve. Since even small errors cannot be corrected afterwards, much effort is put into tests on the ground. Increased digital signal processing

capabilities can counteract these drawbacks allowing more flexibility in the system. This flexibility gives the possibility of adapting the configuration parameters of a transmitter system, even if it is already in space:

- Due to the flexible design it can save costs for repeated use on flight missions
- Risk is minimized by reusing the transmitter system and changing only the digital domain to meet certain and/or new mission requirements
- The selection of carrier frequency, modulation and coding can be done entirely in software. This means that no redesign of the hardware is necessary to change configuration parameters, and the system can be built in a standardized way
- It is possible to react to changing boundary conditions during operation in orbit (like higher slant range, pointing error, atmospheric and rain attenuation, higher data rate requirements)
- Through adaptation to the current link conditions, the mission return can be increased
- It is possible to correct minor errors in the software with a firmware update. This can be done either for the satellite already in orbit or for the use on a new mission
- A completely new software image with a newer and more efficient standard or protocol can be implemented through software updates. This can be done either for the satellite in orbit or for the use on a new mission
- Higher degree of autonomy for the operation of the satellite since the transmitter adapts its current transmission configuration independently of the scheduled satellite operation

2.3 Waveform schemes

Different parameters are necessary to define the way in which the data stream is mapped to the radio signal. The term waveform is often used to refer to the complete parameter set. This includes the modulation, FEC, signal filtering, carrier frequency and polarization (linear or circular). The following subsections describe the parameters digital modulation and FEC in more detail.

2.3.1 Modulation

The term modulation defines the process of modifying a wave parameter to carry information. Modulation is classified according to the modified parameters: amplitude modulation, frequency modulation and phase modulation. Furthermore, mixed modulation schemes like for example combining amplitude and phase modulation are possible. The most important type of digital modulation (thus, implemented in the digital instead of in the analogue domain) for satellite communication is Phase Shift Keying (PSK). A constellation diagram displays the complex baseband signal fed to an IQ modulator in the complex plane as illustrated in *Figure 2-5*.

2.3.1.1 Phase shift keying modulation

PSK modulation is a digital modulation format that only uses the complex phase as the information carrier. Commonly used schemes are Binary Phase Shift Keying (BPSK), quaternary phase shift keying (QPSK) and 8PSK, where 1 bit, 2 bits or 3 bits per symbol are transmitted. This number of bits per symbol transmitted defines the modulation order.

2.3.1.2 Amplitude and phase shift keying modulation

To transmit more information in one symbol and thus to, increase the spectral efficiency, the amplitude can also be modulated in addition to the phase. Yet, the geometric space of the individual points in the constellation diagram becomes

smaller with smaller amplitudes, which increases the receiver requirements for the demodulation process under noise compared to the QPSK signal. Two examples of amplitude and phase shift keying modulation (APSK) are presented in *Figure 2-5*: 16APSK (c) and 32APSK (d). The relation between the concentric rings is described as the ring ratio (γ).

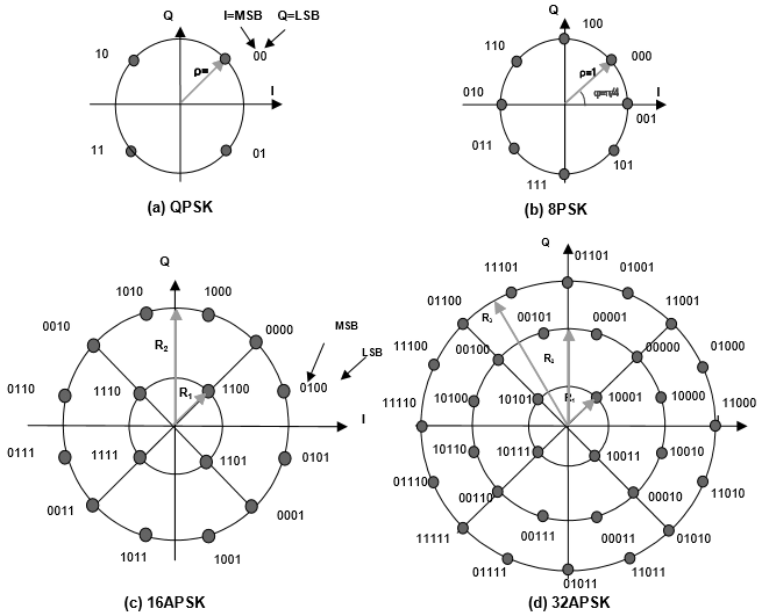

Figure 2-5: Different types of digital modulations. a) QPSK, b) 8PSK, c) 16APSK and d) 32APSK [3]. The ring ratio from the 16APSK modulation is characterized by $\gamma=R_2/R_1$ and the ring ratios from the 32APSK modulation are characterized by $\gamma_1=R_2/R_1$ and $\gamma_2=R_3/R_1$. The values for the ring ratios can be found in [3]

2.3.1.3 Error vector magnitude

The metric Error Vector Magnitude (EVM) evaluates the quality of a digitally modulated signal. It describes the magnitude of the error vector at the sampling time of the

symbol related to the instantaneous amplitude of the reference signal. EVM can be expressed in dB or in % and is directly linked to the SNR, as defined in Eq. 2-8 and Eq. 2-9.

$$\text{EVM [dB]} = 10 \cdot \log_{10} \sqrt{\frac{P_{error}}{P_{reference}}} = \sqrt{\frac{1}{SNR}} \qquad \text{Eq. 2-8}$$

$$\text{EVM [\%]} = \sqrt{\frac{P_{error}}{P_{reference}}} \cdot 100\% \qquad \text{Eq. 2-9}$$

Another parameter that evaluates the quality of a digitally modulated signal is the Modulation Error Ratio (MER). It calculates the ratio of the root mean square (RMS) power of the reference vector (P_{signal}) to the power of the error (P_{error}) as shown in Eq. 2-10:

$$\text{MER } [dB] = 10 \cdot \log_{10} \sqrt{\frac{P_{signal}}{P_{error}}} \qquad \text{Eq. 2-10}$$

If the reference signal power of the EVM is equal to that of the MER, both quantities are interrelated by:

$$\text{MER } [dB] = -20 \cdot \log_{10} \left(\frac{EVM\ (\%)}{100\%} \right) \qquad \text{Eq. 2-11}$$

2.3.2 Forward Error Correction

FEC is used in digital communication links to correct the errors occurring during the data transmission. This is achieved by adding redundant data to detect if the received data

contains errors and, if possible, to correct these errors. The code rate is defined in Eq. 2-12:

$$\text{Code rate} = \frac{n}{n+r} \qquad \text{Eq. 2-12}$$

where r is the number of redundant bits and n the number of data bits. A code rate of 9/10 signifies that for a total of 10 transmitted bits, r = 1 redundant bit is added to the original n = 9 data bits.

Encoding schemes can be divided into block codes and convolutional codes. These also can be combined to concatenated codes.

Block encoding

In block encoding, the encoder adds r bits of redundancy to a block of n data bits; thus, each block is coded independently. The coded bits are generated from a linear combination of the data bits of the corresponding block. Typically, cyclic codes are used where every code word is a multiple of a generating polynomial. Examples for block codes are Reed-Solomon (RS), Bose, Chaudhari and Hocquenghem (BCH) and Low Density Parity Check (LDPC). LDPC codes were already invented in the 1960s but not used until the last two decades due to computational limitations. For further details, see Section 4.3. of [39].

Convolutional encoding

In convolutional encoding, the encoder generates (n + r) bits from the (N - 1) preceding packets of n bits of data. Here, the product N(n + r) defines the so-called constraint length of the code. The encoder consists of shift registers and adders of XOR type. In contrast to block encoding, typically, the entire content of the source data stream is modified. For further details, consult Section 4.3. of [39].

Concatenated encoding

The FEC encoding type is chosen depending on the types of expected errors. The error distribution depends on the noise nature and the transmission propagation impairments. If the channel conditions are stable, errors occur randomly and convolutional encoding is best suited. Yet, the convolutional decoder at the receiver may also fail occasionally which leads to a burst of errors at the output of the decoder. Since for some block codes and some decoding algorithms, block decoders are able to efficiently correct burst errors, concatenated coding schemes combining two different types of encoding are often used. Interleaving is further used with concatenated coding in order to distribute bursts of errors as the output of the inner decoder over different code blocks. Many transmission standards use standard convolutional code as inner code and RS block code as outer code. Others, like the DVB-S2 standard, use two different block codes. The LDPC acts as inner and BCH as outer code. In contrast, turbo codes or serially concatenated convolutional codes (SCCC) concatenate different convolutional codes. The DVB-S2 codes and SCCC both approach the Shannon limit within 0.6 - 1.2 dB [3], [39].

2.4 Space communication protocols and standards

The use of space communication protocols and standards provides several advantages. It promotes global interoperability which results in significant savings in cross support. A well-established standard further reduces complexity and risk. Also, life cycle costs decrease as a result of faster development and testing w.r.t. systems that do not use these standards. Furthermore, the standards are often commercially available as Intellectual Property (IP) cores that can be directly implemented as part of the own design. The following subsections describe the DVB-S2 and the CCSDS 131.2-B-1 standards.

2.4.1 DVB-S2

The Digital Video Broadcasting – Satellite Second Generation (DVB-S2)-Standard is widely used in the transmission of digital television programs via broadcasting satellites. The standard defines a system with which digital information, such as high-definition television programs or interactive services, can be reliably transmitted and received. This is achieved by suitable choices of channel coding, modulation and error correction methods. These procedures are examined in more detail in specification [3].

Figure 2-6 shows a block diagram of a DVB-S2 transmission system from digital up to RF signals. The input data consists, for example, of a coded transport stream, controlled by a protocol for bundled packet-wise transmission of video and audio data. Reliable quasi-error-free (QEF) transmission is guaranteed if the reception quality as quantified by the E_b/N_0 is above a defined threshold.

Mode and stream adaption

The standard allows processing single or multiple input streams, such as for broadcast satellite services that broadcast several TV channels on a single carrier frequency. The input data can be in form of transport stream (TS) data or continuous generic stream (GS) data. For multiple streams, the standard provides modules for dividing and synchronizing the packets to combine them on a single carrier.

A data field with a defined length combines data packets and expands these by an 80-bit long baseband header (BBHEADER). This header contains information on the type of input data including the data format (TS/GS), the number of input streams, the parameters for the synchronization of packets and the roll-off factor. The type of modulation and code rate can be static, also named constant coding and modulation (CCM), variable (VCM) or adaptive (ACM).

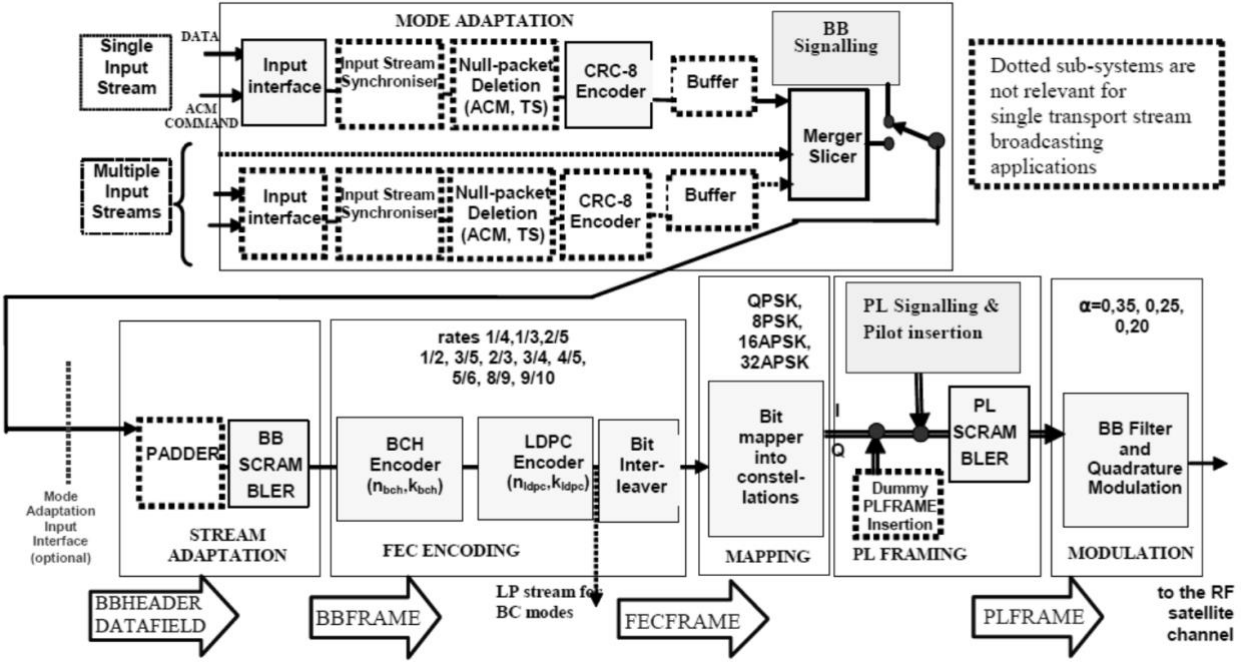

Figure 2-6: Block diagram of a typical DVB-S2 system [3]

The BBFRAME comprises the BBHEADER and the associated data. If there are not enough input data or packets available, the remaining length is filled with zeros in order to achieve a length K_{bch} of the BBFRAME required by the FEC block length. The data of a BBFRAME is scrambled subsequently.

FEC encoding

The error detection and correction subsystem uses BCH as the outer and LDPC as the inner code. The authors of [41] studied the influence of BCH and LDPC code parameters to optimize the performance characteristics. The BCH code efficiency becomes higher with a larger block length. They studied BCH codes with code rates slightly lower than unity and with block lengths from 12000 bits to 20000 bits. It was shown that in order to provide a quasi-error free transmission with a Bit Error Ratio (BER) of 10^{-11} at the BCH decoder output it is necessary to have BER values at the decoder input that do not exceed the following values: 8.81×10^{-7} for BCH(16200,16136), 1.62×10^{-5} for BCH(16200,16008) and 4.475×10^{-5} for BCH(16200,15880). The DVB-S2 standard uses an optimized combination of BCH and LDPC code lengths to achieve error performance near the Shannon limit:

- Very large LDPC code length: 64800 bits normal frame length and 16200 bits short frame length. The performance of 16200 bits is about 0.25 to 0.3 dB lower than with 64800 bits [42]
- Large number of decoding iterations (around 50)
- The presence of a large concatenated BCH outer code with a code rate slightly lower than unity. The block length of the outer code is set equal than the LDPC code length
- The BCH outer code (without any interleaver) is considered by the designers as a “cheap insurance against unwanted error floors at high carrier to noise ratios” [42]

BCH codes enable the generation of code words of a certain length, whereby the number of correctable errors can be determined. In the case of DVB-S2, the BCH coding can correct about 8 - 12 individual errors. LDPC codes use a sparse or low density control parity check matrix to correct the identified errors. The decoding uses iterative methods to find an approximate solution even with limited computing capacity.

The LDPC code carries most of the redundant information for the error correction. The receiver can correct residual errors after the LDPC decoder using the BCH decoder. The block length including all check symbols and the BBHEADER is set to n_{ldpc} = 64800 bits for a normal FECFRAME and n_{ldpc} = 16200 bits for a short FECFRAME (see *Figure 2-7*). The shorter frames allow lower latency in real-time applications with the disadvantage of a less efficient error detection and correction. The selection of a code rate between ¼ and 9/10 allows for the gradual adaption of the error correction measures. The code rates fractions represent the code rate of the LDPC. However, there must be a certain number of information bits K_{bch} for creating a FECFRAME for each LDPC code. Interleaving applies to the continuous bit stream to send the data as an independent, random sequence.

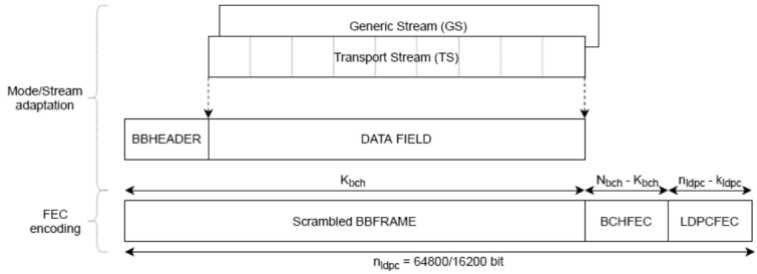

Figure 2-7: FECFRAME with a fixed length (64800 or 16200 bits) [3]

Mapping

In the following step, the bits are mapped to the symbols of a constellation for a selected digital modulation method. QPSK, 8PSK, 16APSK and 32APSK are available. Depending on the number of used symbols M_{MOD}, $\eta_{MOD} = \log_2(M_{MOD})$ bits are assigned to a symbol by serial-to-parallel conversion.

For QPSK and 8PSK, Gray coding is used for the mapping, in which neighbouring symbols differ in one binary digit only. This minimizes the error propagation which consists of the number of bit errors if a wrong decision between two adjacent symbols is made. 16APSK and 32APSK also contain symbols that differ in their amplitude. The symbols are distributed in concentric circles around the centre. The ratio of the radii of these circles was chosen with regard to satellite-specific transmission conditions in order to compensate for the non-linearities of conventional high-frequency amplifiers. After mapping, the sequence of $64800/\eta_{MOD}$ or $16200/\eta_{MOD}$ symbols is referred to as XFECFRAME (complex FECFRAME).

Physical layer framing

The physical layer framing converts the bits into signals that can be transmitted over a physical medium. The symbols of an XFECFRAME are divided into S blocks with constant length of M = 90 symbols. The number of blocks depends on the type of modulation used. To assist synchronization at the receiver, unmodulated pilot symbols can be inserted between the blocks. If there is no data in form of an XFECFRAME, a dummy frame is created that consists of unmodulated carrier symbols.

For each XFECFRAME, a physical layer header (PLHeader) is created. This PLHeader contains a known start of frame (SOF) pattern for synchronization and contains information regarding modulation and coding (MODCOD) and length of the physical layer frame for the receiver. The MODCOD field comprises 5 bits and contains 28 possible combinations (refer to Appendix A for more information). The TYPE field defines the processed

frame's length and the occurrence of pilot blocks. Since the receiver cannot demodulate the data block without this information, these 7 bits are included into a 64-symbol long code word. This ensures that the information can be demodulated and decoded even under unfavourable reception conditions. The SOF sequence and the PLHeader are modulated into π/2-BPSK symbols, where the phase difference between subsequent symbols is always ±90° to ensure a constant envelope. Thus, a better signal quality can be achieved.

The symbols of the data block undergo physical layer scrambling in order to make the spectral properties of the output signal independent of the user data sequence. To this purpose, the data symbols are rotated in the complex plane on the basis of a scrambling sequence R_n.

Baseband filtering

The pulse shaping adjusts the impulse response to the transmission channel of the transmitted symbols. The pulse shaping uses an SRRC filter with a selectable roll-off factor α = 0.2 - 0.35. A change in the roll-off factor allows to adapt the spectral properties of the transmitted signal.

2.4.1.1 DVB-S2 modes

CCM principle

When using constant coding and modulation (CCM), sufficient transmission power, i.e., EIRP must be allocated to ensure the required availability in the event of impairments caused by atmospheric effects such as rain. Therefore, a margin of 3 – 6 dB (clear-sky margin) [42] should be considered. Depending on the location of the ground station and the rain rate, this means that the capacity of the transmission channel is not used optimally. Therefore, the DVB-S2 standard defines two more modes: Variable Coding and Modulation (VCM) and

Adaptive Coding and Modulation (ACM). Using these modes, the MODCOD can be changed on a frame-by-frame basis.

VCM principle

In VCM mode, the prediction of the link quality is used to set the MODCOD. In a non-GEO satellite, the transmission conditions change during a satellite pass over a ground station. The two parameters that mainly influence the link quality are the distance between satellite and ground station, which depends on the elevation, and the atmospheric attenuation. Thus, in VCM mode, the MODCOD is changed based on the prediction of the distance between satellite and ground station to increase the useful bit rate.

ACM principle

While the prediction of the link distance is fully deterministic, atmospheric conditions can be more difficult to predict. The impact of changing orbit conditions (e.g. through orbit drift or orbit manoeuvres), changing the carrier frequency or using ground stations at different geographical locations, and thus climatic zones, can be significant. The use of ACM enables to cope with these changes.

In ACM mode, the MODCOD is adapted dynamically to the current transmission conditions. The receiver measures the received SNR and determines the optimum MODCOD for the current transmission condition. If the received SNR is above or below a defined threshold, an MODCOD change telecommand is generated. Thus, the ACM mode requires a telecommand link to the satellite. The 28 possible MODCODs determine the gradation of the transmission adaption and the possibility to change them on a frame-to-frame basis. In addition, both transmitter and receiver must be able to cope with a variable bit rate. Additional diagnostic means such as measuring the Packet Error Rate (PER) increase the capability of the receiver to evaluate the received signal. The PER is the ratio of incorrectly received data packets compared to the total

number of received packets. The DVB-S2 standard [3] recommends an accuracy of 0.3 dB for the estimated E_b/N_0 threshold for reliable transmission since the gradation of the receive threshold is around 1 - 1.5 dB (refer to Appendix A for the E_b/N_0 values). The given threshold values for error-free transmission and received SNR define the MODCOD selection. The standard further recommends the use of pilot blocks to ensure receiver synchronization, even in case that the decoding process fails.

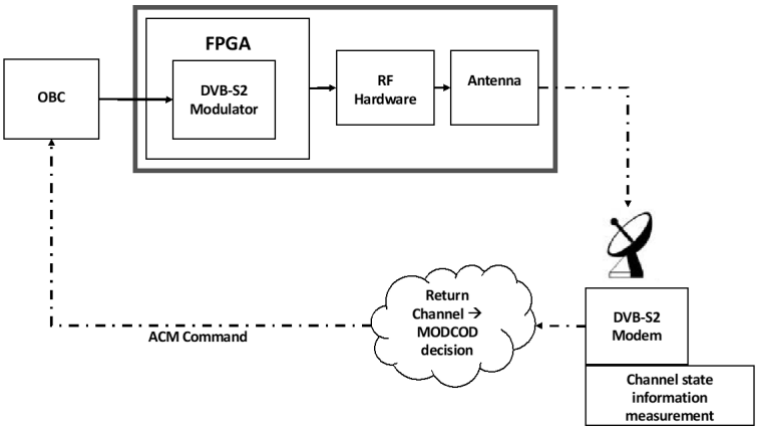

Figure 2-8: Adaptive control loop for DVB-S2 ACM mode schematically

The adaptive control loop, as shown in *Figure 2-8*, determines the efficiency of the ACM mode. The adaptive control loop contains the satellite, a ground station, a channel state information measurement device and a dedicated return channel. At the beginning of a ground station pass, the transmitter (shown in bold outline in *Figure 2-8*) uses the most robust MODCOD. At the ground station, a DVB-S2 compatible modem receives the signal, demodulates and decodes it. In

addition, the channel state information is continuously measured. If the channel state information exceeds a defined value, an ACM command sends the optimized MODCOD combination to the satellite. This ACM command reaches the on-board computer (OBC) of the satellite, which then sends the command to the transmitter. The transmitter adjusts the MODCOD. The loop delay limits the timeliness to adapt to changing transmission conditions. Relevant contributions are the delay for the transmission from/to the satellite and the processing of the incoming data in the ground station. It is estimated that a heavy rain fade in a Ka-band link can change the signal strength by 0.5 dB/s [3]. Consequently, the standard recommends that the maximum recommended delay between evaluation and transmission of the signal quality to the satellite is set to one second.

2.4.1.2 CCSDS over DVB-S2

The Consultative Committee for Space Data Systems (CCSDS) was founded in 1982. CCSDS provides a forum to discuss common issues in the development and the operation of space data systems, which supports interoperability between the different partners. This is the reason why CCSDS protocol standards are used in commercial satellite missions. The DVB-S2 standard established for digital television called the attention of CCSDS. This lead to the CCSDS Recommended Standard 131.3-B-1 [43], that defines how to use the DVB-S2 standard to transmit CCSDS Transfer Frames for telemetry purposes.

The Attached Synchronization Marker (ASM) and the Channel Access Synchronization Unit (CADU) define the interface between both protocols. A Transfer Frame is embedded into each CADU. The CADU corresponds to the input data stream with a corresponding input data rate in the mode adaption block of DVB-S2. The data stream is divided by the

blocks of DATAFIELD length (DFL) bits. Its length depends on the code rate and on the FECFRAME size. The PLFRAMEs are subsequently transmitted through the RF link. *Figure 2-9* shows the format of a CCSDS Transfer Frame using DVB-S2.

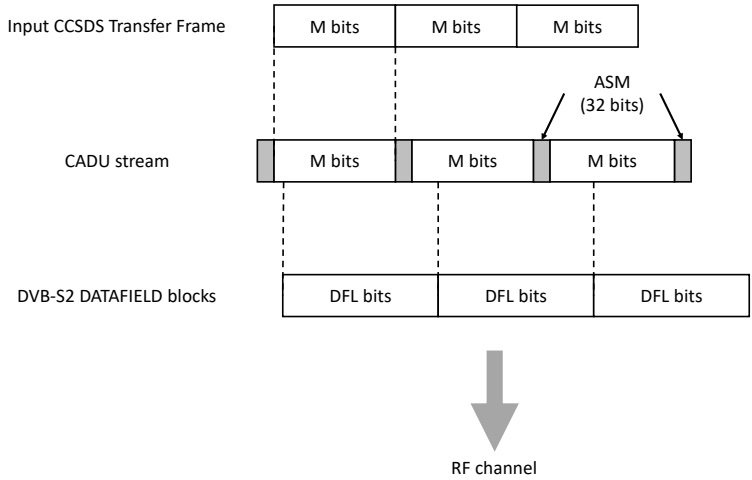

Figure 2-9: Recommended stream format of a CCSDS Transfer Frame using DVB-S2

2.5 Relevant link parameters

Different parameters are relevant to define the performance of the transmission link. The following subsections describe the influence of the most relevant link parameters.

2.5.1 Influence of the orbit type

The movement of satellites around the Earth or another body can be defined by Kepler's laws that describe the relative movement of two point-bodies under the influence of their Newtonian attractions. Kepler's laws are defined as the following [44]:

I. The orbit of a planet is an ellipse with the sun at one focus
II. The vector from the sun to the planet sweeps equal areas in equal times
III. The ratio of the square of the period T of revolution of a planet around the sun to the cube of the semi-major axis a of the ellipse is the same for all planets

An orbit can be defined with 6 Kepler elements at a given time:

- semi-major axis a: the sum of the perigee and apogee distances divided by two. The perigee defines the nearest point and apogee the farthest point an orbiting body (i.e. satellite) to the primary body (i.e. Earth). For circular orbits the altitude is often given instead of the semi-major axis: semi-major axis = altitude + Earth radius (6378 km)
- Eccentricity e: defines the shape of an orbit. If a satellite orbits Earth, then $0 < e < 1$. An eccentricity of 0 defines a circular orbit, the larger e, the more elliptic is the orbit
- Inclination i: defines the angle between the orbit plane and the equator
- Right Ascension of the Ascending Node (RAAN) or Longitude of the Ascending Node Ω: defines the angle between the ascending node of the ellipse (where the orbit passes from south to north through the equatorial plane) with respect to the vernal equinox (apparent position of the Sun on 21st March). An alternative is also often used: The Local Time of the Ascending Node (LTAN), which defines the local mean time at which the spacecraft crosses the equator
- Argument of perigee ω: angle between the ascending node and the perigee

- True anomaly ν: defines the position of the orbiting body along the ellipse at a given time

A geocentric orbit can be further classified according to its altitude, its eccentricity and its inclination as shown in *Table 2-1*. A special orbit is the Sun-Synchronous Orbit (SSO). It is an orbit where the surface of the Earth is illuminated by the Sun from the same angle relative to the satellite. The J2 perturbations, which are the effects caused by Earth´s oblateness, move the RAAN over time at a constant rate depending on the altitude, eccentricity, and inclination. Using the J2 perturbation property, it is possible to choose the orbit such as the RAAN changes at a rate of 360 degrees each year, keeping the orbit at the same orientation with respect to the Sun.

Table 2-1: Geocentric orbit types according to altitude, eccentricity and inclination

Parameter	**Orbit type**
Altitude	LEO: below 2000 km MEO: above LEO and below GEO GEO: 35786 km
Eccentricity	Circular: 0 Elliptical: between 0 and 1
Inclination	Equatorial: ca. 0° Inclined: others than 0° SSO: 97° Polar: 90°

The orbit type mainly influences the free space loss, and the atmospheric losses. The free space loss defines the attenuation between two isotropic antennas in free space with a specific wavelength λ, expressed as a power ratio as shown in the following equation:

$$\text{free space loss} = 10log_{10}\left(\frac{4\pi L_S}{\lambda}\right)^2 \ [dB] \qquad \text{Eq. 2-13}$$

The free space loss increases with the square of distance between the antennas (L_S). Thus, the free space loss depends on the link geometry. Note that the free space loss is rarely used standalone, but is a factor of the Friis transmission to ensure that sufficient power is reached at the receiver as formula shown in Eq. 2-14. P_R is the power at the receiver, P_T the output power of the transmitter, G_T the transmitting antenna gain, L_a the atmospheric loss, L_{FS} the free space loss and G_R the receiving antenna gain.

$$P_R = P_T G_T \frac{1}{L_a} \frac{1}{L_{FS}} G_R \qquad \text{Eq. 2-14}$$

The ground station's position, and the satellite's location define the link geometry as shown in Figure *2-10*. Note that the altitude of the ground station above sea level has an impact on the link geometry. For a given ground station location and a defined position of the satellite, the free space loss is fixed. The slant range through the atmosphere depends on the elevation under which the ground station sees the satellite. The following subsection describes the atmospheric loss in more detail.

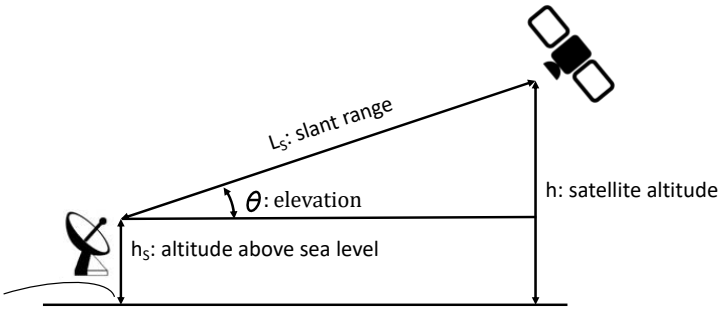

Figure 2-10: Link geometry definition

2.5.2 Influence of the atmosphere

Atmospheric loss depends on the used frequency band. In general, the loss increases with increasing frequency band. *Table 2-2* shows the frequency band convention according to the Institute of Electrical and Electronics Engineers (IEEE). It should be however noted that in the satellite communication community, band designations are used in a flexible manner. Thus, it should be always clear which reference is being used.

The RF spectrum is more and more crowded due to the ever-increasing use of satellites. This can lead to interference problems with the transmission and reception of satellite signals. The ITU coordinates the use of the RF spectrum. Furthermore, ITU publishes the ITU-R Recommendations, that are a set of technical standards that cover technical, operational or procedural recommendations [45].

ITU has published different recommendations for using prediction models for the loss due to clouds and fog [46], atmospheric gases [47] and rainfall [48]. It is important to characterize the loss figures related to atmospheric effects since they have a significant impact on the link quality. [46] predicts the attenuation depending on the used frequency, the propagation distance, the atmospheric temperature and the cloud liquid water density. *Figure 2-11* shows the atmospheric gas attenuation spectrum comparing dry air and a water vapor density of 7.5 g/m^3. The general trend is that the loss increases with increasing frequency. The attenuation peaks at around 22 GHz and 60 GHz are due to excitation of molecular rotation of various components in the atmosphere: mainly water vapor and molecular oxygen, respectively. This influences the decision of suitable carrier frequencies for satellite communication applications. Here, a 500 km propagation distance and 293.15 K atmospheric temperature is assumed. The attenuation increases with higher cloud liquid water density and thus thicker fog. The amount of water vapor

contained in the air is evaluated with the ITU-R P.676-10 recommendation.

Table 2-2: Frequency bands according to the IEEE Standard 521–1984

Band designation	**Frequency range**
VHF	0.03 to 0.3 GHz
UHF	0.3 to 3 GHz
L	1 to 2 GHz
S	2 to 4 GHz
C	4 to 8 GHz
X	8 to 12 GHz
Ku	12 to 18 GHz
K	18 to 27 GHz
Ka	27 to 40 GHz

The rain loss prediction is described in [48]. The rain loss depends on regional and seasonal changes. The rain drops deviate the signal which lowers its SNR at the receiver. Furthermore, the rain causes degradation of the polarization purity. The rain rate, expressed in mm/h, depends on the propagation path length and has an impact on the rain loss. Thus, a higher used frequency, as well as a higher path length, leads to a higher rain loss. The link availability, expressed as a percentage, allows to calculate the rain loss. Here, the evaluation of the strongest rain rate expected in a specific region allows calculating the expected rain loss for a specific ground station. This largest expected rain loss accounts in the link budget calculation. *Figure 2-12* shows the rain attenuation for different rain rates, link distances and frequencies. Above

10 GHz, the attenuation increases exponentially with frequency. *Figure 2-13* shows the rain attenuation depending on the elevation angle at 10 GHz and 30 GHz for different altitudes, respectively.

Figure 2-11 to *Figure 2-13* show that the atmospheric losses can get very high and depend on various factors. Generally, there is a difference depending if the ground station is located in a dry or a wet region. Furthermore, the atmospheric loss depends on the frequency used and the elevation angle. Thus, each case has to be evaluated separately. By designing the transmitter system according to the worst cases, the link margin thus has to be very high. ACM methods can exploit this link margin.

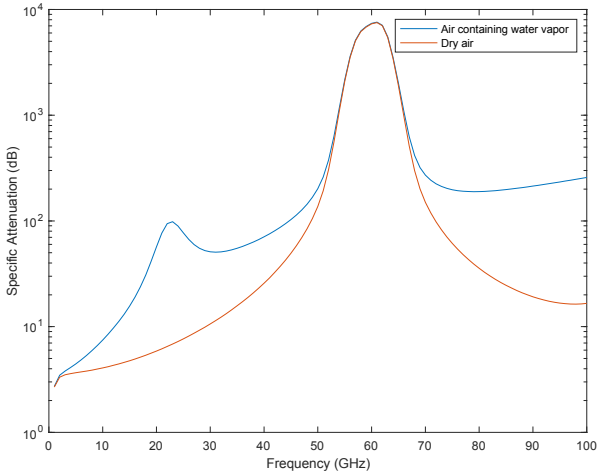

Figure 2-11: Atmospheric gas attenuation spectrum for dry and wet air according to the [47] recommendation. Simulated with MATLAB, according to the data sets provided by [46] and [47]. The attenuation due to water vapor and the climatic parameters depend on the location of the ground station

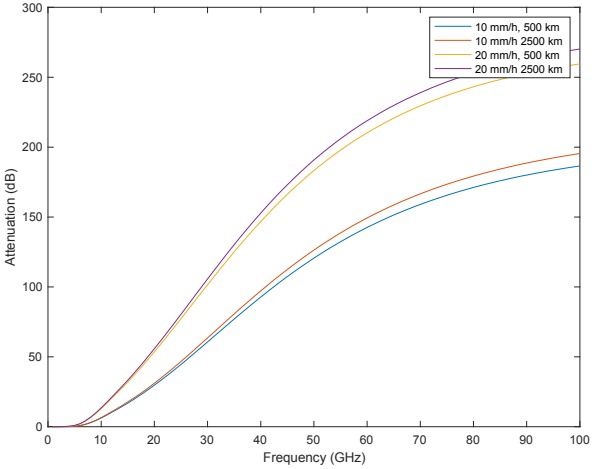

Figure 2-12: Signal attenuation due to rainfall as a function of frequency according to ITU-R P.838-3; parameters are the rain rate and the link distance

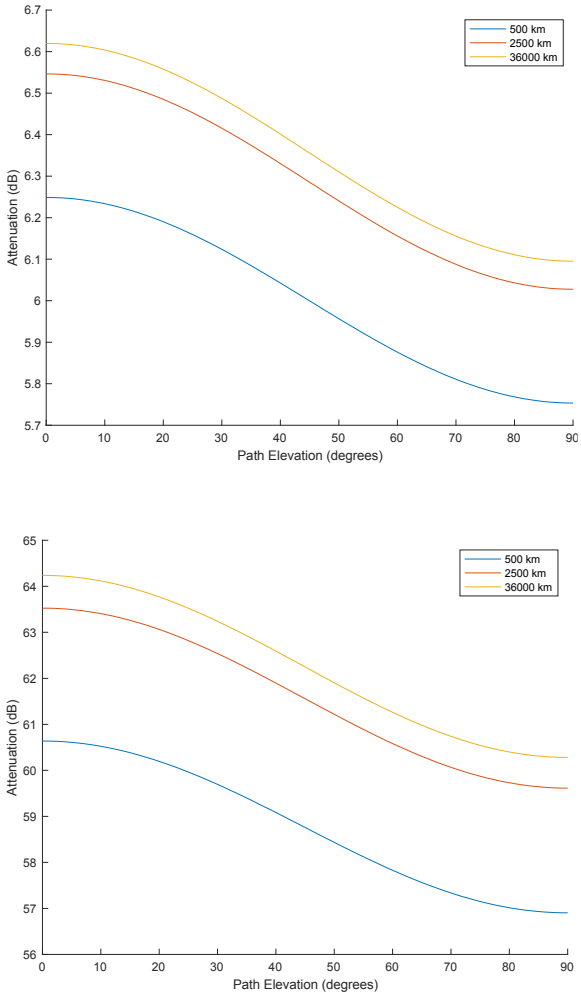

Figure 2-13: Attenuation due to rainfall as a function of the elevation angle for X-band with 10 GHz (upper panel) and Ka-Band with 30 GHz (lower panel) for different path lengths. The rain rate was set to 10 mm/h. Simulated with MATLAB, according to the data sets provided by [48]. The elevation angle of the 36000 km altitude case corresponds to a GEO satellite where the elevation angle depends on the position of the satellite and the ground station location

2.5.3 Impact of noise

Noise is an unwanted power contribution, random or deterministic, in the bandwidth of the wanted signal. Due to the randomness of noise, basic noise models are typically used to characterize a communication channel. One of these models is the Additive White Gaussian Noise (AWGN) model. Other unwanted contributions, like for example carriers from other transmitters, are summarized as interference.

The noise reduces the receiver's ability to recreate the information of the transmitter's signal. The noise's origin is from the transmitter and receiver components, and the noise originated by natural resources of radiation, like the Earth, the Sun or the space, within the transmitter's and receiver's antenna. The main noise contribution in a communication channel is from the components of the receiver, mainly the first amplifier stage. For further information on noise origin and noise characterization it is referred to [39].

Phase noise and thermal noise can be present in the communication channel, mainly introduced by the amplifier stage(s) of the receiver, LOs and clock instabilities of transmitter and receiver. Thermal noise is especially relevant for the amplifier components in the communication channel. Thermal noise depends on the noise temperature, Boltzmann constant and frequency bandwidth:

$$N = kTB \qquad \text{Eq. 2-15}$$

where k is the Boltzmann constant (k = 1.379 x 10^{-23} J/K = -228.6 dBW/Hz K), T the noise temperature in Kelvin and B the frequency bandwidth in Hertz. Thus, cooling or temperature control can help reducing the thermal noise in the components if necessary. Phase noise represents random fluctuations in the phase of the (modulated) carrier. These fluctuations consist in time deviations from the perfect periodicity (jitter) of the oscillator or the digital clock of the system. Phase noise can lead

to random rotations and amplitude variations in the received signal. *Figure 2-14* shows how phase noise and thermal noise influence the constellation diagram of a QPSK-modulated signal.

An antenna gathers noise within its radiation pattern. This noise is a function of the antenna's pointing direction, its radiation pattern and the surrounding environment. The noise captured by a satellite's antenna comes mainly from Earth and outer space. For a ground station, it stems mainly from the sky and from the Earth. The antenna noise temperature depends on the frequency and the satellite orbit. The satellite antenna noise temperature depends on frequency and the covered area. The oceans produce less noise than the continents. A typical value for ground station antenna noise temperature in uplinks is 290 K.

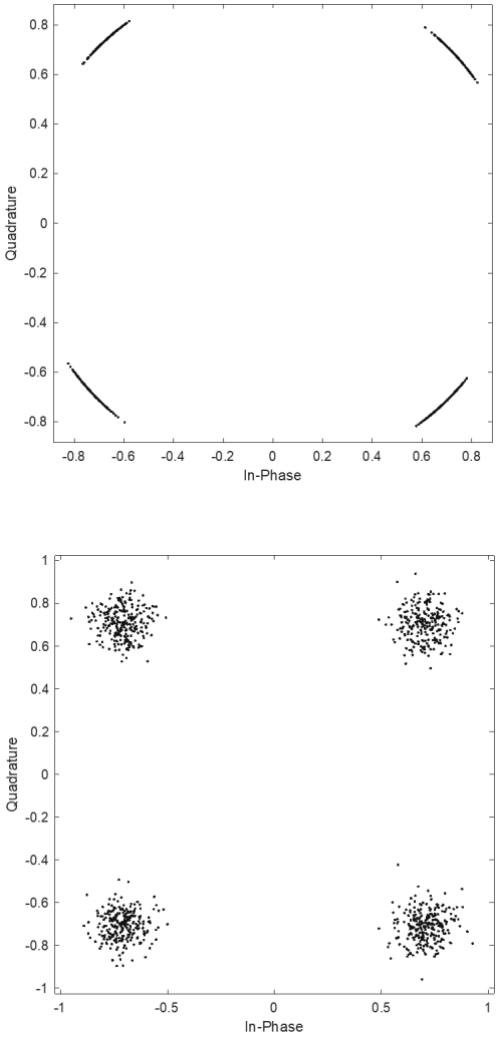

Figure 2-14: Influence of phase noise (upper panel) on a QPSK-modulated with a phase noise vector at -50 dBc/Hz and a frequency offset of 20 Hz. Thermal noise (lower panel) on a QPSK-modulated signal with an SNR of 20 dB. Simulated with MATLAB

2.6 Radiation environment

A satellite experiences different types of radiation. Depending on the satellite's orbit, the amount of received radiation varies substantially since residual atmospheric effects and the position relative to the Earth's radiation belts, the inner and outer Van Allen belt, are at play. Furthermore, geomagnetic field irregularities such as the South Atlantic Anomaly (SAA) further increase the particle flux the satellite is exposed in orbit.

Radiation is typically categorized according to its origin rather than by its physical properties:

- Trapped particles. These are mostly protons and electrons that are captured by Earth's magnetic field. The inner Van Allen belt primarily traps electrically charged ions and protons whereas the outer Van Allen belt mostly contains electrons. The inner belt ranges from 700 km to 6000 km and the outer belt from 16000 to 58000 km altitude above Earth's surface. The inner belt contains high concentrations of protons with kinetic energies even over 100 MeV and the outer belt mainly electrons with kinetic energies up to 7 MeV. The Van Allen belts have a torus-shape
- Solar energetic particles (SEP). These include protons, electrons and ions that are expelled during solar flares or coronal mass ejection (CME) events. These produce mainly protons with kinetic energies above 10 MeV
- Galactic cosmic rays (GCR). These consist of highly energetic protons and ions that originate outside the solar system. Specially the GCR particles that travel with velocities near the speed of light affect the electronics of spacecraft

2.6.1 Radiation effects

Radiation can have different effects on satellite components. These can mainly be divided into the TID, displacement damage (DD) and SEE.

The TID is the cumulative dose of a semiconductor due to ionizing radiation over the exposition time. As ionizing radiation passes through a material it is depositing energy along its trace while being decelerated. The dose of energy is defined as unit of energy per unit of mass. The TID unit of measurement is rad, which is equivalent to 10^{-2} J/kg. The amount of energy deposited by an individual radiation event is defined by the interaction between the particle and the radiated material. The amount of energy deposited per mass unit of material is called Linear Energy Transfer (LET), which is measured in MeV·cm^2/mg. A high LET leads to quicker particle deceleration, thus inhibiting the particle to reach great penetration depths. Yet, a high LET also increases the probability of damage of the material within the affected region, since more energy is transferred into a smaller volume.

Collision with high energetic mass-rich particles, such as protons or neutrons, causes DD. It causes irregularities in the crystalline atomic structure of the exposed material.

In contrast to cumulative radiation effects such as TID or DD, SEE can take place during individual radiation events or within a short amount of exposure time. Their severity on electronic components ranges from temporal and reversible to permanent and destructive. The most important types of SEE are the following:

- Single Event Upset (SEU): change of the state of a singular stored bit in a memory, essentially flipping its value. This error persists until the memory is rewritten
- Multi Bit Upset (MBU): describes multiple upsets

- Single Event Transient (SET): a transient current is injected into a signal path potentially disturbing its nominal operation.
- Single Event Functional Interrupt (SEFI): causes a device to reset, lock-up or become faulty in a reversible way, that does not require a power cycle to recover
- Single Event Latchup (SEL): an induced high-current state within the electronic device that can lead to faulty operation or even destruction. Its effect can be mitigated by disabling the power to the device within a short amount of time after the occurred SEL
- Single Event Burnout (SEB): irreversible destruction of a device by induction of a high-current state in a power transistor
- Single Event Gate Rupture (SEGR): ion-induced condition in a Metal Oxide Semiconductor Field-Effect Transistors (MOSFET) transistor that leads to a conductive path within the gate's oxide layer

3 Analysis of an adaptive transmitter for space applications

To design an adaptive transmitter for small satellite applications, requirements and constraints have to be defined. In the following, a use case is defined to provide a specific scenario to derive design constraints, e.g. mass, volume, RF power, available RF bandwidth and minimum data rate. The potential of using adaptive transmission on an SSO-to-MEO-satellite transmitter is analysed in this chapter. The compensation for different effects and their impact on the link budget as well as the link dimensioning and the performance improvement when using ACM is described.

3.1 Use case – the ROMEO mission

The use case consists of a satellite mission which is designed to explore the region of the inner Van Allen radiation belt. The satellite's mass is approximately 60 kg. The ROMEO (Research and Observation in the Medium Earth Orbit) satellite shall be launched to an orbit of 600 km altitude and shall then perform orbit change maneuvers to reach an elliptical orbit of 314 km perigee and 3025 km apogee. The mission shall prove function and performance of novel electronic components. One of these components is the adaptive transmitter system discussed in this thesis. *Figure 3-2* shows the CAD design of the ROMEO satellite with the subsystems and their components. For a more detailed overview of the ROMEO mission, refer to [49].

The ROMEO mission is planned for a minimum lifetime of one year. The launch is into a sun-synchronous orbit. This offers the most flight opportunities since the satellite can be launched as a piggy-back. In the first mission phase, different Earth observations with an Earthshine telescope and with a camera

system are carried out. Then, maneuvers are carried out in order to transfer the satellite to MEO orbit. This transfer takes about 5 months and is intended to prove function and performance of a novel water-based propulsion system. Furthermore, the transfer maneuvers ensure the possibility to de-orbit the satellite and intend to avoid collisions with other satellites in orbit. The lowering of the perigee guarantees re-entry within 25 years regardless of the satellite's condition. Thus, it fulfils the European Code of Conduct for Space Debris Mitigation. The radiation environment was analyzed in [50]. This analysis showed that the particle flux is highest at low latitudes. Thus, ω was assumed constant at 0°, meaning the apogee is in the low latitude regions, i.e. in the equatorial region. The main sources of radiation were trapped particles in the Van Allen radiation belts, GCRs and solar particle events (SPE). The average flux of both electrons and protons raised at higher altitudes. Between 0.1 and 5 MeV, the number of electrons exceed the number of protons while between 5 and 400 MeV the protons dominate the radiation flux. The TID was analyzed for a mission duration of one year. The dose depth curve, as shown in *Figure 3-1*, shows that an aluminum shielding of 2mm decreases the TID to 39.8 krad, 5 mm to 9.5 krad, 8 mm to 6.2 krad and 10 mm to 5.4 krad. This indicates that a shielding of 10 mm is necessary for the adaptive transmitter since mainly COTS components are used. The trapped protons are the major contributor to the TID and are barely mitigated by the aluminum shielding. Furthermore, the expected SEU rates were calculated for the SoC on the ROMEO mission for a worst day scenario. For this calculation, the cross section of the Block Random Access Memory (BRAM) of the AMD Xilinx Zynq-7000 SoC was used. With the cross section the maximum LET of the stopping ion over its entire path length in the sensitive volume was calculated. The sensitive volume is based on a default silicon device of 28 nm. Combining the cross section, the sensitive volume and the LET spectra, the SEU rates could be calculated. The SEU rates depend on the orbit position

and reach up to 50 SEUs per day. This is an expected value since typically the SEUs per day for a LEO satellite range from a few to a few hundred upsets per day, depending on the satellite's specific orbit and the prevailing space radiation conditions. This SEU rate has to be considered when designing the adaptive transmitter.

The dynamic adaption of the transmitter parameters to the orbit conditions is studied. Different radiation instruments will characterize the lower radiation belt. They will also collect data for space weather studies. Furthermore, all components of the satellite bus are monitored for their radiation dose. The ROMEO avionics core combines digital data and signal processing in one highly integrated SoC. The use of COTS components where possible is a novelty for an MEO satellite mission. This would show the use of cost-effective new space design principles in this challenging environment and the COTS performance in it.

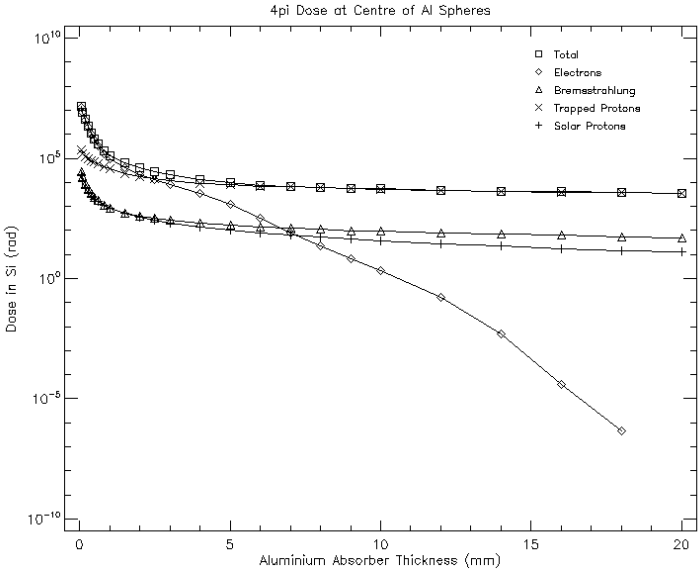

Figure 3-1: SPENVIS simulation of the dose depth curve of the ROMEO mission [50]

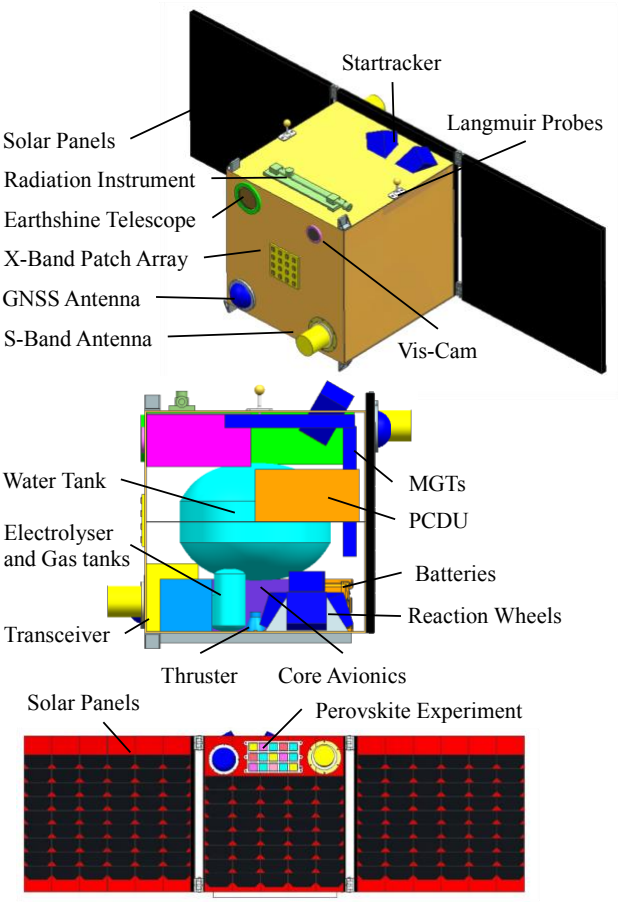

Figure 3-2: CAD of ROMEO satellite. Each subsystem is shown in a designated color: light blue indicates the orbit control subsystem, dark blue indicates the attitude control system, orange indicates the power subsystem, green and pink indicates the payload subsystem, yellow indicates the communication subsystem, purple indicates the on-board data handling subsystem. MGT represent the magnet torquers, PCDU the power control and distribution unit, and GNSS the global navigation satellite system [49]

Table 3-1: Characteristics of the ROMEO Satellite

Parameter / Subsystem	**Characteristics**
Orbit	Start orbit: 600 km circular sun-synchronous Final orbit: 314 km x 3025 km elliptical De-Orbit: within 25 years, according to the European Code of Conduct for Space Debris
Orbital Control	1-N-water-based engine with 10 kg fuel (water). The system is based on electrolysis
Communication	Adaptive payload data transmission in the ham radio X-band (10.45 – 10.5 GHz) featuring the CCSDS-Standard Telemetry and telecommand in the commercial space research S-band (2025 – 2100 MHz telecommand and 2200 – 2290 MHz telemetry) Use of the Institute of Space Sytems (IRS) ground stations and ground station network
Attitude Control	3-axis stabilization using reaction wheels with an alignment accuracy of 0.5°
Power	3 solar panels with 90 W power Scalable Li-Ion-battery system
Mass	60 kg incl. 10 kg fuel

Table *3-1* summarizes the features of the ROMEO satellite.

Due to the elliptical orbit, which constantly changes due to the orbit change maneuvers, the need for an adaptive data downlink transmitter platform arises, that is capable of adapting its transmission configuration to the current transmission conditions. Thus, for this mission it is intended to demonstrate ACM with the transmitter system. Furthermore, the transmitter shall be compliant with the IRS ground station network. This implies compatibility with the CCSDS recommendations for the physical and the data link layer. These recommendations will be implemented in a COTS SoC featuring a dual-core processor and an FPGA. Furthermore, the used ham radio X-band allows a more rapid frequency registration and coordination. Furthermore, the filing process is free of charge compared to several thousand euros that typically cost a frequency registration and notification. The maximum usable bandwidth in this frequency band is 50 MHz. Thus, bandwidth-efficiency is a driver for the transmission system.

3.2 ROMEO orbit analysis and operational concept for the adaptive transmitter system

The detailed orbit analysis presented hereafter is a prerequisite to define requirements for the adaptive transmitter of the ROMEO satellite. The analysis on the slant range and contact time per day and over the mission time are important since the orbit of the satellite changes over the mission time. The analysis was performed for two different ground stations that pertain to the IRS ground station network as shown in *Table 3-2*. The ground station's geographical positions contribute to different effects in the transmission quality. From [51] it can be seen that the rainfall rate exceeded 0.01% of an average year is ca. 40 mm/h for STR ground station

and 110 mm/h for MAL ground station. This 0.01% outage due to rain is the reference rain rate of the corresponding ITU model.

Table 3-2: IRS ground station parameters for the ham radio X-band downlink

Parameter	**Ground station**	
	Stuttgart, Germany (STR)*	Banting, Malaysia (MAL)
Latitude	48.745° N	2.84° E
Longitude	9.106° N	101.51° E
Altitude above sea level	445 m	0 m
Antenna Diameter	4.5 m	
Ground Station Antenna Gain	52.32 dBi @10.475 GHz	
Gain to noise temperature (G/T), clear sky	28.5 dB/K	
Frequency range	10.4 – 10.5 GHz	
Half Power Beamwidth (HPBW)	0.21°	
Polarization	Left handed and right handed circular	

*anchor ground station

The impact of the satellite's orbit is analysed with the "Analysis, Simulation and Trajectory Optimization Software for Space Applications" (ASTOS) simulation tool. The mission

phases of the ROMEO satellite mission are divided into the following phases:

- *Phase 1 – SSO*. During 3 months the satellite operates in an SSO at 600 km altitude. The mission start time in the simulation is 2024-01-01T00:00:00. In this mission phase, the focus is on Earth observation and on first tests with the adaptive transmitter
- *Phase 2 – Transfer*. In this phase the technology demonstration of the water engine begins. The apogee is raised while the perigee is lowered by subsequent engine burns. The concept for the engine burns is such that, even if the water engine fails at any time, the re-entry is within 25 years. This mission phase lasts, according to the simulations made in [52], 125 days. Furthermore, the radiation dose is measured with the radiation sensor suite. Also, the Earth observations with the Earthshine telescope and the camera system continue. It is also tested how the change in the orbit conditions impact the adaptive transmitter
- *Phase 3 – MEO*. This is the end phase of the ROMEO mission. The satellite is intended to stay in this elliptical orbit where the apogee is 314 km and the perigee 3025 km height above the Earth's surface for at least 6 months. The space weather measurement continues as well as the Earth observations. The adaptiveness of the transmitter is further extended to its full potential

The assumptions and constraints for the simulations are listed in *Table 3-3*.

Table 3-3: Simulation assumptions and constraints of the ROMEO mission

Parameter	**Assumption / Constraint**
First orbit	600 km height sun-synchronous orbit LTAN: 11:00
End Orbit	Perigee: 314 km Apogee: 3025 km True anomaly drift: 0.7°/day Argument of perigee drift: 2.3°/day
Elevation angle	Worst case: 5° Best case: 90°
Center frequency	10.475 GHz
Bandwidth	50 MHz (max. allowed by ITU), roll-off = 0.2
Symbol rate	41.55 Msps
Availability	99.9%
ITU recommendations used	Attenuation due to clouds and fog [46] Attenuation by atmospheric gases [47] Attenuation due to rainfall [48] Climatic models [51]

The orbit raising strategy from [52] is shown in *Figure 3-3*. The plot shows the change of the perigee and the apogee according to the ROMEO mission phases. The steady increase of the apogee and the lowering of the perigee during the transfer in Phase 2 can be clearly seen. *Figure 3-4* shows the orbit in Phase 1 and Phase 3 and the drift in the argument of perigee in Phase 3.

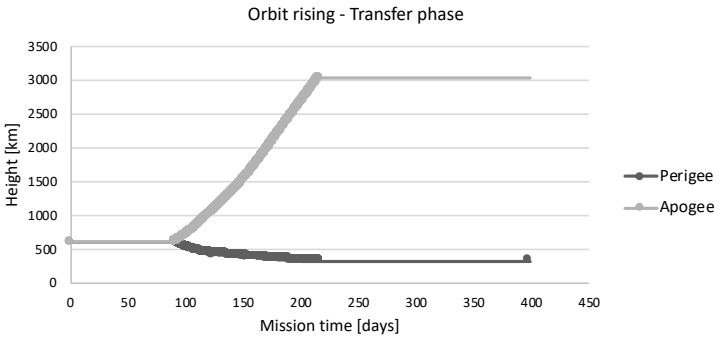

Figure 3-3: Change of the apogee and the perigee during the ROMEO mission

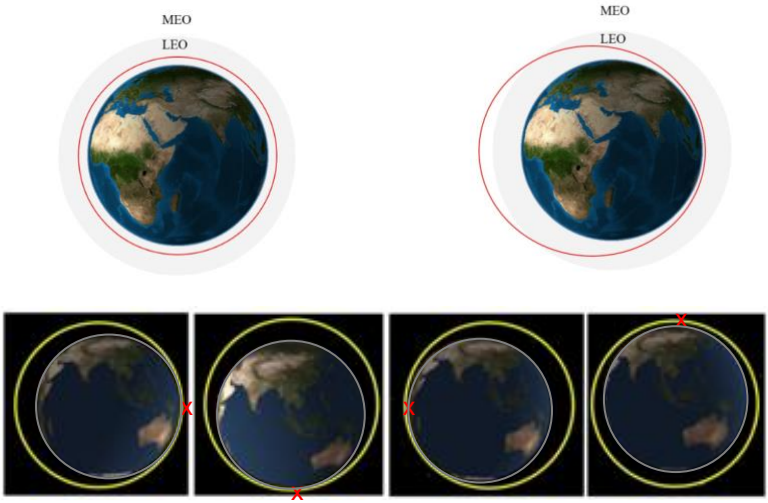

Figure 3-4: Phase 1 - SSO (upper left panel). Phase 3 - MEO (upper right panel). Argument of perigee drift during the Phase 3 (lower panel): Day 1 $\omega = 0°$, day 40 $\omega = -90°$, day 80 $\omega = 180°$, day 120 $\omega = +90°$ [49]

The orbit rising strategy from [52] was imported into ASTOS using a script to be able to analyse the influence on the adaptive transmitter and to simulate the ground station visibilities and contact times.

In a first analysis, the increase of the slant range over mission time was simulated for the best and the worst cases, respectively. In Phase 1, the minimum slant range is 600 km and the maximum 2329 km. In Phase 3 the minimum slant range is 314 km and the maximum 6375.7 km. Consequently, the free space loss varies during the mission time as given in *Table 3-4*. The highest variation in free space loss during the mission time is 26.1 dB, which directly impacts the link budget. Furthermore, the higher rain loss in Malaysia according to [51] implies further loss that is important to consider. Note that the free space loss is frequency dependent and the comparison made is only valid because a constant center frequency of 10.475 GHz (according to *Table 3-3*) was considered.

Table 3-4: Slant ranges and free space loss for the different ROMEO mission phases

Mission phase	**Slant range [km]**	**Free Space Loss [dB]**
Phase 1 (600 km SSO)	Min: 600	168.4
	Max: 2329	180.2
Phase 3 (314 x 3025 km MEO)	Min: 314	162.8
	Max: 6375.7	188.9

An analysis of the ground station visibility was performed for the ROMEO mission. The different geographical positions and climatic conditions of the IRS ground stations as listed in *Table 3-2*, result in different ground station visibilities. The ground station visibility determines the time a ground station has a line of sight to the satellite and is capable of having sufficient link margin. The different ground station visibility has an impact on the ROMEO missions' operational concept. *Figure 3-5* shows the average contact time per day, and *Figure 3-6* the mean and maximum ground station pass time over the mission time, respectively. The ground station pass times for MAL and STR are similar. Yet, there are more STR ground station passes which result in a higher contact time per day.

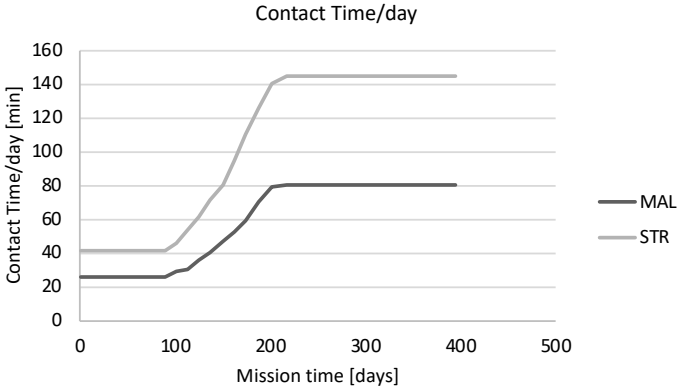

Figure 3-5: Contact time per day for ground stations located in Stuttgart (STR) and Banting (MAL) over the mission time. A minimum elevation angle of 5° was considered

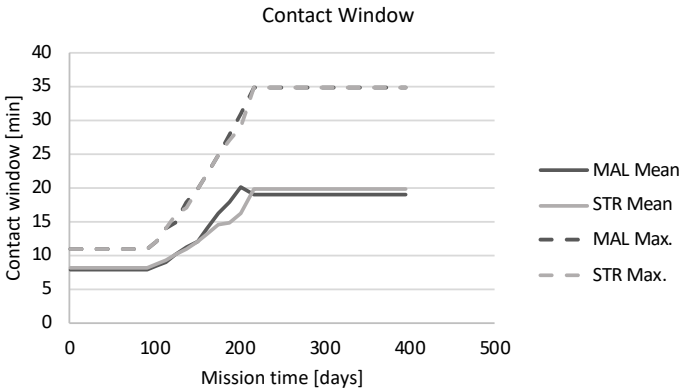

Figure 3-6: Mean and maximum contact window for ground stations located in Stuttgart (STR) and Banting (MAL) over the mission time. A minimum elevation angle of 5 °was considered

3.3 ROMEO link budget analysis

In order to design a ham radio X-band data transmitter suitable for the ROMEO mission, a link budget analysis was performed to determine the expected performance as well as the minimum required EIRP to fulfil the different requirements. This section explains the tool which was used for the calculations of the atmospheric losses. Furthermore, the atmospheric attenuations in the signal path are described. Then the downlink budget is presented and further discussed regarding its data throughput.

3.3.1 Atmospheric attenuations on the signal path

The ITU-R PROPA tool has been developed by CNES to enable calculating the atmospheric attenuations in the signal path [53]. PROPA was integrated into the own link budget tool. The following atmospheric effects are considered: Gas Attenuation (A_{Gas}), Rain Attenuation (A_{Rain}), Clouds Attenuation (A_{Cloud}) and Scintillation Impairment (I_{Scint}). A_{cloud} includes the loss due to fog

according to [46]. Scintillation is an effect caused by ionospheric irregularities that act like lenses which focus and defocus the radio waves. Scintillation affects both the amplitude and the phase of the signal. The input and output parameters of PROPA of each attenuation are listed in Appendix C. The following equation is used to calculate the total atmospheric attenuation:

$$A_{total} = A_{Gas} + \sqrt{(A_{Cloud} + A_{Rain})^2 + {I_{Scint}}^2} \qquad \text{Eq. 3-1}$$

A_{total} is calculated for the ground stations listed in *Table 3-2* assuming the parameters of *Table 3-3*. For the following simulations, a rain rate of 40 mm/h for STR and of 110 mm/h for MAL ground station is considered, according to [51]. *Figure 3-7* shows the total atmospheric loss for an average annual time percentage of excess for the rain attenuation for STR and MAL. This parameter calculates the rain attenuation, which satisfies the exceedance condition, in terms of the percentage of an average year. *Figure 3-8* shows the attenuation change as a function of the elevation angle.

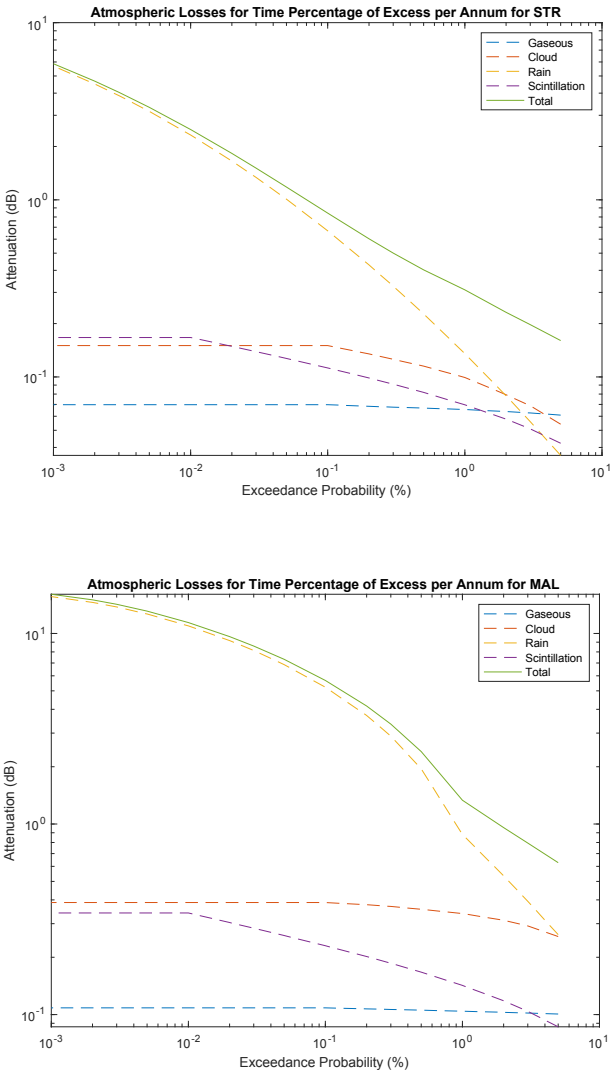

Figure 3-7: Atmospheric losses depending on the time percentage of excess for an average year for the STR (upper panel) and the MAL (lower panel) ground stations. The considered rain rate is according to [51]

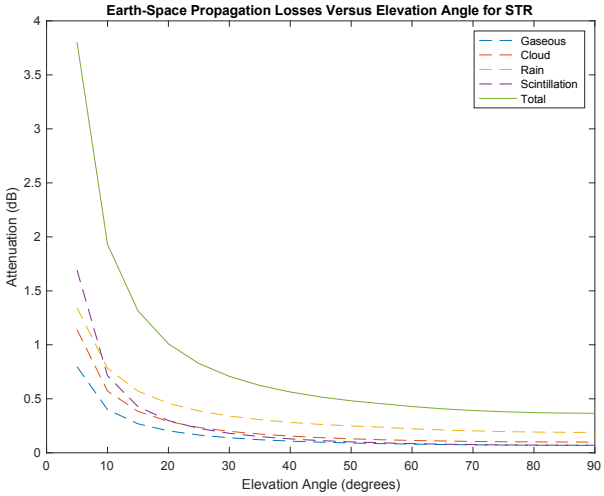

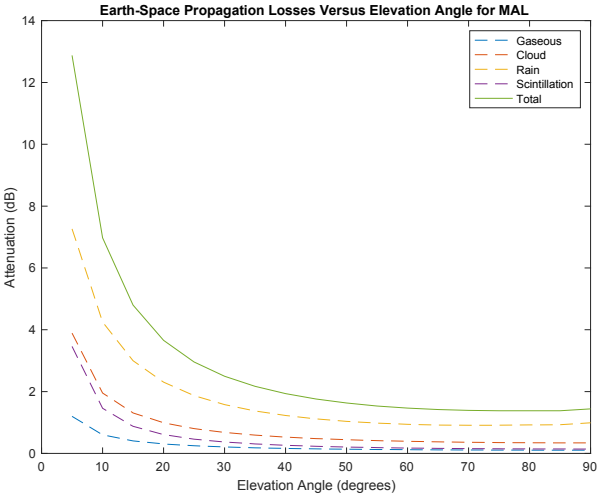

Figure 3-8: Atmospheric losses depending on the elevation angle during a satellite pass over the STR (upper panel) and the MAL (lower panel) ground station. The considered rain rate is according to [51]

3.3.2 Determination of the minimum required EIRP

The minimum required EIRP is calculated from the requirements on data rate, minimum E_b/N_0 and spectral efficiency of the given MODCOD listed in Appendix A. Also, the maximum permissible bandwidth allowed is considered. The impact due to atmospheric influences in 3.3.1 is also considered. *Table 3-3* lists the assumptions and constraints for the downlink link budget.

Link budgets have been analyzed for the usage of the STR ground station as described in *Table 3-2*. For this analysis, a constant maximum possible symbol rate was chosen, and the MODCOD was adapted. Hence, the link budget is calculated for the highest MODCOD that is capable to close the link with a minimum margin of 3dB. In Appendix D, a detailed link budget for the STR and also for the MAL ground station can be found.

Table 3-5 lists the link budget for the different mission phases. It can be seen that for all cases, the bandwidth used by the modulated carrier was always below the permitted 50 MHz as required in *Table 3-3*. For the first mission phase, link budgets were calculated for best and worst cases, respectively. It can be seen that during this mission phase the highest MODCOD 28, i.e. 32APSK code rate 9/10, can be used with a data rate of 185 Mbps for the best case. Even for the worst case it is possible to use 8PSK modulation to close the link with a 3.43 dB margin.

The comparison between the 314 km best case with the 3025 km worst case shows that it could be an advantage to change the transmitter waveform according to the current transmission conditions. For the 3025 km worst case, the minimum MODCOD configuration that can be used to close the link is MODCOD 1 (QPSK 1/4). This allows a data rate of 20.36 Mbps. Yet, in the 314 km best case it is possible to use the

highest MODCOD configuration. This allows a maximum data rate of 185 Mbps, which still fulfils the bandwidth constraint.

Table 3-5: Link budget of the STR ground station for the ROMEO mission. The different cases are related to the orbit altitude

Parameter	314 km best	314 km worst	3025 km best	3025 km worst	600 km best	600 km worst
EIRP [dBW]	16.4					
Height [km]	314		3025		600	
Elevation [°]	90	5	90	5	90	5
Rx Gain [dBi]	52.32					
Modulation	32 APSK	16 APSK	QPSK	QPSK	32 APSK	8PSK
Nominal code rate	9/10	3/4	4/5	1/4	9/10	2/3
MODCOD	28	19	8	1	28	13
Spectral efficiency [bits/symbol]	4.45	2.97	1.59	0.49	4.45	1.98
Bit rate [Mbps]	185	109.57	65.94	20.36	185	82.31
Bandwidth [MHz]	49.85	49.86	49.86	49.86	49.85	49.86
Eb/N0 [dB]	21.96	10.12	7.93	5.44	16.34	8.08
Eb/N0 req. [dB]	9.56	5.49	2.67	0.75	9.56	3.65
Margin	11.4	3.4	3.94	3.7	5.78	3.43

Table 3-5 shows that the minimum required EIRP to close the link budget is 16.4 dBW. The RF level budget for the transmitter is shown in *Table 3-6*. An output backoff (OBO) of 2 dB and transmission line loss of 0.6 dB are included, corresponding to an EIRP of 18.4 dBW in saturation. Considering the limited power resources on ROMEO, the RF output power should be as low as possible. PA convert DC to RF power where an amount of power is dissipated into heat; the efficiency is defined as the ratio of the output power to the input power. The thermal control subsystem and the power budget should account for the PA operation. As discussed further in 4.5.4, the efficiency of the PA is up to ca. 45% in the best case. Thus, the output power of the transmitter is defined to 2 W (3 dBW) in saturation and thus, the transmit antenna gain 16 dBi in order to achieve the minimum required EIRP. These values are considering typical power amplifier modules and typical volume resources for the antenna on ROMEO, as described in further detail in 4.5.5.

Table 3-6: RF level budget

Stage	**Gain [dB]**	**Output Power level [dBW]**
DAC	-	-40
Upconverter	10	-30
Power amplifier (saturation)	33	3
Output backoff	-2	1
Transmission line loss	-0.6	0.4
Antenna	16	16.4
EIRP (saturation)		18.4
EIRP (backoff)		16.4

3.4 Link budget and ACM assessment

The various parameters that have an impact on the link budget have to be analysed to understand the role of the relevant link parameters from 2.5 to use adaptive transmission. The adaptive transmission analysis includes the following steps to assess the data throughput gain of ACM or VCM:

- Evaluate the possible variation of the parameters for the link budget including the identification of worst case, best case, and the respecting range of values in the link budget. The worst case is considered the reference case. This is defined as the case where DVB-S2 CCM is used, i.e. only one modulation scheme and code rate, with the MODCOD 1 (as defined in Table *A-1*)
- Evaluate the variation speed of the link budget parameters to assess whether a dynamically (ACM) or a lower rate (VCM) of change is more convenient
- Evaluate the influence of protocol complexity on the waveform and system parameters

3.4.1 VCM and ACM analysis

The impact of the parameters on the link budget is given in this subsection. Furthermore, the potential benefit of adaptive transmission is analysed.

Waveform hypothesis

The performance assessment is based on the use of DVB-S2. Among the different standards, DVB-S2 is state-of-the-art for end-to-end transmission over GEO telecommunication satellites and is offered through different commercial IPs. The minimum data rate for the link budget depends on the mission requirements. The link budget analysis considers all possible 28 MODCODs as listed in Table *A-1*.

Simulation hypothesis

The simulations depend on the parameters and assumptions listed in *Table 3-2* and *Table 3-3*.

Influence of the ground station location

The different climatic regions of the ground stations impact the link budget. *Figure 3-7* and *Figure 3-8* illustrate the difference for different link unavailability for both ground stations. This shows a difference of up to 5 dB for Stuttgart and up to 11 dB for Banting for the availability of 99.9 %.

Conclusion

The results are the following:

- There is a high dynamic range, even under clear sky conditions (without rain loss)
- This dynamic under clear sky conditions includes the free space loss (ca. 29 dB), and the atmospheric loss (gas and cloud loss)
- There is an additional dynamic range due to the atmospheric losses (rain and scintillation)
- The link budget results highly depend on the elevation angle and on the ground station's location
- The use of ACM allows to increase the data throughput at least a factor of two for the MEO phase and more than a factor of four for the LEO phase, considering the data rate throughput for the whole mission
- The use of ACM allows to increase the data throughput w.r.t. the worst case, i.e. the worst MODCOD for each mission phase

The simulations show that there are large variations in the following link budget parameters: free space loss variation and rain loss as given in Figure *2-12* and Figure *2-13*. The use of ACM provides better performance both in terms of spectral efficiency and minimum data rate. The worst case link budget

case is very constraining. This case would lead to very low data rates for the whole system without ACM use.

Three different cases are listed in *Table 3-7*:

- DVB-S2 CCM with the lowest MODCOD 1. This is also the reference case for the following two cases
- The lowest MODCOD that fulfils the link budget for the corresponding mission phase
- The highest and lowest possible MODCOD that is required to close the link budget for the corresponding mission phase

The data throughput per day was obtained using the average contact times as given in *Figure 3-5* and *Figure 3-6*. The link margin for the 3000 km worst case in *Table 3-5* is very low with 3.7 dB. Thus, the considered assumption is that the most probable solution on a typical mission would be to choose MODCOD 1 as the worst case. *Table 3-7* clearly shows the potential of using ACM for the ROMEO mission: the increase w.r.t. to the first case is up to 436% for Phase 1 and up to 144% for Phase 3. The increase w.r.t. the first test case in the data throughput per day, i.e. CCM MODCOD1, would be even higher if several or all MODCODs would be considered since the third case only considers the minimum and the maximum MODCOD.

3.4.2 Parametric link budget analysis

The following parametric link analysis shows the impact of the free space loss, atmospheric loss, elevation angle, Earth ground station parameters and satellite parameters on the link budget. These parameters depend mainly on the used frequency band, and the orbit type. They partly depend on the ground station location. The following parameters have large variations during a ground station pass and would impact the link budget results.

Table 3-7: Data volume per day for the different mission phases. The IRS ground stations from Table 3-2 were considered for all cases. The MODCODs are according to Table A-1

Condition		**GB/day**	**Increase w.r.t. CCM MODCOD1**
CCM MODCOD1	Phase 1	10.3	-
	Phase 3	19.5	-
CCM min. MODCOD	Phase 1 (MODCOD13)*	41.8	404%
	Phase 3 (MODCOD1)*	26.1	134%
Min. and max. MODCODs	Phase 1 (MODCOD13 and 28)*	45.1	436%
	Phase 3 (MODCOD1 and 28)*	28.0	144%

*MODCODs according to Table *A-1*

Free space loss

The free space loss depends on the link geometry, mainly the slant range as shown in *Figure 2-10*. However, the free space loss varies slowly with the satellite's position over the ground station. *Table 3-4* shows that the mean free space loss difference due to the slant range between the best and the worst case is 11.8 dB in the LEO and 26.1 dB in the MEO phase.

Atmospheric loss

Atmospheric loss increases the lower the elevation angle is as shown in *Figure 2-13*. Furthermore, the atmospheric loss increases the higher the used frequency band or the higher the rain probability in the given location is. This rain loss has to be considered in the link budget calculations. *Figure 3-7* and *Figure 3-8* show the difference in atmospheric loss only for the

ground stations of *Table 3-2* for the best case. Depending on the specified link availability, losses of up to 5 dB for STR and up to 11 dB for MAL have to be taken into account. The heavier the rainfall is, higher atmospheric loss results. Thus, an atmospheric loss of at least 9 dB for STR and 18 dB only for MAL has to be taken into account in the link budget to ensure a robust and reliable data transmission with a link availability of up to 99.99 %.

Elevation angle

The elevation angle depends on the current link geometry as shown in *Figure 2-10* and it indirectly impacts the following link budget parameters:

- The free space loss. The slant range and thus the free space loss is a function of the elevation angle
- The atmospheric loss. The lower the elevation angle, the higher the slant range. A higher slant range means higher atmospheric loss due to tropospheric effects (clouds, fog, gas, rain)
- The antenna gain. Depending on the antenna pointing error, both from the satellite and from the ground station, the higher or lower the boresight gain that can be considered for the link budget. A higher pointing error leads to less gain due to the offset of the boresight gain

The mentioned parameters are independent of system specific architectures. However, system specific parameters are important to consider. The system parameters are divided into the Earth ground station parameters and satellite specific parameters.

Earth ground station parameters

The main parameters for possible ACM use are the antenna gain and the EIRP. These parameters depend on several items. Two cases can be distinguished:

- If several ground station terminals coexist within the system, they typically have different G/T figures. *Table 3-2* shows that the IRS ground stations have the same G/T under clear sky conditions but the location in different climatic regions leads to differences in the rain attenuation [51]. This increases the need for using ACM: in Banting more robust MODCODs are necessary to close the link and the MODCOD change commands should be higher to be able to react to the rain loss
- The antenna boresight gain varies depending on the pointing error. The ground station antennas have a high gain, which leads to a HPBW of 0.21° as listed in *Table 3-2* and thus, increases the pointing requirements

Satellite parameters

The whole ROMEO satellite rotates to point the antennas towards a ground station during a ground station pass. The pointing error influences the boresight EIRP and the pointing loss, which directly impacts the link budget. Furthermore, the used transmission standard and components could strongly impact the link budget but are difficult to determine for the whole mission time. Thus, a safety margin (often named implementation margin) is considered to take account of possible variations for these parameters.

Conclusion

The different parameters of the link budget may vary over time. This can depend on the orbit type, and on the used frequency band. However, several other parameters have large

variations that could make ACM of interest. Section 3.4.1 described their link budget impact and possible gain due to ACM. Yet, among these parameters are differences:

- Parameters with slow variations that can be tracked and compensated through ACM:
  - Free space loss – range of up to 26.1 dB
  - Atmospheric loss due to clouds and gas
  - Satellite antenna pointing errors
  - Earth ground station antenna pointing errors
  - Scintillation effects
- Parameters with fast variation that are difficult to track and should be considered in the ACM margin:
  - Atmospheric loss due to rain
  - Interference due to other carriers in the considered frequency band or due to intermodulation

3.4.3 MODCOD selection concept

Another important parameter is the MODCOD selection. Appendix A shows the E_b/N_0 thresholds for a MODCOD according to [3]. MODCODs 10, 15, 22, and 23 achieve a lower spectral efficiency at higher E_b/N_0 than their nearby MODCODs. MODCODS 11, 16, and 17 achieve a marginally higher spectral efficiency at higher E_b/N_0 and MODCOD 22 practically has the same performance as MODCOD 23. Thus, a higher MODCOD does not necessarily mean a higher E_b/N_0 or lower spectral efficiency. In order to reduce the complexity in the adaptive transmitter designed in Chapter 4, the number of used MODCODs can be reduced.

Figure 3-9 shows an analysis of the ROMEO mission for a subset of possible MODCODs in order to close the link with at least 3 dB margin for different MODCODs at different altitudes for the minimum elevation angle possible. Note that the altitude corresponds to the satellite´s height above the Earth

surface (with the equator as reference), measured along a perpendicular line, while the slant range is the straight-line distance between the satellite and a ground station (refer to *Figure 2-10* for a detailed overview).The lowest MODCODs which use QPSK modulation ensure reliable transmission during the entire mission down to minimum elevation angles. The use of MODCOD1 allows to close the link in each mission phase. This MODCOD allows a reliable contact window with the different ground stations when used at the beginning of each satellite pass, i.e. it allows an error free transmission at already low elevation angles. This is essential for the MEO phase and also for part of the transfer phase. However, in the SSO phase, the minimum MODCOD that allows to close the link is MODCOD13, even for an elevation angle as low as 5°. Therefore, it is not useful to use a MODCOD below MODCOD13 in Phase 1. In this phase even the highest MODCOD28 closes the link down to an elevation of 45°. Thus, especially ground station passes that achieve high elevation angles in the Phase 1 can use modulation schemes like 16APSK and even 32APSK with the different code rates possible for this type of modulation. Furthermore, any MODCOD below MODCOD19 ensures to close the link at 15° elevation, and below MODCOD13 at 5° elevation. In Phase 3 not even all QPSK modulation MODCODs allow to close the link under worst case conditions. Furthermore, the contact time for the higher MODCODs is reduced during Phase 2, compared to Phase 1. Therefore, it is important to select adequate MODCODs in these phases to increase the data throughput while ensuring a reliable data transmission.

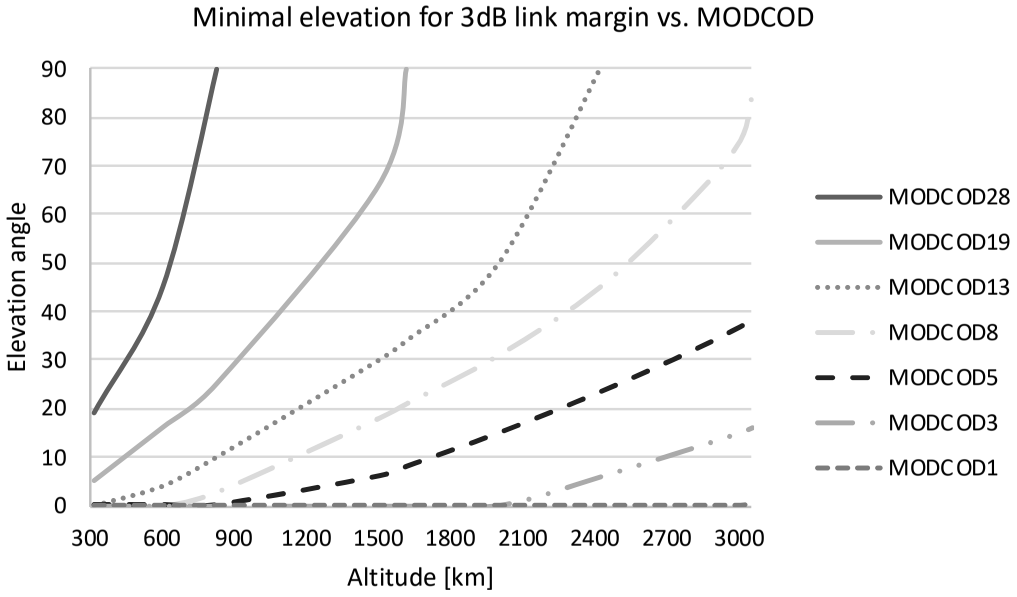

Figure 3-9: Minimum elevation angle as a function of altitude required to close the link with a margin of at least 3 dB margin with different MODCODs

Figure 3-10 shows the mean contact time per day for different MODCODs, considering the assumptions of *Table 3-2* and *Table 3-3*. Note that some of the lower MODCODs allow transmission even under 5° elevation, but in order to define comparable cases, a minimum elevation angle of 5° was chosen. The plot shows the contact time for constant MODCOD. Consider also that the mean contact time is different for the STR and the MAL ground stations. Adding both contact times per day leads to a higher contact time per day compared to considering only one of the ground stations. In *Figure 3-11* the data throughput when using a determined MODCOD configuration are plotted. It shows that the lower MODCODs allow higher throughput. This is due to the higher average contact time for this configuration. Furthermore, the figures show how MODCOD contact time per day and data throughput per day change during Phase 2 and 3. In Phase 3, all MODCODs above MODCOD19 have a maximum contact time of one minute. This is due to the fact that the orbit has a high drift and the condition of a slant range below 1600 km is not ensured so often during a satellite pass. Therefore, it is important to analyze the contact time per day as well as the data throughput for the specific mission phase to specify the optimum MODCOD according to the mission requirements. For the ROMEO mission, the MODCODs above MODCOD13 are well-suited for Phase 1 but not for Phase 3. For Phase 3 only MODCODs below MODCOD19 allow to close the link. Thus, during Phase 2 the change in orbit conditions have to be analyzed continuously during the satellite operation to know which MODCODs can be excluded from the analysis.

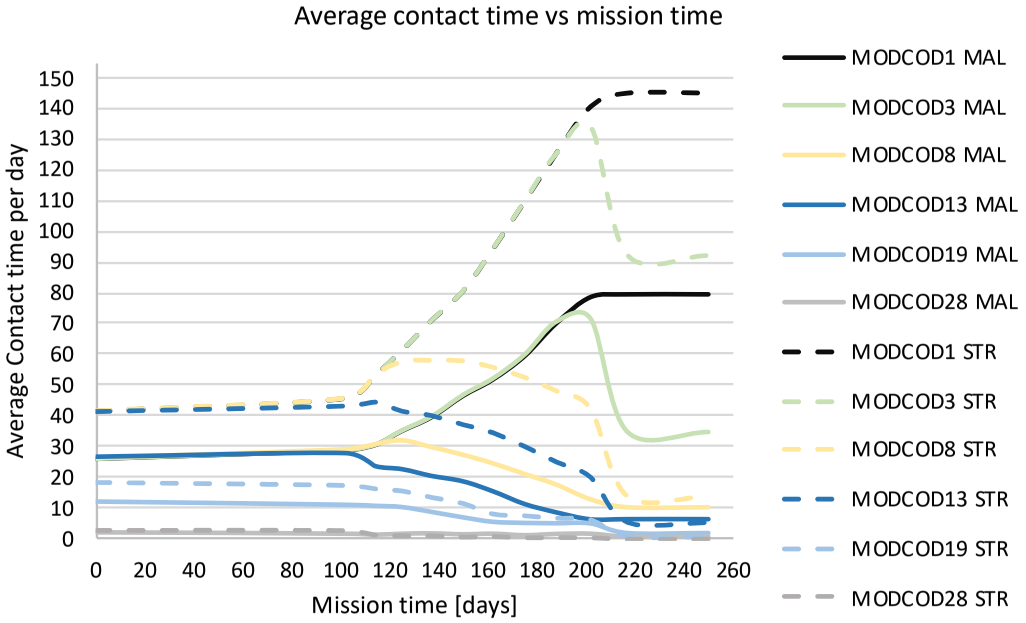

Figure 3-10: Average contact time per day for the STR and MAL ground station depending on the MODCOD used during the mission time. The simulation was based on the parameters and assumptions of Table 3-2 and Table 3-3

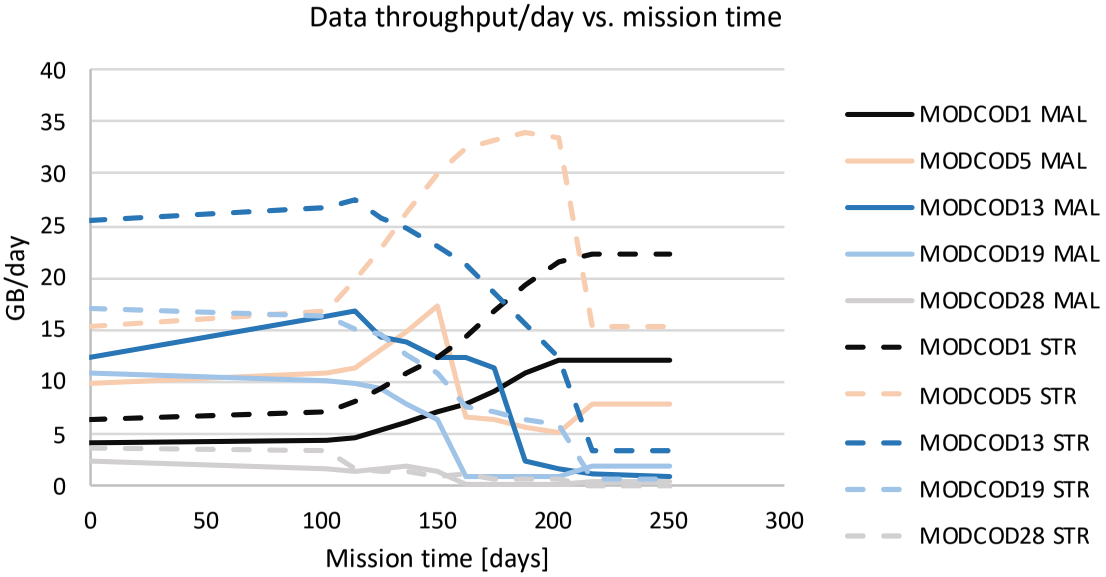

Figure 3-11: Mean downlinked data per day depending on the MODCOD used according to the mission time. The simulation was based on the parameters and assumptions of Table 3-2 and Table 3-3

3.5 Interaction of space segment and ground segment

A typical GEO satellite DVB-S2 ACM link contains the gateway, the satellite, and the receive ground segment. The receiving segment connects to the gateway through a return channel. The gateway is a ground station that transmits data to and receives from the satellite to the local area network. The gateway is equipped with an ACM DVB-S2 modulator. This kind of system can be adapted to small satellite applications. These adaptions on the ground segment relate, among others, to different used bandwidths, and frequency ranges that differ from a typical GEO satellite. Furthermore, the Doppler shift needs to be considered due to the relative velocity between the fast-travelling satellite and the ground station.

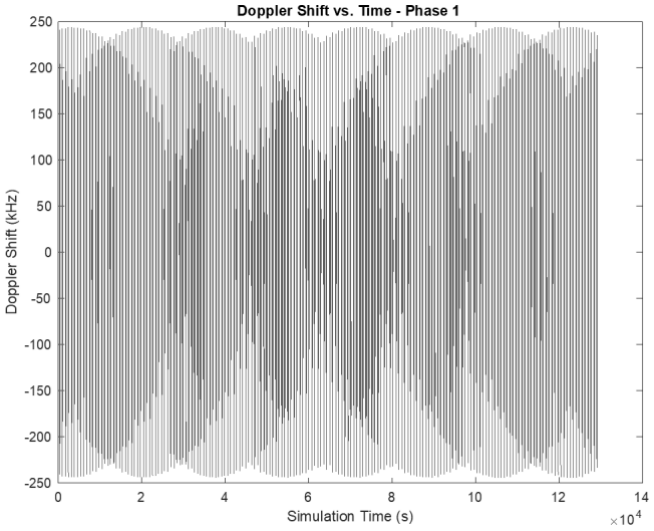

(a)

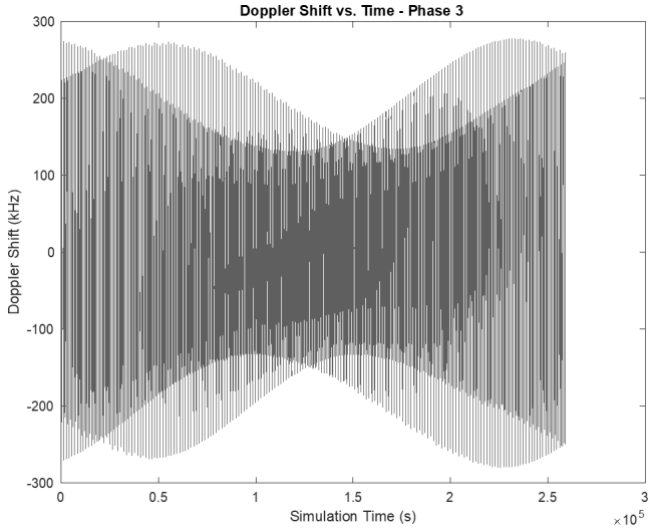
Doppler Shift vs. Time - Phase 3
Doppler Shift (kHz)
300
200
100
0
-100
-200
-300
0
0.5
1
1.5
2
2.5
3
Simulation Time (s)
×10^5

(b)

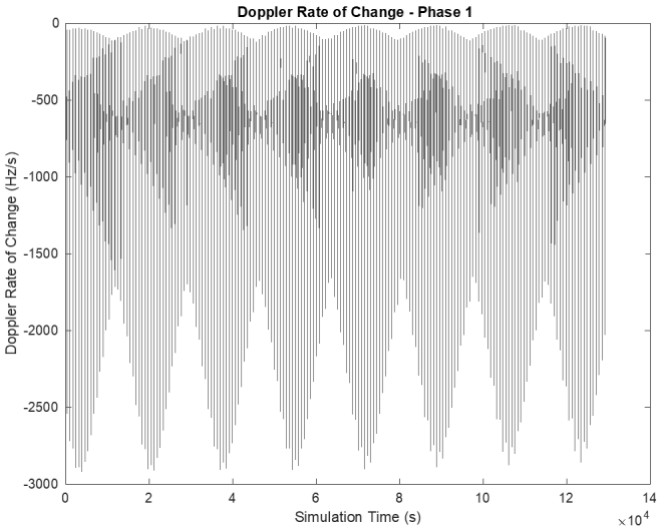
Doppler Rate of Change - Phase 1
Doppler Rate of Change (Hz/s)
0
-500
-1000
-1500
-2000
-2500
-3000
0
2
4
6
8
10
12
14
Simulation Time (s)
×10^4

(c)

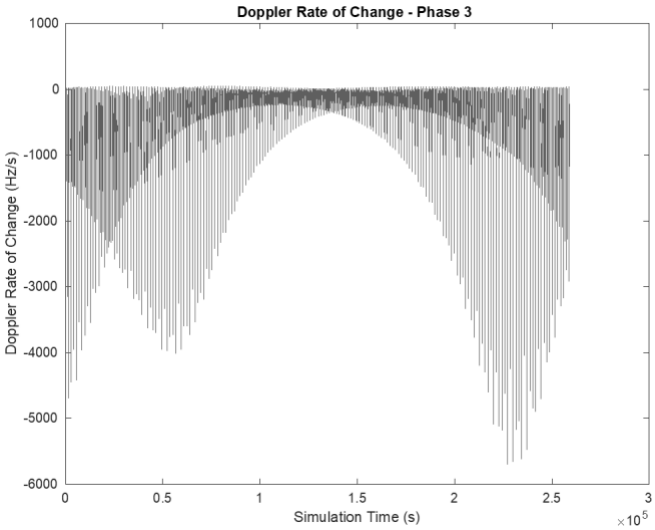

(d)

Figure 3-12: Doppler shift and Doppler rate simulated with MATLAB according to parameters listed in Table 3-3. The Doppler shift during Phase 1 is shown (a) and during Phase 3 in (b). The Doppler rate of change during Phase 1 is shown in (c) and during Phase 3 in (d). For all simulations a carrier frequency of 10.475 GHz was used and the simulation time was set to 3 months for Phase 1 and to 6 months for Phase 3, corresponding to the intended mission phase times

Using the parameters listed in *Table 3-3*, a simulation was performed to calculate the expected Doppler shift and Doppler rate for the ROMEO mission during ground station passes of the STR ground station (see parameters in *Table 3-2*). The simulation results are shown in *Figure 3-12*. The Doppler shift increases during the ROMEO mission from ca. ±250 kHz in Phase 1 to ca. ±270 kHz in Phase 3. The Doppler rate of change increases from ca. ±3 kHz/s in Phase 1 to ca. ±5.7 kHz/s in Phase 3. These values have to be considered when choosing the

modem for the ground segment (as well as the receiver of the ROMEO satellite) since standard Doppler limits for ground modems are ±200 kHz and ±2 kHz/s.

The high-level architecture of the link with ACM for a small satellite like ROMEO is shown in *Figure 3-13*. Within the space segment, the adaptive X-band transmitter receives data from a mass memory. This data is processed according to the DVB-S2 standard. The PA module amplifies the signal and then feds it to the antenna. The antenna sends the signal out, which then travels through the transmission channel. The transmission channel introduces loss that mainly depends on the slant range, the atmospheric conditions and the pointing error.

The antenna of the ground station receives the signal that the adaptive X-band transmitter sent with a defined MODCOD. The ground station pass initiates with the most robust MODCOD as defined for the mission phase. The signal is amplified and then passed to a modem that downconverts, demodulates and decodes the received signal. The modem extracts the current MODCOD information and determines the current E_b/N_0. This information is fed into the ACM estimator. If the E_b/N_0-level is outside predefined minimum and maximum limits, the ACM estimator calculates the optimum MODCOD for the current transmission state and generates an ACM MODCOD command with the optimum MODCOD. This optimum MODCOD information is used to create a CCSDS-compatible telecommand that is sent back to the satellite.

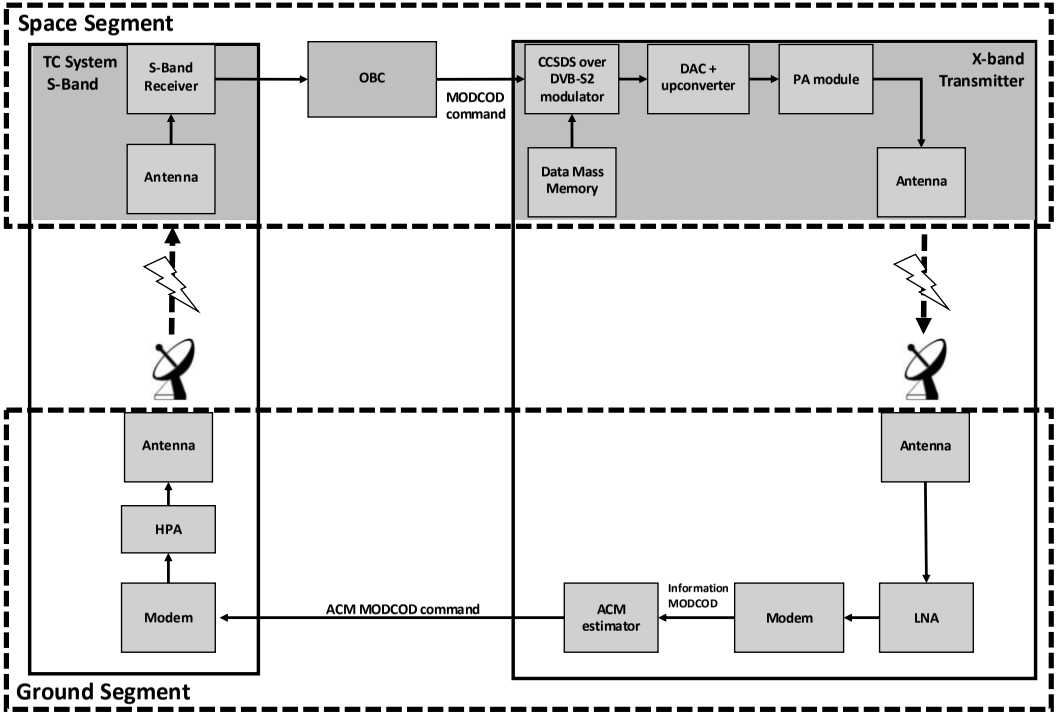

Figure 3-13: Interaction of the space and the ground segment

The telemetry and telecommand ground stations typically operate in the space research S-band. This corresponds to 2025 - 2100 MHz for telecommands and 2200 - 2290 MHz for telemetry. The transmission channel introduces loss that depend on the slant range, the atmospheric conditions and the pointing of the satellite's and ground station's antenna. The S-band telecommand system of the satellite receives the telecommand through the antenna, forwards it to the receiver where the telecommand is demodulated and decoded. This ACM telecommand reaches the OBC that extracts the information of the optimum MODCOD to be used. This information then is forwarded to the adaptive transmitter that changes its current transmission accordingly. This loop remains active during the entire satellite pass.

Table 3-8: Overview of the different delays for the satellite mission

Parameter	**600 km altitude**		**3025 km altitude**		**314 km altitude**	
Elevation [°]	5	90	5	90	5	90
Delay due to slant range [ms]	8	2	21	10	5	1
Delay due to processing of the OBC [ms]	1					
Delay resulting from SNR measurements on ground [ms]	300					
Total delay [ms]	309	303	322	311	306	302

The loop delay determines the quality of the adaptivity of the transmission. The delay differs for each satellite mission. The loop delay depends on the slant range, the OBC, the transmitter MODCOD adjustment, the ground modem, and the MODCOD decision after the E_b/N_0 measurement. Considering the ROMEO mission with its Phase 1 at the altitude of 600 km the delay at 5° elevation is 8 ms and with 90° elevation 2 ms. In comparison, for Phase 3, 5° elevation corresponds to a delay of 21 ms at 3025 km and 5 at 314 km. Even the best case, at 90° elevation at 3025 km still has a delay of 10 ms which is more than the worst case at 600 km. Assuming an OBC with a clock frequency of 35 MHz results in a delay of ~1 ms. The assumed transmitter adjustment delay is 10 ms. The delay in the SNR measurement depends on the measurement accuracy and the algorithm. For worst-case calculations, delays of up to 300 ms are expected to counteract for all delays in the different ground segment subsystems. This should allow to be within the DVB-S2 recommended error standard deviation better than 0.3 [42]. Table *3-8* shows an overview of the total loop delay. It considers the delay on the slant range, the OBC, the transmitter adjustment and the MODCOD decision after the SNR measurement on-ground.

4 Design of an adaptive transmitter system

The previous chapters gave an overview about different transmission systems for space applications and analyzed the advantages and drawbacks of different transmitter architectures, based on the ROMEO use case. The design approach of an adaptive transmitter system for this mission, including the trade-off for the transmitter architecture as well as the detailed overview of the different components are described in this chapter.

4.1 Requirements

The main challenges on the design of the adaptive transmitter are the compatibility between the different components, the ACM mode implementation, the power consumption and the space environment. The system level approach combines radiation-hardened and COTS components with technologies for fault mitigation to provide a reliable and scalable transmitter. *Table 4-1* lists the main requirements and how they are intended to be verified and tested in this thesis. The requirements for the maximum permissible bandwidth are defined in [54], the minimum data volume per day are derived the ROMEO data budget [49] and the RF output power and antenna gain are defined in *Table 3-6* according to the minimum required EIRP calculation in 3.3.2. The power consumption and radiation tolerance requirements have been derived from the ROMEO power budget and the radiation simulation [50]. The CCSDS requirement for the physical layer and the data link layer ensures compatibility to the entire IRS ground station network and the DVB-S2 standard an adaptive quasi error-free transmission according to [3].

Table 4-1: Overview of the ROMEO adaptive transmitter requirements and the corresponding verification method

Parameter	**Requirement**	**Verification method**
Frequency band	Ham radio X-Band (10.45 - 10.5 GHz)	Test
Bandwidth	50 MHz max.	Test
Data Volume	Min. 15 GB/day	Analysis
Data rate	Variable	Test
RF output power (saturation)	33 dBm, according to 3.3.2	Concept analysis
Antenna gain	Min. 16 dBi, according to 3.3.2	Simulation
Power Consumption	20 W	Concept analysis
CCSDS compatibility	Yes	Test
Coding and modulation	DVB-S2 standard	Test
Radiation tolerance	TID 8.2 krad min., according to [50]	Concept

The next section shows the trade-off for the adaptive transmitter architecture that can fulfill the requirements listed in *Table 4-1*.

4.2 Architecture trade-off

The transmitter architecture options B, C and D, as defined in 2.2, are considered for this trade-off since option A, where the DAC is before the SRRC filter, does not allow to implement complex digital signal processing as required by the DVB-S2 standard.

In the direct transmitter in option D all signal processing is placed in the digital domain. To achieve the required output frequency at 10.475 GHz, the DAC must have a high sampling

rate above 20.95 Gsps in order to fulfil Eq. 2-5 [36]. Yet, it is also possible to reconstruct the signal when Eq. 2-5 is not fulfilled using bandpass sampling. This technique allows to reduce the sampling rate requirements of the DAC compared to using the Nyquist-Shannon theorem. Such a technique could be implemented with the AD9161 from Analog Devices [55]. Yet, this and other available DACs, as shown in *Table 4-2*, do not have a sufficient output bandwidth to generate the desired signal at 10.475 GHz or exceed the financial budget of ROMEO like the EV12DS460AZP from Teledyne e2v [56]. Furthermore, these are only available in ball grid-array design, which complicate the board layout and its assembly. Also, these high-speed class DACs require the JESD204B interface in FPGAs with corresponding serializers that increase the interface complexity.

Table 4-2: Comparison of direct conversion DACs

Parameter	**AD9161**	**AD9162**	**EV12DS-360AZP**
Resolution	11-bit	16-bit	12-bit
Max. sampling rate	12 Gsps	12 Gsps	7 Gsps
Max. Direct RF conversion	7.5 GHz	7.5 GHz	12 GHz
Interface	JESD204B	JESD204B	LVDS
Power consumption	2.65 W @5 Gsps	2.65 W @5 Gsps	3 W
Cost	130€	130€	6000€

The low-IF transmitter of option C offers the advantage of a large available number of COTS components in the required frequency range. Thus, a replacement is easy to find if a component is not available. Yet, an image frequency is generated during the conversion, which would have to be suppressed by means of a steep filter. This makes a compact

implementation less practicable due to the high required filter order. To eliminate the disadvantage of the low-IF transmitter, the image frequency can be suppressed by a suitable second mixer, as in the zero-IF transmitter in option B. The COTS market offers available ICs that integrate two mixers and the 90° phase splitter. A disadvantage is that only a few mixers from one manufacturer are available in the desired frequency range. This entails disadvantages in the event of availability problems in case of obsolescence or supply problems. The detailed component trade-off for the DAC and the upconverter for these architectures is explained in 4.5.

Table 4-3 gives an overview of the various options and their specific properties, considering also the price and the power consumption of the available DACs. Comparing the alternatives shows that the zero-IF and the low-IF architectures show the most promising results. Since the COTS components offer the possibility to operate with complex as well as analogue baseband, both the zero-IF and the low-IF architecture are further considered in the design. Thus, the choice of a zero-IF or a low-IF architecture is driven by output signal quality and interface compatibility, which is analyzed in chapter 4 and 5.

4.3 Overview

An overview of the high-level architecture of the ROMEO satellite including the core avionics and the adaptive transmitter is shown in Figure 4-1. The adaptive transmitter can be divided into two subsystems: the ham radio X-band transmit processor (XTra-Pro) and the RF analogue frontend. An additional power supply board for the PA module is necessary since the power amplifier typically require higher voltages (20-50V, depending on the PA) than the other components. The XTra-Pro is part of the core avionics system of ROMEO, which mainly acts as the on-board data handling (OBDH) system.

Table 4-3: Trade-off between the transmitter architectures for the ROMEO mission

Parameter	**Zero-IF**	**Low-IF**	**Digital**
Practicability	Moderate, due to price, complexity and component availability	High, due to price, complexity and component availability	Low, due to price and component availability
Effort	Low, well-known components and interfaces	Low, well-known components and interfaces	High, due to interface complexity
Price	Low, ca. 500 €	Low, ca 500 €	Up to 6000 € only for the DAC
Power consumption	Low to moderate, up to 2 W for the DAC	Low to moderate, up to 2 W for the DAC	3 W only for the DAC
Component availability	Many COTS components available	Many COTS components available	Low, few DACs available for RF conversion

The main component of the core avionics is the SoC that features the digital signal processing algorithms of the adaptive transmitter functions but also hosts OBDH functions. The OBDH functions are being developed within another PhD thesis and are thus not within the scope of this thesis. Yet, the high-level architecture design according to the ROMEO requirements was done in collaboration. The following OBDH functions are provided by the SoC:

- interface to the bus components, as an example in *Figure 4-1* the X-band analogue frontend
- running the on-board software
- monitoring/reading sensor values of the different bus components
- commanding the bus components
- performing the satellite configuration management and the attitude and orbital control algorithms
- providing the data interfaces
- providing the clocks
- performing error detection and correction (EDAC) and failure detection, isolation and recovery (FDIR)

Due to the orbit characteristics of the ROMEO mission, the satellite travels through the inner Van Allen belt. Since the used SoC is not a space-grade component and is not radiation hardened (components that by design achieve a TID beyond 100 krad), different radiation mitigation techniques have to be considered and implemented in the processing system (PS) and the programmable logic (PL). Furthermore, a radiation hardened supervisor for the SoC, the Vorago M4 [57] was chosen. The main characteristics of the Vorago M4 can be found in *Table 4-4*.

The supervisor acts as a watchdog to monitor correct functionality of the SoC during operation and during the boot

process. Thus, it permanently checks the heartbeat (periodic signal generated to indicate nominal operation or for synchronisation) of the PS and the PL and provides a time synchronisation heartbeat. Furthermore, it supervises the configuration pins of the SoC during booting and, in case of a fault during the boot process or detection of a faulty boot image, it can force to boot the “golden” image. The boot image is a configuration file that is necessary to boot, i.e. to start, the SoC. The “golden” image is an image defined at launch, which will remain identical during the whole mission. The boot images for the SoC are contained in configuration memories. Since the images could have faults, separate memories are used in order to improve the reliability. One of the memories, which is radiation hardened, contains the “golden” image. The other memories contain updated images which have been uplinked during the ground station passes. Scrubbing is used on these memories for error detection.

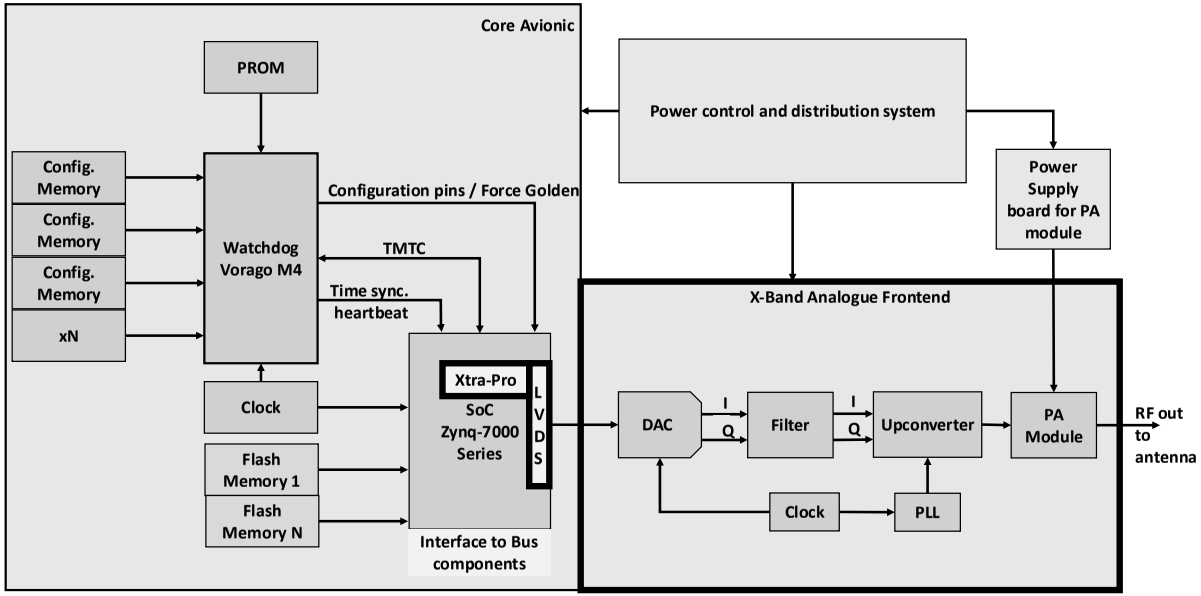

Figure 4-1: High-level architecture of the ROMEO satellite including the core avionics system, the power control and distribution system and the adaptive transmitter with its XTra-Pro and the X-band analogue frontend. The components outlined in bold correspond to the components developed here. This architecture corresponds to a zero-IF transmitter architecture

Table 4-4: Main characteristics of the Vorago M4 [57]

Processor	32bit ARM Cortex M4
Clock rate	100 MHz
Memory	64 kB on-chip data 256 kB on-chip program memory SRAM EDAC Memory scrubbing
Radiation tolerance	TID > 300 krad Soft Error Rate with EDAC and scrubbing enabled < 1e-15 errors/bit-day Latch up immunity LET > 110 MeVcm^2/mg

The check for failures does not have to be fast but reliable since the images are only needed for the boot process of the SoC. The data of the memories is read and forwarded to the SoC through the supervisor. The boot image of the supervisor is saved on a radiation hardened programmable read-only memory (PROM). The scientific and telemetry data are stored into mass memories. The data is written in parallel into N flash memories. A checksum is used to detect errors that could be introduced during data storage or transmission. To detect failures and bit-flips in the memories, these are scrubbed. Thus, the data is read, the bit errors (if any) are corrected with an Error-Correcting Code (ECC), and the corrected data is written back to the memory. The architecture also contains the power supply as well as the power distribution network to provide each component with its corresponding voltage and voltage ranges. To control these value ranges, input/output (IO) controllers are provided. In order to detect latchups, a latchup protection circuit is implemented. The manufacturer AMD Xilinx defines defines a latchup as an increase in current of at least 100 mA in less than 10 µs [58]. The protection circuit monitors the current on the power rails and if it is above a defined threshold, the single component or the whole power rail is reset.

An overview of the high-level architecture of the transmitter is shown in *Figure 4-2*. The main component of the XTra-Pro is the SoC, a hardware component which consists of a dual-core PS and a PL implemented on an FPGA. The CCSDS and the DVB-S2 protocol stacks as well as the corresponding digital signal processing are implemented in the PL while the configuration management, the status control and the commanding are handled by the PS. The XTra-Pro is part of the core avionics system of ROMEO, as shown in *Figure 4-1*. Thus, the SoC is used by different subsystems. After the XTra-Pro, the complex baseband signal is transmitted via the ham radio X-band analogue frontend, which consists of several hardware components. The digital in-phase and quadrature sampled signals have to be converted into an analogue signal. This is done with a dual-channel DAC. The use of a Low-Voltage Differential Signaling (LVDS) interface enables reliable transmission and data rates sufficient for the link budgets analyzed in 3.3. The dual-DAC has a first-in first-out (FIFO) buffer at its input to compensate delay variations of the incoming data. After up-sampling, the sampled signals are passed through adjustable interpolation filters. The output signal of the dual-DAC can either be directly output or additionally filtered by low pass filters. This complex signal is then passed to the upconverter which consists of a quadrature mixer. This scheme enables upconversion of the complex signal to the required carrier frequency. The RF signal is fed to the PA module that amplifies the RF signal. The amplified signal is then fed through a 50 Ω coaxial cable to the antenna and transmitted at the air interface.

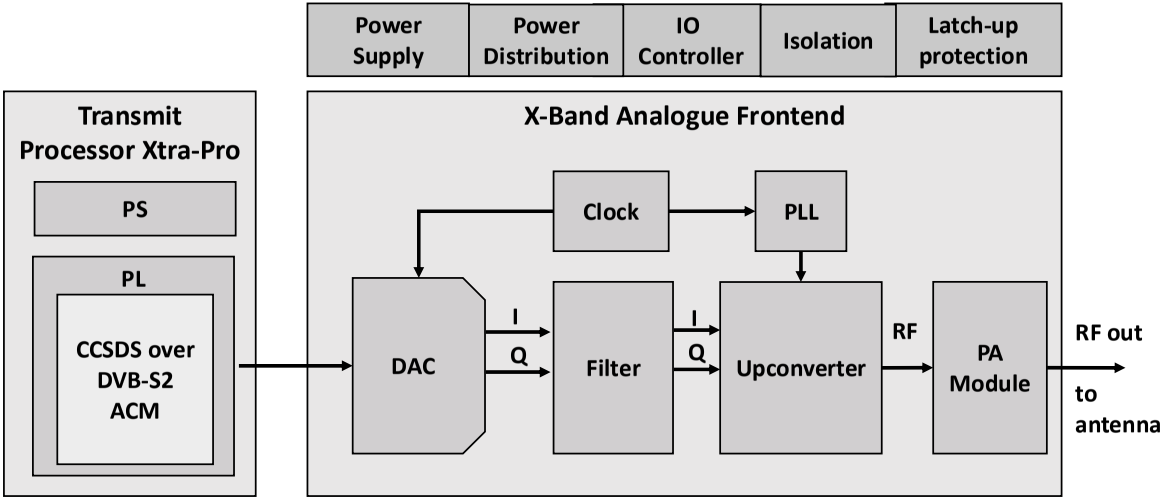

Figure 4-2: High-level architecture of the X-band transmitter for ROMEO, representing the corresponding partial area of the X-band transmitter from Figure 4-1

All components have to be chosen in terms of their relevance to the survival of the satellite bus since the OBDH and the communication system share the same SoC, as described in more detail in 4.4.2. Thus, the most critical component of the transmitter is the SoC since at least the PS will always be on in order to receive commands from the on-board computer and to monitor the different components from the analogue frontend. The other components will only be switched on during a ground station pass. Thus, a "careful-COTS approach" was chosen to select either a COTS SoC which is radiation-resistant by design or to consult databases of radiation tests for different COTS SoCs. Radiation-resistant SoCs are too expensive for this university satellite mission and therefore components were searched in radiation databases. The chosen SoC is the Zynq-7020 from the AMD Xilinx Zynq-7000 series since it has been implemented on several NASA CubeSats, multiple ISS missions, has extensive flight heritage [59] and meets the requirements regarding power consumption and FPGA resources. The main characteristics of the AMD Xilinx Zynq-7000 series SoC are described in *Table 4-5*. The DAC, the Phase-Locked Loop (PLL) and the upconverter were chosen to meet the mission requirements since no significant information was available in the radiation databases for these components. To further protect the transmitter, it will be ensured that a radiation shielding which is equivalent to a 10 mm full sphere of is used to protect the electronics as well as a latch-up protective circuit that interrupts the power supply via a switch as soon as an anomaly in the current flow is detected. This shielding should minimize the TID effect from over 40 krad down to 5.4 krad according to the radiation analysis in [50]. Yet, this shielding was neither implemented nor tested during this thesis.

Table 4-5: Main characteristics of the AMD Xilinx Zynq-7000 (XC7Z020) [60]

Parameter	**Value/Function**
Processor core	Dual-core ARM Cortex-A9
Maximum clock frequency	Up to 866 MHz
On-Chip memory	256 KB
PS to PL Interface ports	2x AXI 32-bit Master 2x AXI 32bit Slave 4x AXI 64bit/32bit memory AXI 64-bit Accelerator Coherency Port (ACP) 16 interrupts
PL	Artix 7 FPGA
Programmable logic cells	85K
Look up tables (LUT)	53200
Flip-Flops (FF)	106400
Block RAM	4.9 Mbit
DSP slices	220

Since the power resources on the ROMEO satellite are limited, a preliminary power budget for the different components of the adaptive ham radio X-band transmitter was established which is shown in *Table 4-6*. The expected power consumption is based on typical power consumption of the available components in the frequency range used. Most of the power consumption is allocated to the PA module. The power consumption of the components is part of the trade-offs presented in the following subsections. The verification and the comparison of the measured and expected power consumption is shown in 5.1.2 for the XTra-Pro and in 5.2.1.5 for the analogue frontend. The detailed architecture and trade-off for

the components is explained in 4.4 for the SoC and in 4.5 for the components of the analogue frontend.

Table 4-6: Preliminary power budget for the adaptive ham radio X-band transmitter

Component		**Expected power consumption**
XTra-Pro	XTra-Pro, AMD Xilinx Zynq-7020	2.5 W
Analogue Frontend	DAC	2.5 W
	Upconverter	3.0 W
	PLL	2.0 W
PA module		10 W
Total		20 W, according to *Table 4-1*

4.4 Detailed architecture XTra-Pro

The detailed architecture of the XTra-Pro is described in this section. First, an overview of the interaction between the XTra-Pro and the core avionics is given in 4.4.1. The detailed architecture is explained in 4.4.2 and in 4.4.3 the functionality DVB-S2 IP core is evaluated. In 4.4.4 the interaction with the analogue frontend is outlined.

4.4.1 Interaction core avionics and XTra-Pro

Since the XTra-Pro is part of the core avionic's SoC, the interaction between the core avionics and the XTra-Pro has to be defined. The interaction between both systems is performed by the supervisor that monitors and controls the SoC and thus

the XTra-Pro functionality. The finite state machine which monitors and controls the SoC's boot process and operation is shown in *Figure 4-3*. Its main purpose is to enable safe operation of the SoC. States and state transitions are described in the following:

- *SoC power off*. The SoC is without power. If it is commanded by a telecommand (TC), the supervisor will change its state to SoC power on
- *SoC power on*. The supervisor enables the power rails to power up the SoC. A series of voltage regulators are used to generate the various voltages required by the SoC and its peripherals. A dedicated circuit returns a "power good (PG) signal" to an array of supervisor pins. The finite state machine transitions into *Ready2Boot*, if all PG signals are set high ("1"). Otherwise, the state will change to *Faulty* triggering the supervisor to retry powering up the system
- *Ready2Boot*. The supervisor sets the boot partition pins according to a previously set configuration to let the SoC either boot from its "golden" image or from one of the other stored images. The boot timeout timer is started and the defined pins are pulled to high to start the SoC's boot process. The finite state machine transitions to *Booting*
- *Booting*. The finite state machine is idle until an external TC or another signal disables the boot timeout timer. This external TC or signal confirms a successful boot of the SoC and leads the finite state machine into the *Operational state*
- *Operational*. The SoC is in the operational state and will transition into the *Faulty PS* or *Faulty PL* if the heartbeats of the PL or the PS are lost, respectively
- *Faulty PS/Faulty PL*. Two watchdog tasks supervise the PS and the PL section of the SoC. If the respective

heartbeat is lost, the state machine will transition into the *Faulty PS* or *Faulty PL* state

- *Faulty*. The finite state machine will transition into the Faulty state if a latchup event is detected at any time during the boot sequence or during operation of the SoC. The Faulty state can also be accessed by a timeout during booting, missing PG signals or loss of the PL and/or PS heartbeat. The supervisor will power down and restart the entire SoC to prevent damages to the components. If the restart subsequently fails more than a specified number of tries, the supervisor will shut down the SoC's power until further TCs are received

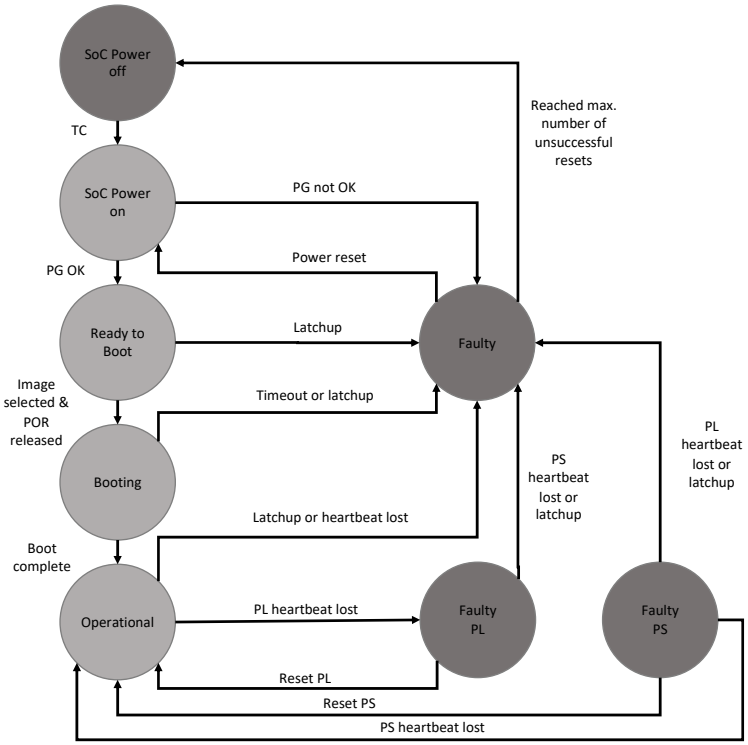

Figure 4-3: Finite state machine of the SoC booting process which is controlled through the Vorago M4 supervisor

4.4.2 Detailed architecture of the XTra-Pro

An overview of the XTra-Pro architecture is shown in the *Figure 4-4*. The PL can perform digital signal processing up to a clock rate of 150 MHz. The CCSDS and the DVB-S2 protocol stacks are implemented in the PL while the satellite configuration management, the status control and the commanding are handled by the PS. The programmable logic consists of a data interface to the data source (mass memory, i.e. flash memory in *Figure 4-1*), the CCSDS Packet Telemetry Encoder (PTME) IP core, a buffer supporting a variable data rate, the DVB-S2 IP Core (which is described in more detail in 4.4.3) and the LVDS interface to the DAC. The PTME IP core is part of the IP core portfolio licensed by the European Space Agency (ESA) and is used on several ESA missions and other missions of the ESA member states. Since any implementation of DVB-S2 is complex and since there are several commercial IP cores available, it was decided that a DVB-S2 IP core should be used for the ROMEO mission.

The implementation of the interface between the CCSDS protocols and DVB-S2, i.e. the ASM and the CADU, had to be analysed for this study. The interface is a data-pull interface [61]: the XTra-Pro periodically requests for and gets data streams. The data source at the XTra-Pro input is the mass memory. The master component is the XTra-Pro and the slave component is the mass memory. The internal clock frequency (83.10 MHz) is twice the symbol rate (41.55 Mbps). The XTra-Pro has an internal buffer to store data before processing it. The data-pull interface allows to exchange an unframed stream or an entire CADU of data, as discussed in 2.4, between the data source and the XTra-Pro. The CCSDS PTME IP Core and a buffer are inserted between the data source and the DVB-S2 IP Core. These transmit the “data_request” signal from the DVB-S2 IP Core to the data source as well as the “data_valid” signal from

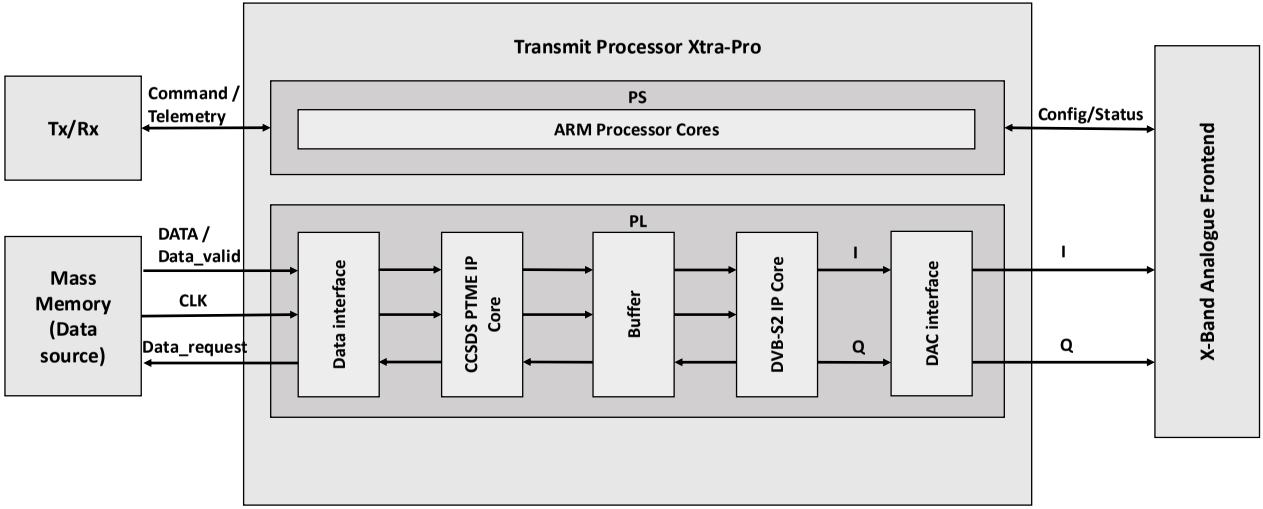

Figure 4-4: Overview of the XTra-Pro architecture and its interfaces to the analogue frontend, the mass memory and the telecommand and telemetry system. For the overview of the XTra-Pro with the core avionics see Figure 4-1, and for the overview of the XTra-Pro with the X-band analogue frontend see Figure 4-2

the data source to the DVB-S2 IP Core. When the PL receives the command of the PS to downlink data, the XTra-Pro sets the “data_request” signal to “1”, and thus the data source begins to send the stored data to the XTra-Pro. In ACM mode, the data must be sent with a data rate higher than the maximum achievable one by the XTra-Pro. Thus, the buffer is filled and the XTra-Pro stops requesting data: the “data_request” signal is set to “0”. Then, the buffer is dumped and after reaching a minimum filling value, the XTra-Pro requests data again (“data_request” = 1). The “data_valid” signal is used by the XTra-Pro to detect when data are received. The DVB-S2 standard specifies a constant symbol rate. Thus, the ACM required input data rates at the XTra-Pro depend on the chosen MODCOD.

4.4.3 Evaluation of the DVB-S2 IP Core

Several DVB-S2 IP cores with different features are commercially available. For the ROMEO mission the DVB-S2 IP core from IPrium [62] was chosen due to the resource utilization on the target SoC and the cost. In a first step, this IP core was tested. The core implements the DVB-S2 standard according to [3] and can be used on an FPGA using the supplied netlist. The input and output parameters of the IP core are shown in *Figure 4-5*. The IP core consists of an 8-bit wide input data bus (*idat*) and inputs for setting parameters such as MODCOD (*imodcod*), symbol rate (*isample*), output gain (*igain*), roll-off factor of the output filter (*iroll*), main system clock (*iclk*), pilot insertion (*ipilot*), and LDPC frame size (*isize*). The input *irst* resets the IP core when set high, *isop* is a sync-word byte marker that can be adjusted. The modulated signal can be output either at an intermediate frequency or in complex baseband (*ifreq*). The digital in-phase (*odati*) and quadrature signal (*odatq*) is made available as a 16-bit wide data bus.

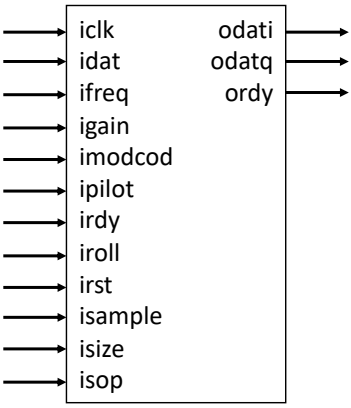

Figure 4-5: Block diagram of the IPrium DVB-S2 IP core

The inputs *irdy, ival* and the output *ordy* control the data flow, as shown in *Figure 4-6*. The *ordy* signal controls the input data flow. The output of the data can be controlled by the *irdy* signal. The *ival* signal specifies whether the incoming data should be processed or if dummy frames should be provided in its place.

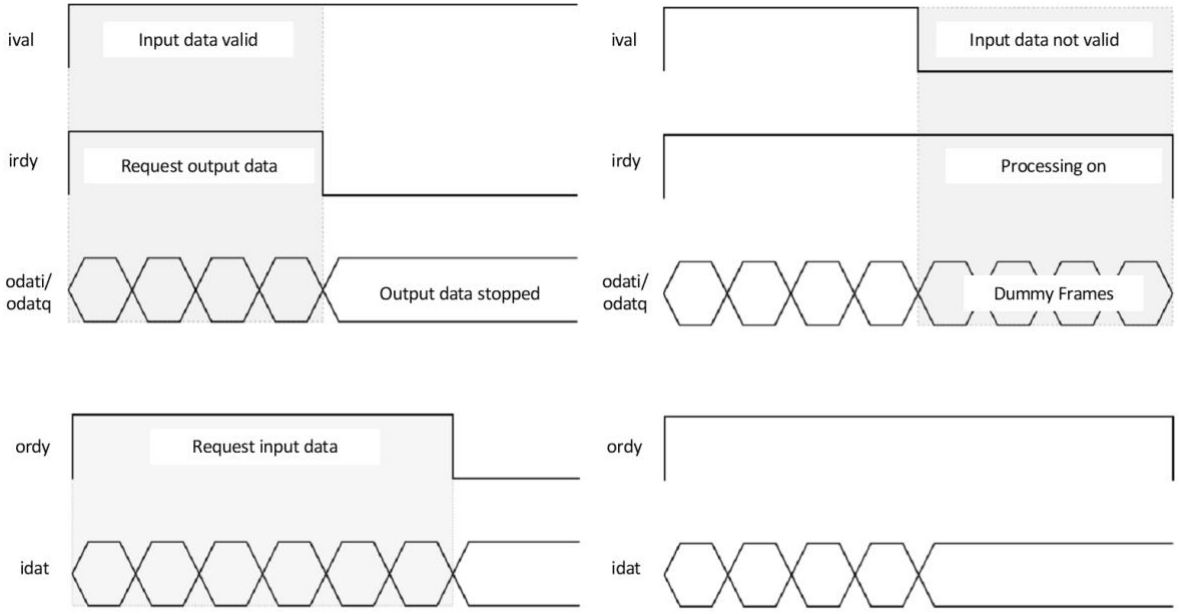

a) If ival and irdy are set high, the transmit signal is output while new input data can be processed. If the output data is stopped, limited further input data can be processed internally.

b) If no new input data is available, dummy frames are sent

Figure 4-6: Data flow control for the IPrium DVB-S2 IP core

The DVB-S2 IP core was implemented, tested and verified with the Vivado tool of AMD Xilinx (for more information see Appendix B). The Vivado workflow can be divided in the following steps:

- Register Transfer Level (RTL): this is the fundamental design step when using FPGAs. The RTL design uses hardware description language (HDL) such as Very High Speed Integrated Circuit Hardware Description Language (VHDL) or Verilog. More advanced tool chains can include a high-level synthesis flow or an IP-based graphical design flow so that it is not required to write HDL. The HDL code can be verified using a behavioral simulation, which can be done with the Vivado simulator or with an external simulation tool. With the used DVB-S2 IP core, a test bench for the behavioral simulation is included. This testbench was used to verify that the data flow control works as visualized in *Figure 4-6*
- Synthesis: a netlist that consists of the generation of circuit elements is created in the synthesis step. This netlist is not device-specific. The design can also be restricted to specific areas on the FPGA if necessary, for example for radiation mitigation strategies
- Implementation: the synthesized netlist is translated into a vendor-specific netlist. Being device-specific, the elements in this netlist can now be placed on the target FPGA by assigning them to the available resources. Finally, the connections between the elements are implemented using the available routing resources. In addition, a static timing analysis can be performed in this step
- Bitstream generation: after the implementation, a bitstream is created automatically with Vivado. The bitstream contains the description of the hardware logic, routing and the initial values for the registers

and the on-chip memories. This bitstream is loaded into the configuration memory of the FPGA to upload the design into the FPGA.

Figure 4-7 shows the test setup used for the evaluation of the DVB-S2 modulator IP core before implementing the netlist on the own design, as recommended by the supplier IPrium. For testing the DVB-S2 IP core, IPrium provided a DVB-S2 firmware file that could be loaded onto a specific hardware in order to test the IP core. The test setup was implemented using the software-defined radio ADALM-PLUTO (PlutoSDR) [63], which is a development platform. The main characteristics of this platform are listed in *Table 4-7*. It contains the AMD Xilinx Zynq 7010 SoC, which pertains to the AMD Xilinx Zynq-7000 series, and the AD9363 transceiver chip. The Zynq 7010 is similar to the Zynq 7020 chosen for the ROMEO mission, the main difference is the number of logic elements and the maximum clock frequency as shown in *Table 4-8*. The SoC of the PlutoSDR contains less logic elements than the Zynq 7020 but for the evaluation of the IP core it is considered sufficient to test it on a FPGA of the same family. The maximum clock frequency allows to work up to a symbol rate of 30 Msps, which is below the maximum symbol rate of ROMEO but still considered sufficient in order to test the DVB-S2 modulator IP core functionalities.

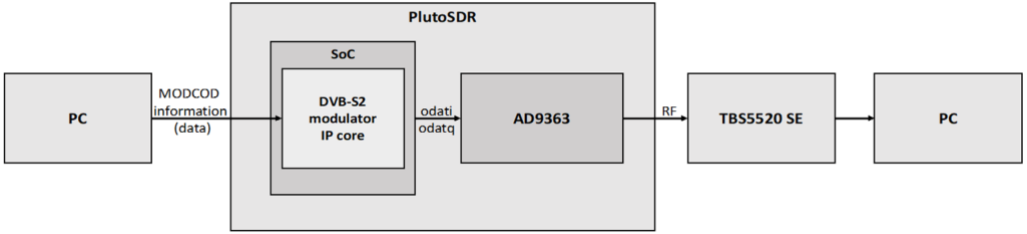

Figure 4-7: Test setup for the evaluation of the DVB-S2 modulator IP core from IPrium. The configuration settings for the DVB-S2 IP core are set with the PC USB interface. The DVB-S2 IP core sets the configuration parameters according to the received settings and starts processing the data. The AD9363 transceiver converts the digital signal into an RF signal with a 1450 MHz centre frequency, which is sent to the TBS-5520 SE. This device is configured via the PC interface. The TBS-5520 SE demodulates and decodes the DVB-S2 signal

Table 4-7: Main characteristics of the ADALM-PLUTO

Specifications	**Typical**
RF Performance based on Analog Devices AD9363	
Instantaneous bandwidth	Up to 20 MHz
ADC/DAC resolution	12-bit
Operation	One Tx and one Rx, half or full duplex
Tuning range	From 325 MHz up to 3.8 GHz
Tx output power	7 dBm
EVM	-34 dB (2%)
Digital	
FPGA logic cells	28k
DSP slices	80

Table 4-8: Differences in the programmable logic (PL) between the Zynq 7010 and the Zynq 7020 [60]

Parameter	**Zynq 7010**	**Zynq 7020**
Programmable logic cells	28K	85K
LUTs	17600	53200
FFs	35200	106400
BlockRAM	2.1 Mb	4.9 Mb
DSP slices	80	220

Table 4-9: Product features of the TBS-5520 SE multi-standard TV tuner USB box [64]

Compatible standards	DVB over satellite (DVB-S, S2, S2X), cable (DVB-C, C2) and terrestrial (DVB-T, T2)
DVB-S2 symbol rate	1 to 45 Msps
FEC, nominal code rate	QPSK: 1/2, 3/5, 2/3, 3/4, 4/5, 5/6, 8/9, 9/10 8PSK: 3/5, 2/3, 3/4, 5/6, 8/9, 9/10 16APSK: 2/3, 3/4, 4/5, 5/6, 8/9, 9/10 32APSK: 3/4, 4/5, 5/6, 8/9, 9/10
Interfaces	USB for PC (32 and 64-bit operating systems) and power Satellite TV antenna input Input for cable-/terrestrial receiving
TV features	Manual and scheduled recording
Cost	200€
Dimensions	8.8 x 6.3 x 2.2 cm

In order to demodulate and decode the DVB-S2 transmitted signals, a TBS-5520 SE multi-standard TV tuner USB box *[64]* was used. The main features of this device are presented in Table *4-9*. It is typically used to receive, to display and/or record TV signals on a PC. Since the TV satellites are geostationary satellites, the Doppler effect is negligible for this kind of application. However, the Doppler effect cannot be neglected for the ROMEO mission as discussed in 3.5. Consequently, the test with the TBS-5520 SE emphasized to verify the functionality of the DVB-S2 IP core excluding the Doppler effect. The feature to cope with the Doppler effect has to be provided by a modem that will be described in more detail with the ground segment in 5.3.3.

The DVB-S2 firmware is loaded as a bitstream file from the PC to the FPGA from the PlutoSDR. The symbol rate was set to 20 Msps and the RF output frequency to 1450 MHz as required by the TBS-5520 SE. With the PC, the following settings were sent via the USB interface: MODCOD, pilot insertion, roll-off, and FEC frame length as described in 2.4.1.

Table 4-10 gives an overview of the parameter values used for the DVB-S2 IP core evaluation. The TBS-5520 SE detects the DVB-S2 configuration when providing the parameter values, thus it does not feature the ACM mode. Figure *4-8* shows the evaluation using MODCOD 28 with the test setup of Figure 4-7. The search parameters are set according to the TBS-5520 SE datasheet to emulate the reception of a TV satellite, thus the frequency is 11200 MHz. However, this has none effect on the measurement since the frequency parameter for the test setup was set to 1.45 GHz. The SNR of 22.5 dB is less than expected for an EVM of 2% of the PlutoSDR as listed in *Table 4-7* . This can be seen on the constellation points spreading in Figure *4-8*. Consequently, it is expected that the EVM is less than the one specified in *Table 4-7* since it was also observed in the other MODCOD configurations. This could be due to a higher quantization noise originating from a lower ENOB from the DAC than written in the datasheet. Despite the lower EVM, it can be seen that the IPrium DVB-S2 IP core works as expected and according to the datasheet since the TBS-5520 SE was able to demodulate and decode the DVB-S2 signal and to detect the correct configuration that was set. Consequently, an EVM measurement was not performed since the PlutoSDR is also not the target device.

Table 4-10: Overview of parameter values used for the DVB-S2 IP Core evaluation

Test parameter	**Value**
Symbol rate	20 Msps
RF output frequency	1450 MHz
MODCOD	1 – 28, according to Appendix A
Pilot symbol insertion	Yes
Roll-off	0.2 and 0.35*
FEC frame length	Normal and short

*the 0.35 roll-off was also evaluated to test the commanding of this register. Note that a roll-off of 0.35 will not be used for the ROMEO mission

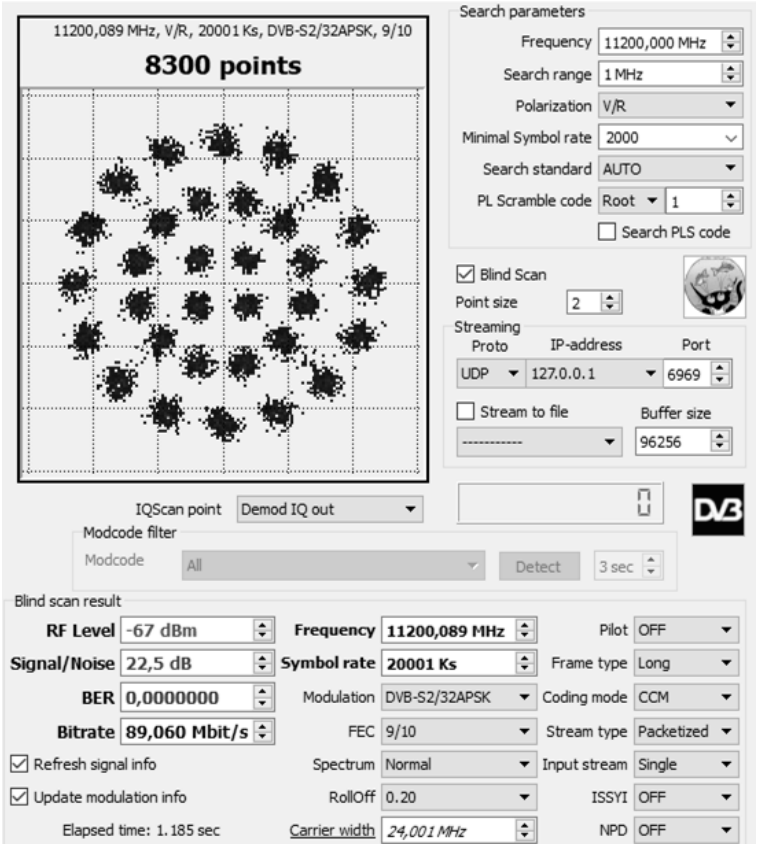

*Figure 4-8: Results of the DVB-S2 IP core evaluation for MODCOD 28 (refer to A.*DVB-S2*) according to the test setup in Figure 4-7. The roll-off was set to 0.2*

4.4.4 Influence of the X-band analogue frontend

The use of adaptive signal processing allows to increase the data throughput compared to non-adaptive digital signal processing. However, the X-band analogue frontend, as shown in *Figure 4-1* has to be compatible with the XTra-Pro and should not distort the signal and thus degrade the EVM in order not to impair reception on ground. Main issues are the selected DAC, the PA module, the antenna system and also the analogue frontend printed circuit board (PCB).

The digital to analogue conversion performance is determined by the quantization noise introduced. This can reduce the E_b/N_0 at the ground receiver if the ENOB is not sufficient. Consequently, a DAC with a high resolution and ENOB has to be chosen.

The PA module can introduce products due to its nonlinearity, which depends on the chosen backoff. The achieved gain depends on the input power and the required output power. Furthermore, the power consumption depends on the output power level, the OBO and the power efficiency. The thermal aspect is also relevant which depends on the operating temperature, the dissipation and the heat sinking, i.e. cooling mechanisms used.

The antenna system can further lead to loss due to impedance mismatching or cross polarization if not designed correctly. Typically, parabolic or horn antennas are used to achieve a high gain in satellites. However, due to volume constraints, neither horn nor reflector antennas can be used on the ROMEO mission. The inner structure of ROMEO is very limited due to the high volume and mass of the water-propulsion system. Thus, the inner structure is not available for a horn antenna. Also, the outer structure does not allow an easy integration of a parabolic antenna without decreasing the launch opportunities due to higher volume of the overall satellite.

The PCB design has to consider the vacuum, temperature and radiation effects. Hence, materials and components have to be used to are compatible with the space environment. Highly-integrated components permit to save on mass, volume and even power resources. Yet, these components are often recently made available on the market where little or none radiation data is available since they are not specifically tested for space use. Furthermore, it is difficult to test all failure cases due to the complexity of the component itself. In addition, the redundancy concept in hard- and software, latch-up protection and power distribution are key drivers. All these parameters have to be traded off to find the optimum components for the analogue frontend.

Further, the main components of the X-band analogue frontend should fulfil the RF level as listed in *Table 3-6*.

Another important factor for the component selection is radiation mitigation. The compromise between radiation protection and software complexity and resource increase due to radiation mitigation techniques like triple modular redundancy and scrubbing for the implementation of the digital signal processing algorithms is analyzed in 5.1. Other aspects, which are not implemented in this work, are: enabling system resets through a telecommand, radiation shielding, hardware redundancy, using over-current protections against latch-up, watchdog implementation, health-monitoring using relevant telemetry of the components and ECCs to correct the detected bit errors.

4.5 Detailed analogue frontend architecture

This section describes in detail the selection for the different components of the analogue frontend architecture and explains in detail the selected option.

4.5.1 DAC

As can be seen from the requirements listed in *Table 4-1*, the signal bandwidth is up to 50 MHz. This requires either two DACs or a two-channel-DAC with a sampling rate of at least 100 Msps, according to the bandpass sampling theorem described in 2.1. However, a two-channel DAC minimizes the synchronization problems due to delays in the two incoming data streams and is thus used for this transmitter. However, a higher sampling rate is advantageous since it allows digital oversampling, which reduces the requirements on the following anti-aliasing (bandpass) filter. Comparing DACs that provide an LVDS interface, a sampling rate of at least 100 Msps, gain and phase adjustment for sideband suppression reduced the component selection to AD9122 [65], AD9142 [66], AD9146 [67], and AD9783 [68] from Analog Devices. However, the AD9142 is not recommended for new designs by the manufacturer. Comparing the power consumption (<2.5 W, as specified in *Table 4-6*), phase offset and gain adjustment, availability, obsolescence risk and cost, the AD9122 was selected for the ROMEO transmitter. *Table 4-11* shows the DAC parameters of the considered DACs for the selection process.

Table 4-11: Parameters of the considered DACs

DAC	Resolution [bits]	Max. sampling rate [Msps]	Power consumption [W]	Gain and offset compensation	Cost [€]
AD9122	16	1230	1.5 @1.2 Gsps 0.8 @500 Msps	Yes	50
AD9142*	16	1600	2 @1.6 Gsps 1.7 @1.25 Gsps	Yes	50
AD9146**	16	1230	1.2 @1 Gsps 0.8 @500 Msps	Yes	40
AD9783	16	500	0.5 @500 Msps	Yes	30
EV12DS460	12	7000	3 @5 Gsps	Not mentioned	5000

*not recommended for newer designs, **only available when ordering 250 parts

4.5.2 Upconverter

A market survey of components that fulfil the requirements of *Table 4-1* led to the Analog Device's HMC8191 [69], HMC1056 [70] and ADRF6780 [71] upconverters. The parameters of the considered upconverters are shown in *Table 4-12*. The first two ones are passive components and thus require sufficient signal power (ca. 10 dBm) at the local oscillator input and attenuate the signal by ca. 7 dB during the frequency conversion. Moreover, the baseband inputs are not differential which would require that the differential outputs of the DAC must be converted into a single-ended signal with an active circuit. The ADRF6780 is an active component that has an integrated LO with a buffer amplifier and differential baseband inputs. The output is also differential, which necessitates the use of a balun. A drawback of the ADRF6780 is the power consumption of ca. 2.5 W, whereby the power consumption of the amplifiers with the passive solutions must also be considered. Yet, the power consumption is less than the expected 3 W, as specified in the preliminary power budget in *Table 4-6* and fulfils the RF level budget as listed in *Table 3-6*.

The ADRF6780 was selected due to its high level of integration that allows a more compact design compared to the passive upconverters. For converting the differential signal at the output of the ADRF6780 into a single-ended signal, the integrated LTCC balun NCR2-123+ from Mini-Circuits [72] was chosen, which is characterized by its compact design, low price and minimum phase imbalance at 10.475 GHz.

Table 4-12: Parameters of the considered upconverters

Upconverter	Active / Passive	Frequency range [GHz]	Conversion loss [dB]	Power consumption [W]	Cost [€]
HMC8191	Passive	6 - 26.5	9 – 11.5	0.7	100
HMC1056	Passive	8 - 12	8 - 11	0.8	30
ADRF6780	Active	5.9 - 23	5 - 7	2.5	90

The ADRF6780 upconverter is a key component since it has a significant influence on the RF characteristics like signal power level and EVM, among others, of the transmitter. Thus, in order to verify the performance of the component before developing, manufacturing and assembling a PCB, the evaluation board of the ADRF6780 [73] was procured and evaluated. *Figure 4-9* shows the test setup consisting of an Arbitrary Waveform Generator (AWG), the ADRF6780 evaluation board, and a spectrum analyzer to evaluate the upconverter's output spectrum. With this test setup the sideband and carrier suppression as well as the intermodulation distortion can be measured. The suppression of the unwanted sideband and on the carrier power level is evaluated with a sideband and carrier suppression test. The intermodulation distortion consists of multiples of the applied input frequency and mixing products of these that fall into the used bandwidth. These harmonics are tested with a single-tone test and a two-tone signal test.

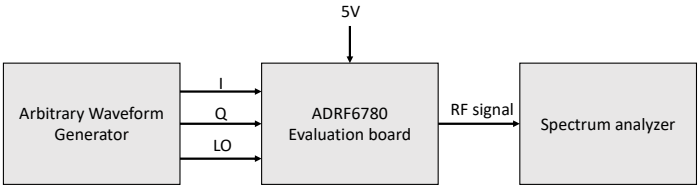

Figure 4-9: Test setup for the evaluation of the ADRF6780: arbitrary waveform generator, ADRF6780 evaluation board and spectrum analyzer. All the interfaces consist of 50 Ω coaxial cables

The purpose of the first test was to determine the sideband and carrier suppression of the ADRF6780. For this, an LO signal at 10.5 GHz and a single-tone baseband signal of 20 MHz was generated with the AWG and fed into the ADRF6780 evaluation board. *Figure 4-10* shows the spectrum at the output of the upconverter before and after tuning of amplitude, phase, and I/Q-offset. A difference of more than 50 dBc to the interference signals could be achieved.

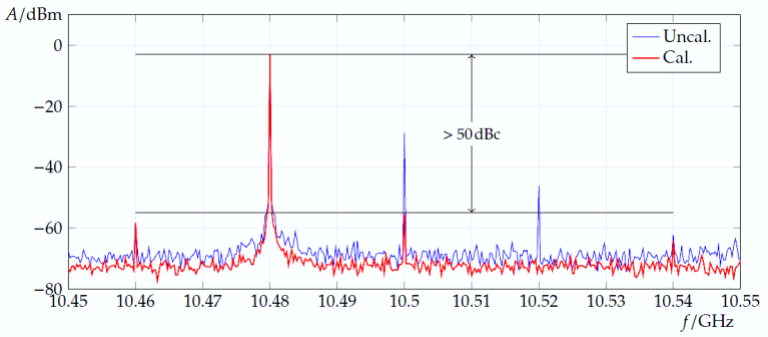

Figure 4-10: Spectrum at the output of the ADRF6780 with a single-tone signal test. The blue line represents the measurement before and the red line the measurement after phase, amplitude and I/Q-offset adjustment

To evaluate the linearity of the upconverter on the basis of intermodulation products, a two-tone signal with two tones at a distance of 1 MHz was generated using the AWG. The measured spectrum is shown in *Figure 4-11*. It can be seen that the interference signals are further than 50 dBc below from the useful signal.

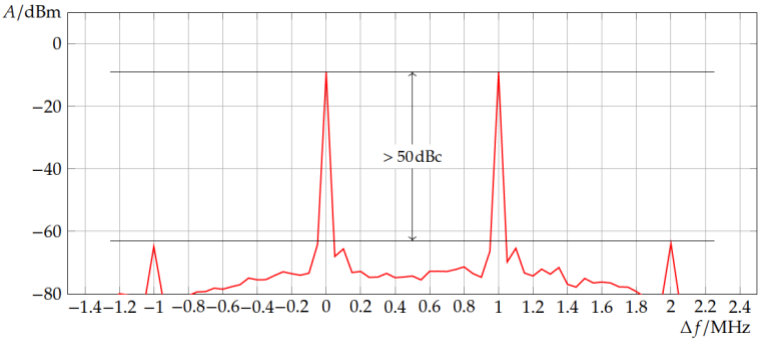

Figure 4-11: Spectrum at the output of the ADRF6780 with a two-tone signal test

Furthermore, the EVM was measured using a QPSK signal generated by the AWG to assess the modulation signal quality. The measured EVM is 5%. The comparatively poor EVM is due to the fact that the AWG has a resolution of 8 bits and generates quantization noise. It is expected that the EVM value will be lower due to the higher resolution (16-bit) and lower bandwidth of the DAC used in the actual transmitter.

With the presented measurements it was shown that the ADRF6780 is suitable for the intended application.

4.5.3 Local oscillator and clock

Instead of generating the required frequency directly, it can also be generated from a low-frequency signal by frequency multiplication. This low-frequency signal in turn can be generated with a PLL. To double the frequency, a signal is specifically distorted in a non-linear manner which results in harmonics. With a suitable design and filtering, the fundamental frequency and unwanted harmonics can be suppressed. Nevertheless, after the frequency multiplication, unwanted harmonic frequencies may be present, which have to be removed by bandpass filters either before or after the mixer. When considering PLLs, a distinction can be made between ICs in which the Voltage Controlled Oscillator (VCO), phase detector and divider are integrated and those that require an external VCO. External VCOs can be tuned by an external voltage, which makes the use of switching regulators necessary to generate the tuning voltage. However, when an X-band VCO, a phase detector and a divider are integrated into an IC, an external VCO with a high tuning voltage is not needed. Such PLLs have a large number of narrowband VCOs, from which the one suitable for the desired frequency is automatically selected. The fully integrated PLL LMX2594 [74] of Texas Instruments was selected since it can generate the required output frequency directly, has two differential outputs

and only requires a single supply voltage of 3.3 V while having a power consumption of less than 2 W (which fulfils the requirement of the power budget in *Table 4-6*).

The PLL and the DAC both require a reference clock of 100 MHz with LVDS level. A crystal oscillator of the type SG5032VAN [75] from Epson is used to generate this reference clock. The clock is distributed by a 1:4 bus of type Si53306 [76].

4.5.4 PA module

The PA module of the transmitter consumes most of the power of the transmitter, produces large amounts of dissipated heat and has a nonlinear characteristic which is prone to distort the useful signal. Thus, in this section, a concept for the PA module of the ROMEO mission is defined and simulated. This will ensure a baseline for the further development of the PA module that is not the scope of this thesis.

The amplifier's input (P_{in}) to output (P_{out}) characteristics have a significant impact on the satellite link. The maximum of the curve shown in *Figure 4-12* is the saturation point, the linear part of the curve is the small signal region, and the nonlinear part the compression region. The input backoff (IBO) is defined as the power amplifier's input below the value required for saturation, and the output backoff (OBO) refers to the corresponding reduction in the power amplifier's output, both values are in dB. The output versus input backoff diagram is known as AM/AM conversion, where the gain is normalized to 0 dB at saturation. In addition to the nonlinearity, a power amplifier can rotate the phase of the input signal as a function of the input level. This is known as AM/PM conversion. Furthermore, if mixing products are excited, intermodulation occurs. Thus, it is important to characterize the intermodulation distortion ratio (C/IM) that is the ratio of the signal power level at the fundamental frequency to one of the lower peaks. The intermodulation product that usually has the highest level is the third order product (C/IM3). It is important

to characterize the C/IM3 to avoid spurious signals in the channel bandwidth. However, mixing products outside the channel bandwidth can be suppressed by subsequent filtering. Also, a linearizer is often used before the driver amplifier which compensates part of the AM/AM and AM/PM distortion and thus allows a more linear operation of the whole PA module.

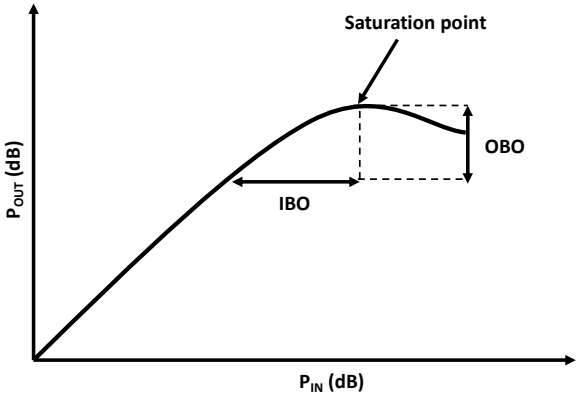

Figure 4-12: Power output P_{out} vs power input P_{in} of a power amplifier

In space applications, two amplifier technologies are typically used: Travelling Wave Tube Amplifiers (TWTAs) and Solid State Power Amplifiers (SSPAs). The preferred option when high power levels are needed is using TWTAs since they provide higher output power levels for a given frequency compared to SSPAs, but they are larger, heavier and require higher power supplies compared to SSPAs. Consequently, SSPAs are the preferred option for lower power application where they are also more economic. Since the resources on ROMEO are very limited and the PA module does not require a high output level in the order of 100 W, TWTAs are not an option for the ROMEO mission. Consequently, an SSPA will be used. SSPAs can be further distinguished by the semiconductor technology used: Gallium Nitride (GaN) and Gallium Arsenide (GaAs) amplifier. GaN amplifiers operate at higher voltages (24-

50V) than GaAs amplifiers (5-20V). The higher operating voltage results in a better power added efficiency (PAE) of the amplifier. Furthermore, GaN amplifiers can operate at higher temperatures than GaAs amplifiers without degradation but these are more expensive than GaAs SSPAs due to the materials and production process [77]. Yet, due to the higher power density, better high frequency performance, higher efficiency and increased reliability, GaN SSPAs are chosen for the PA module of the transmitter of the ROMEO mission.

The parameters AM/AM conversion, AM/PM conversion, and backoff define the operation point of the PA module, which has to fulfil the requirements of the ROMEO mission listed in *Table 4-1*. A minimum required EIRP of 16.4 dBW for the transmitter was calculated in 3.3.2. Due to the restricted resources, and thus the power budget on ROMEO, the power consumption of the PA module should be as low as possible while providing a sufficient RF output power to close the link budget. The signal power level at the output of the upconverter is ca. 0 dBm, which means that an overall gain of ca. 33 dB for the PA module is required, as shown in the RF level budget in *Table 3-6*.

The following has to be considered when choosing the PA module components:

- The output power level has a significant effect on the efficiency. When the amplifier is driven in compression, the maximum efficiency is achieved at maximum output power. At reduced output power, the efficiency decreases
- The transmitted signal is based on the DVB-S2 standard where the envelope of the modulated signal continuously changes due to the different modulation schemes used. The amplifier must be able to cover the maximum power peaks in order to mitigate the distortion of the signal. Thus, the amplifier must be operated with backoff, which

reduces the maximum achievable output power level

Taken these into consideration, the following assumptions were made for the PA module and will be the baseline for future work on it:

- The PA module consists of a pre-amplifier that pre-distorts the signal, and a driver amplifier. The pre-amplifier is a variable gain amplifier that adapts the gain according to the used MODCOD
- The PA will be operated below nominal power in order to improve the EVM and MER. A maximum backoff of 2 dB is assumed and was already considered in the link budget calculations of 3.3.2
- It is assumed that the thermal design of the ROMEO satellite achieves a stable temperature were the PAE is constant
- A power supply board for the PA module is considered as shown in *Figure 4-1* due to the voltage supply requirements of the GaN SSPAs that cannot be provided by the power control and distribution unit of the satellite
- It is assumed that the impedance matching is not optimal and an output return loss of 10 dB is considered due to the parameters of the amplifiers listed in *Table 4-13*
- An isolator will be located after the driver amplifier's output to improve RF matching
- To account for any further loss, an implementation loss of 1 dB and degradation loss of 1 dB was considered in the link budget calculations as listed in *Table 3-6*

The different parameters were compared to commercially available amplifier solutions as well as the potential to survive the space environment. A variable gain pre-amplifier, like for example the NBB-300, can be used to amplify the signal before

the driver amplifier. The NBB-300 achieves a small signal gain of typical 9.5 dB and thus can amplify the 0 dBm signal from the upconverter to 9.5 dBm. The power consumption is defined with 300 mW in the datasheet. Yet, for the expected power consumption 1 W is considered to include an additional reduction of PAE due to higher operation temperature, for example. *Table 4-13* shows possible driver amplifiers of Qorvo. Qorvo is a semiconductor company that develops GaAs and GaN amplifiers that are used in different satellite missions and are thus flight-proven. However, this information is not valid for every amplifier. In general, the performance of the amplifier regarding output power and PAE is higher the lower the environmental temperature, the higher the input power (P_{IN}), the higher the drain voltage as well as drain and gate current. In terms of PAE, the QPA2610 presents the best value with a PAE greater than 47% at an environmental temperature of 25ºC. If the temperature is -40ºC, the PAE would be near 50% and if the temperature is +85ºC, the PAE decreases down to 26%. Regarding the output power, the TGA2760SM, the QPA2610 and the TGA3042SM achieve similar values. Since the output power decreases by approximately 0.21dB/ºC with the QPA2610 a heat sink in the PA module must be implemented in order to minimize the operating temperature as far as possible. The expected power consumption of the QPA2610 is 8W. Thus, the total expected power consumption for the PA module is 9 W which fulfils the power budget defined in *Table 4-6*.

Simulations were performed in Simulink to analyze the influence of the different PA parameters and the influence of the pre-amplifier. The simulation model and its results can be found in Appendix G. Since the transmitter is adaptive, the different modulation schemes were tested to see the influence of the PA module for the different configurations. Furthermore, the use of a digital pre-distortion (DPD) algorithm was analyzed. A DPD algorithm ideally distorts the signal to counter the nonlinear effects of the power amplifier.

Thus, the baseline for the PA module is the NBB-300 as variable gain pre-amplifier and the QPA2610 as driver amplifier. Since the simulations showed that EVM increases the higher the modulation scheme, the use of a DPD algorithm should be further investigated. The DPD algorithm could, for example, be only used for higher modulation orders (16APSK and 32APSK) and not for the more robust ones (QPSK and 8PSK) in order to save power resources and to minimize the complexity when reliability of the link is needed. In order to save on power resources, it should be further analyzed if the DPD algorithm is needed for all the different configurations or if it is especially suitable for higher modulation orders only. For the use of a DPD algorithm with a feedback loop, a downconverter is needed which increases the number of components in the analogue frontend. However, a DPD algorithm without a feedback loop is also possible and less complex. Also, more power resources are needed for the DPD algorithm implementation on the SoC. However, if the DPD algorithm permits to transmit more useful data, and since the transmitter will only be switched on during ground station overflights, this could be a compromise.

Table 4-13: Parameters of the considered power amplifiers. The term typical gain corresponds to the small signal gain, e.g. to the gain in the linear region

Amplifier module	**Frequency range**	**Typical gain**	**PAE at P_{IN}=dBm**	**P_{OUT} with P_{IN}=0dBm**
TGA2760SM	10 – 11.7 GHz	33 dB	36% @+25ºC	33 dBm
QPA2610	8.5 – 10-5 GHz	38.5 dB	>47% @+25ºC	33.7 dBm
TGA3042SM	7 – 10.5 GHz	32 dB	25% @+25ºC	33 dBm
TGA2598SM	6 – 12 GHz	33 dBm	>25% over freq. range	26 dBm
TGA2704SM	9 – 11 GHz	21 dB	10%	23 dBm

4.5.5 Patch array antenna

The antenna has to be compatible to the IRS ground stations from *Table 3-2* and fulfil the parameters listed in *Table 4-1*. The different antenna types that were considered for the development are the following:

- Parabolic reflector antenna: antenna type that uses a parabolic reflector to direct the radio wave signal with a horn-based feed system
- Horn antenna: antenna type that uses a horn-shaped waveguide to direct radio wave signals in a beam
- Patch(-array) or microstrip antenna: antenna type that can be printed directly onto a circuit board. If several patch/microstrip antennas are connected it is called a patch array antenna

In order to select a suitable antenna type for the ROMEO mission, a trade-off was performed comparing different parameters like development effort, maximum achievable gain, polarization, feed concepts and costs. The trade-off is presented in *Table 4-14*. The gain figures were calculated for a 10x10 cm area located on the ROMEO structure. The limited mass and volume resources on ROMEO make the use of a parabolic reflector antenna or a horn antenna difficult. The parabolic reflector antenna further requires a feed and a circular polarizer. The gain of a parabolic reflector antenna and a symmetrical horn antenna can be calculated with the following equation:

$$\text{Gain} = 10\ log_{10}\text{k}\left(\frac{\pi D}{\lambda}\right)^2 \text{[dB]} \qquad \textit{Eq. 4-1}$$

where 0<k<1 is the antenna efficiency, D the parabolic reflector diameter and λ the wavelength. If an efficiency of 0.7 is assumed, a 0.1 m diameter parabolic reflector achieves a gain of 19.2 dBi. Yet, the parabolic structure exceeds the ROMEO dimensions and would thus difficult the selection of a launch opportunity.

A horn antenna has to be positioned inside or outside the ROMEO structure. Ideally, it achieves the same gain of 19.2 dB as the parabolic reflector antenna. However, since the inside structure of ROMEO is very limited it is not suitable to select a horn antenna for the ROMEO mission.

Table 4-14: Trade-off for different antenna types

Parameter	Antenna type		
	Parabolic reflector antenna	**Horn antenna**	**Patch (array) antenna**
Volume	High, antenna has to be mounted on external panels of the satellite	High, located at the inside or outside satellite structure	Low, low-profile structure on the outside satellite structure
Development effort	Well-known methods	Well-known methods	Well-known methods
Max. achievable gain	Ca. 19.2 dBi	Ca. 19.2 dBi	Depends on the number of patches, see results of Eq. *4-3* for gain values. 4x4 patch array can achieve up to ca. 17.4 dBi
Polarisation	Depending on polarisation concept, additional volume needed		
Feed concepts	Depending on feed concept		
Cost	High	Low	Low

A possible alternative is to use a patch antenna. Such antennas are very compact and inexpensive. In order to be able to use patch antennas for the adaptive transmitter, the gain must be minimum 16 dBi, according to *Table 4-1*. This can be achieved if several patches are placed on the same substrate (patch array). If a suitable feed and polarizer concept is used to generate a circular polarization it is also compatible to the IRS ground stations.

A patch antenna is defined by its patch length, patch width, input impedance, gain and radiation pattern. The patch length can be calculated with the following equation [78]:

$$\mathrm{L} = \frac{c_0}{2f_r\sqrt{\epsilon_{eff}}} \qquad \textit{Eq. 4-2}$$

where c_0 is the velocity of the electromagnetic wave in free space, f_r the resonant frequency, and ϵ_{eff} is the effective dielectric constant of the substrate. For further details on patch antenna basics refer to Appendix E.

Various patch array configurations were considered and compared with the requirements from *Table 4-1*. The maximum area permitted for the patch array antenna was 10x10cm area on the outer structure of ROMEO as seen in the CAD in *Figure 3-2*. The absolute achievable gain of a patch array can be described by [78]:

$$G_{abs} = 4\pi \cdot \frac{Md_xNd_y}{\lambda^2} \qquad \textit{Eq. 4-3}$$

where M and N are the number of patches in x- and y-direction, dx and dy the distances between the patches in x- and y-direction and λ is the wavelength. It should be mentioned that Eq. 4-3 is similar to Eq. 4-1 through comparing the equivalent area, and thus, the patch array antenna´s physical

characteristics, such as the number of patches, their size, shape, and spacing, as well as the antenna´s directivity and radiation efficiency to the hypothetical area of an ideal isotropic antenna. The only difference is that Eq 4-3 defines the case of an efficiency k = 1, which in practice is not achievable. To achieve a minimum gain of 16 dBi with a 10.475 GHz centre frequency, a 4x4 array (M = 4, N = 4) is needed. This was calculated with a distance in x- and y-direction between the patches of dx = dy = 0.5λ = 14.3mm. With four patches M = N = 2, the array gain G_{abs} is 11.35 dB and with a total of 9 patches, M = N = 3, the array gain G_{abs} is 14.7 dB, which does not meet the requirement of 16 dBi. With M = N = 4, a theoretical gain of G_{abs} = 17.37 dB could be achieved. Yet, the simulated gain is expected to be less since feeder loss or mismatch are not taken into account. Considering an efficiency of k = 0.73, a gain of 16 dBi can be achieved, which meets the requirement. With the correct patch array antenna configuration it is also considered that a sufficient cross polarization discrimination (XPD) can be met.

With the use of the simulation tool Altair Feko (refer to Appendix B for more information), different patch array antennas and their polarizer and feed concepts were simulated to prove the feasibility of using a patch array antenna for the ROMEO mission. The detailed simulations can be found in Appendix E. Overall, the simulations showed that it is feasible to use a patch array antenna for the ROMEO mission. The trade-off and the simulation of different patch array antenna configurations were analysed in a master thesis [79].

5 Testing and verification

To verify the analysis and design assumptions made in chapter 3 and 4, the different parts of the adaptive transmitter for ROMEO were tested and verified, according to the verification methods listed in *Table 4-1*. The implementation of the digital signal processing is evaluated in 5.1, the chosen components for the analog frontend are evaluated in a prototype in 5.2 and the breadboard chain test from the XTra-Pro up to the upconverter, including the verification of the ACM mode, is explained in 5.3. A discussion about the different tests and evaluations is given in 5.4.

5.1 Evaluation digital signal processing

5.1.1 Implementation

All DSP algorithms were implemented on the ZedBoard development board, which includes the target Zynq-7020 SoC. *Table 5-1* shows the main characteristics of the ZedBoard. The Advanced eXtensible Interface 4 (AXI4) bus system allows the communication between the different components on the SoC. The AXI supports bidirectional data transmission and its protocol defines five channels: two for Read transactions (read address, read data) and three for Write transactions (write address, write data, write response). The data flow is controlled by a handshake mechanism, and the data exchange takes place using a master-slave architecture. This is accomplished by using the control signals VALID and READY. The VALID signal indicates that data is ready for transmission. The READY signal indicates that data can be received and processed by the component in the SoC receiving the data. There are three types of AXI4-interfaces: AXI4 (for high-performance memory-mapped requirements), AXI4-Lite (for simple, low-throughput memory-mapped communication, for example, to and from control and status registers) and AXI4-Stream (for high-speed streaming data).

Table 5-1: Main characteristics of the Zedboard [80]

SoC	Zynq-7000 SoC XCZ7020-CLG484-1
Memory	512 MB DDR3 256 Mb Quad-SPI Flash 4 GB SD card
Programming interface	USB-Joint Test Action Group (JTAG)
Interfaces	10/100/1000 Ethernet USB OTG 2.0 USB-UART PS and PL I/O expansion Multiple displays (1080p HDMI, 8-bit VGA, 128x32 OLED)
Cost	500€

The interfaces between the programmable logic and the processing system, and between the Zedboard with the PC are shown in Figure 5-1 and were implemented during a bachelor thesis [81]. A USB interface is used to configure the SoC from a PC and an Ethernet connection is used to transmit the data for this test setup. The ARM processor of the SoC's processing system is used to control and configure the DVB-S2 modulator IP core. The different software tools used in this implementation are described in *Table 5-2*.

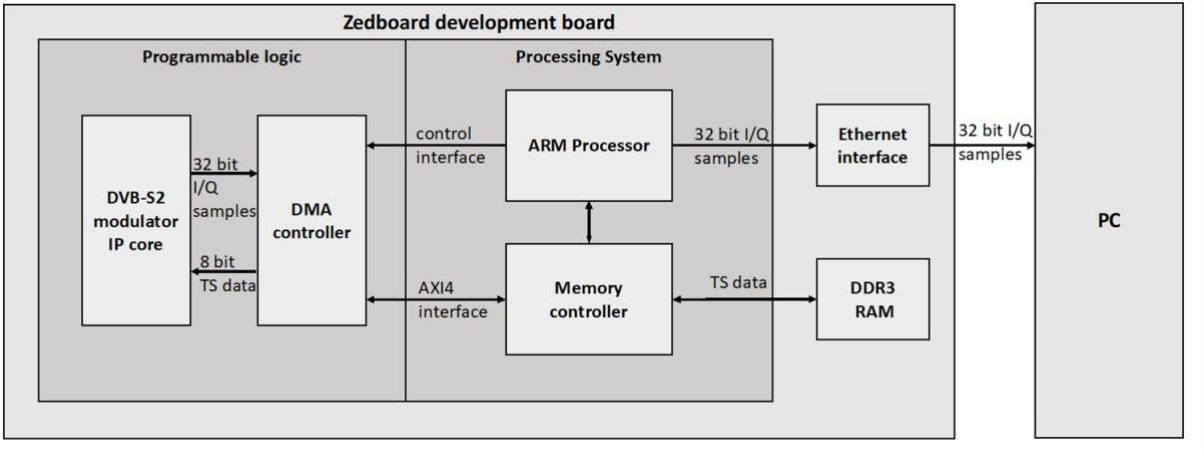

Figure 5-1: *Overview of the required interfaces between the programmable logic and the processing system of the Zedboard to implement the DVB-S2 IP core and between the Zedboard and the PC through the Ethernet interface*

The data to be processed by the DVB-S2 modulator is stored as a TS video file on the SD card of the Zedboard. The TS video file is read from the FAT32 file system of the SD card and stored in the DDR3 RAM with the XilFFS library. The data from the DDR3 RAM is accessed with a direct memory access (DMA) controller. A DMA function block is instantiated in the programmable logic, which is connected to the processor, the DVB-S2 modulator and the DDR3 RAM memory controller. Transmission to or from the DDR3 RAM are executed through the DMA controller, specifying the memory address and the number of bytes to be transferred. The maximum number of bytes than can be transferred in a single transmission is 8 MB in the configuration used. The processor periodically queries the transfer status through the DMA controller. The AXI-based DMA distinguishes two channels: memory-mapped to stream (MM2S) that transports data from the memory to the FPGA and stream to memory-mapped (S2MM) that transports data to the memory.

After the data is processed by the DVB-S2 modulator, the data output is connected via the AXI S2MM interface of the DMA controller. The DMA controller processes this data stream for an address-based transfer to the DDR3 RAM. The data flow is performed via the READY and VALID control signals. When a transfer is started, the DMA controller sets the READY signal and a certain number of bytes can be transferred to the DDR3 RAM if the VALID signal is set. The status of a transfer can be queried by the processor or signaled via interrupts. The data to be sent is provided via the AXI MM2S interface. For this purpose, the data from the DDR3 RAM is processed into an 8-bit wide data stream. Additionally, the input sync-word byte marker (0x47) signal is generated from the DVB-S2 modulator, which indicates the start of a packet. For this purpose, a VHDL module was written that detects the synchronization byte 0x47 in the data stream. Since this pattern can also occur in the user data of the packet, the detection is blocked for the length of a packet (188 bytes).

Table 5-2: Software tools used for the evaluation of the digital signal processing

Tool	Description and use
Vivado	Software suite from AMD Xilinx for synthesis and analysis of HDL designs with features for SoC development and high-level synthesis. Used for the implementation, simulation and test of the DVB-S2 modulator IP core
AMD Xilinx fat file system (XilFFS) library	Library from AMD Xilinx that provides a file system that supports FAT16 and FAT32 for selecting a File system with an SD or a RAM based File system
lwIP TCP/IP stack library	Library from AMD Xilinx that provides a TCP/IP stack to use with Ethernet interfaces for Zynq-boards
Python	Programming language used to set up the TCP/IP client on the PC
SDRangel	Open-source SDR and signal analyzer that collects I/Q samples from a hardware device. One or more channel Rx plugins can be used to demodulate, decode or analyze the received signal [82]. It is fully compatible to the DVB-S2 standard. To decode the data correctly, the received I/Q samples must be extended by a 32-byte header containing information such as sampling rate and center frequency
DVB-S2 IP core (IPrium)	IP used for the implementation of the DVB-S2 standard according to [3]
CCSDS PTME IP core	IP core distributed through the ESA IP core portfolio website [83] which is used for the implementation of the CCSDS standard according to [84]

The ARM processor configures the modulator with the selected parameters and manages the data input/output. *Table 5-3* summarizes the parameter values for the test setup. The address-based data transmission between the PS and the PL is enabled by an AXI4-Lite interface. The data to be transmitted to each address, as shown in *Figure 5-2*, is stored in registers and connected to the DVB-S2 modulator's control inputs. Each register has a word width of 32 bits, and can be addressed byte by byte. A C-code was written to program these registers, including functions for writing and reading the registers. This code is executed in the ARM processor, which in turn configures the DVB-S2 modulator settings. Due to the limited memory capacity of 512 MB of the DDR3 RAM, the stored data is transmitted through the Ethernet interface of the Zedboard to the PC. To this purpose, the AMD Xilinx lwIP TCP/IP stack library was implemented on the Zedboard to enable the data transmission to and from the PC through an Ethernet interface. TCP enables connection-oriented and reliable transmission, as loss of data can be automatically detected. A TCP server was set up on the PC using a Python script. The TCP server saves the incoming data after the connection with the client has been established. The S2MM transfer data is buffered and spread across multiple TCP packets. Double buffering was used to optimize the data throughput with DMA transfers and Ethernet transfers to the PC. Two buffers of the same size are used and accessed alternately for reading and writing. While the data of one buffer is being sent via TCP, the other buffer is simultaneously filled with new data from the DVB-S2 modulator via the DMA controller. When both transfers have been made, the processing of the buffers is exchanged. The newly recorded data are processed via the TCP stack and the data already sent are overwritten with new data from the S2MM transfer. The TCP stack allowed a maximum transmission speed of up to 500 Mbps which was sufficient to test the maximum data rate of 185 Mbps for MODCOD 28. Thus, this configuration fulfils the maximum data rate requirements for the ROMEO mission.

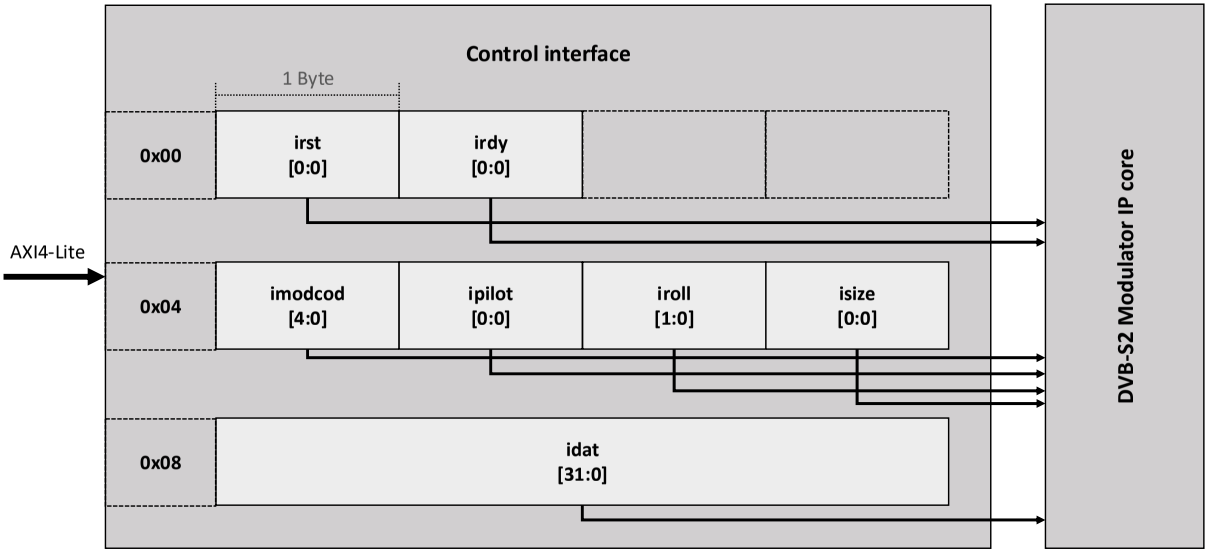

Figure 5-2: Control interface for the DVB-S2 modulator IP core

Table 5-3: Parameters set for the test setup, according to the analysis made in chapter 3 and the design of chapter 4

Parameter	**Value for the test setup**
System clock rate	83.1 MHz
MODCOD	1 to 28
Pilot symbols	On
Roll-off factor	0.2
Symbol rate	41.55 Msps
LDPC code frame size	Normal frame (64800 bits)
Input sync-word byte marker	0x47

In the next step, the recorded transmission signal is analyzed and verified against the transmitted data. This is done with the SDRangel tool on the PC. The data was successfully decoded by specifying the signal bandwidth, symbol rate and roll-off factor, according to the values in *Table 5-3*. The modulation scheme and the code rate are automatically determined for each frame from the PL header. To test the ACM mode of the DVB-S2 IP core, the ARM processor commanded a randomly selected MODCOD each second. The DVB-S2 IP core changed the MODCOD after each frame and the SDRangel tool on the PC could successfully select the correct MODCOD, decode the data and reproduce the TS video file on the PC.

To fulfil the requirement of IRS ground station compatibility (refer to *Table 4-1* for more details), the transmitter must implement the CCSDS standard in the physical and in the data link layer. For this purpose, the CCSDS PTME IP core from the ESA IP core portfolio is used. This IP core was implemented analog to the DVB-S2 IP core. The IP core is controlled and configured by the ARM processor of the SoC's processing system Since the IP core was not developed for the new SoC generations (the SoCs including version 7 or newer of FPGAs, like the Artix-7 or Kintex-7 that are included in the Zynq-SoCs) based on the AXI bus system, the IP core's control interface is incompatible with the SoC. Thus, an AXI4-Lite interface was

implemented to allow address-based data transmission between the PS and the PL.

5.1.2 Resource utilization

After implementing and testing the DVB-S2 modulator and the CCSDS PTME IP core, the resource utilization of the implemented configuration was analyzed. This is important since the resources on the SoC as well as the power resources on ROMEO are limited.

Figure 5-3 shows the resource utilization of the DVB-S2 modulator IP core on the SoC of the Zedboard for the used implementation. LUTRAM is the distributed RAM used for the LUT. IO are the input and output resources and BUFG represents the global buffer usage resource used on the FPGA. It can be seen that less than 20% of each resource of the FPGA of the SoC is used. This permits to implement redundancy in the design since sufficient resources are available to implement, for example, double or triple modular redundancy. Here, the IO resources would remain equal since no additional input and output resources would be used. The power resources and their distribution on the SoC of the DVB-S2 modulator IP core implementation are shown in *Figure 5-4*. Static power represents the power if the SoC is powered but the implementation is not running. Dynamic power is the power consumed if the SoC is in operation. The total on-chip power consumption, if the implementation is in operation, corresponds to the sum of the static and the dynamic power, which is 0.275 W. 61% corresponds to dynamic power and 39% to the static power.

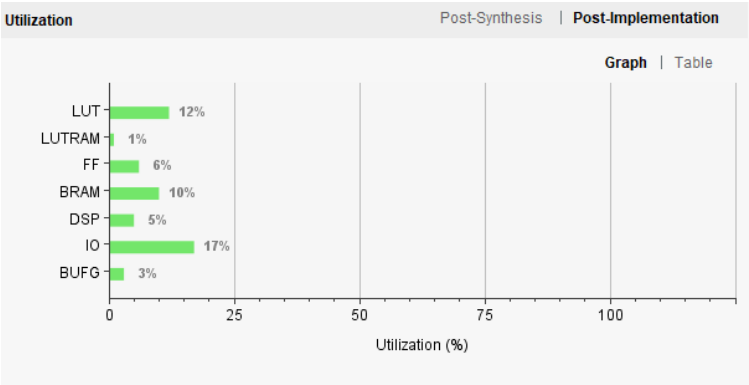

Figure 5-3: Resource utilization of the DVB-S2 modulator on the SoC after implementation. The implementation of the DVB-S2 modulator IP core as well as the resource utilization calculation was done with the Vivado tool from AMD Xilinx. BUFG is the global buffer of the Zedboard

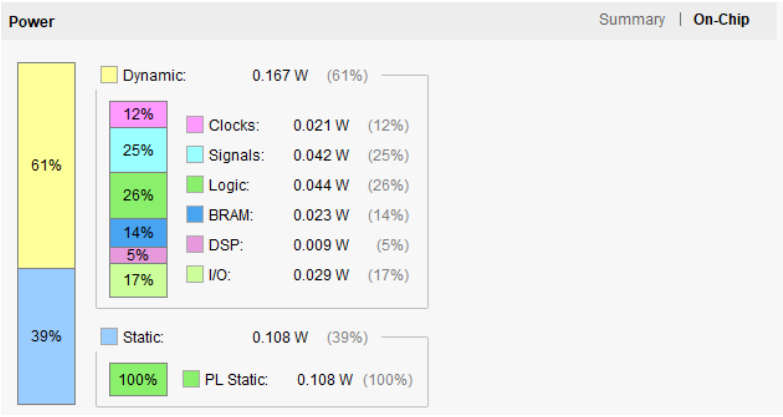

Figure 5-4: Power resources of the DVB-S2 modulator IP core implementation on the SoC of the Zedboard

Figure 5-5 shows the resource utilization and *Figure 5-6* the power consumption of the CCSDS PTME IP core. Because the CCSDS PTME IP core is also utilized for telemetry and telecommand processing, knowing the IP core's utilized resources as well as the predicted power consumption is critical. The static power consumption of the CCSDS PTME is very low, i.e. 0.149 W, compared to the 1.661 W dynamic power consumption. This means, that only during a ground station pass the CCSDS implementation will consume 1.809 W; nominally it consumes 0.149 W.

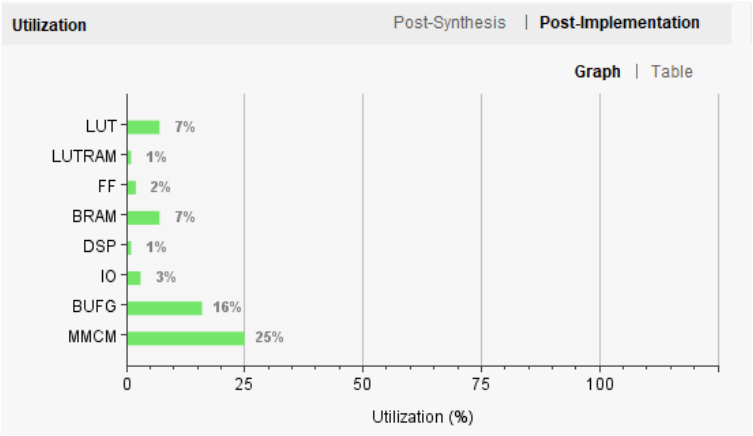

Figure 5-5: Resource utilization of the CCSDS PTME IP core on the SoC after implementation. The implementation as well as the resource utilization calculation was done with the Vivado tool from AMD Xilinx. BUFG is the global buffer and MMCM the mixed-mode clock manager

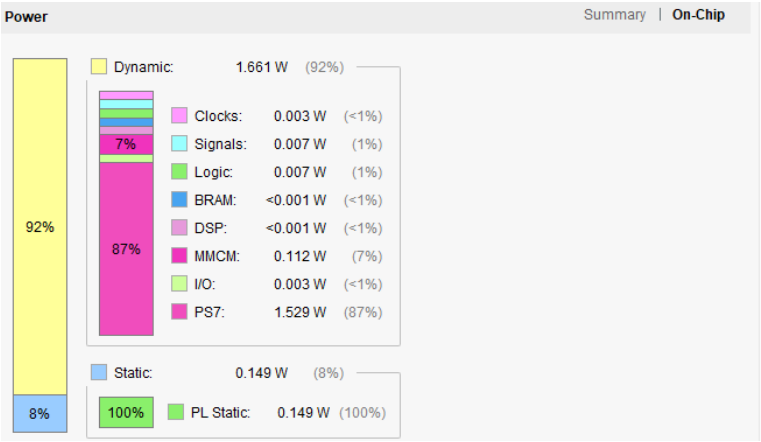

Figure 5-6: Power resources of the CCSDS PTME IP core implementation on the SoC of the Zedboard

The combined resource utilization of DVB-S2 and CCSDS PTME IP core implementation is 19% of the LUTs as shown in *Table 5-4*. In order to minimize the resource utilization, only the most important functionalities, i.e. the mission critical functions on ROMEO, should be triple modular redundant in order to save resources on the SoC and power consumption. Triple modular redundancy consists of implementing a function, in this case the CCSDS PTME IP core, three times. The result of the three implementations is processed by a majority-voter which produces a single output. If any of the three implementations fails, for example due to a SEE, the other two can correct and mask the fault. Since the CCSDS PTME IP core is used for the transmission of telemetry during a ground station pass, and the telemetry transmission is more critical than the payload data transmission, the CCSDS PTME IP core should be as reliable as possible and thus be implemented in a triple modular redundant configuration. Thus, the CCSDS PTME IP core implementation was triplicated to assure a triple modular redundancy while the DVB-S2 IP core is only implemented once

without redundancy. Furthermore, this leads to the minimum needed resource utilization on the SoC as well as the least power consumption compared to other possible combinations, as shown in *Table 5-4*.

Table 5-4: Resource utilization of the different IP core configurations

IP Core	**LUTs [%]**	**Total power consumption [W]**
DVB-S2	12	0.275
CCSDS PTME	7	1.809
CCSDS over DVB-S2	19	2.107
TMR CCSDS PTME	25	1.821
TMR CCSDS + DVB-S2	37	2.113

The evaluation of the digital signal processing implemented on the Zedboard showed that it is feasible to use the CCSDS and the DVB-S2 standard on the ROMEO adaptive transmitter. Furthermore, the implementation on the Zedboard showed that the ACM mode could be tested successfully by processing a TS video file and decoding it on a PC with the SDRangel tool. The resource utilization evaluated by Vivado shows that if triple modular redundancy is used on the CCSDS PTME IP core and no redundancy is applied on the DVB-S2 IP core, the LUTs needed are less than 40% and the total power consumption during a ground station pass would be 2.113 W. This value is slightly lower than the one specified for the SoC in *Table 4-6*.

5.2 Evaluation of the analogue frontend on a prototype

Since the analogue components have an effect on the signal quality of the Xtra-Pro, a prototype of the analogue frontend was built, analyzed and characterized to further assess the influence of the analogue frontend components.

After the analysis of the best suited transmitter architecture for the ROMEO mission in 4.2 and the component selection regarding DAC in 4.5.1, upconverter in 4.5.2 and LO and clock in 4.5.3, a prototype of the analogue frontend using these components was designed. The prototype consists of the X-band analogue frontend as shown in *Figure 4-2* without the PA module. The layout and the assembly of the prototype was done in the frame of a master thesis [85] and the characterization was performed in the laboratories of the Institute of Robust Power Semiconductor Systems of the University of Stuttgart. All circuit diagrams of the prototype can be found in Appendix F.

5.2.1 PCB circuit design

To make the commissioning and subsequent tests as simple as possible, the assembled board was powered by a single voltage source. This reduces the risk of damage caused by a reverse polarity of the voltage source. A 3 A diode is connected in anti-parallel to the input to protect the board against reverse polarity of the voltage source. The required voltage for each component of the analogue frontend board is listed in *Table 5-5*. To prevent the propagation of interference between circuit parts via supply voltages, each of these voltages is generated by a separate voltage regulator. To further limit interference, linear regulators are used whenever possible.

Table 5-5: Voltage requirements for the analogue frontend

Voltage	Component
1.8 V	1.8 V pins from FPGA DAC, digital part DAC PLL Upconverter
2.5 V	FPGA, LVDS interface
3.3 V	FPGA, USB interface DAC, analog part DAC, programming interface Upconverter LO-PLL, clock distribution
5 V	Upconverter

5.2.1.1 FPGA

To configure the components, an FPGA was selected in order to keep the complexity low (compared to using the SoC AMD Xilinx Zynq-7020). The MAX 10 Series FPGA from Intel [86] was used.

Table 5-6 shows the main characteristics of the selected MAX 10 FPGA and the used FPGA banks to interface with the other circuit components.

5.2.1.2 DAC

The LVDS interface on the AD9122 DAC [65] is used to load the data from the MAX10 FPGA. This interface can be operated with four different bit widths: 4, 8 or 16 bits. Due to the 16-bit resolution of each of the two channels, a complete 32-bit wide data word can be transmitted in 8, 4 or 2 clock cycles. Two additional signals, “FRAME”, and “DCI”, are used to synchronize the signals of the two channels. The 8-bit mode is chosen since the FPGA has 10 LVDS outputs. Since the LVDS outputs support a maximum data rate of 200 Mbps, a sampling rate of 200 Mbps

in the 8-bit mode = 50 Msps was used. The FRAME signal indicates to which portion of the 32-bit word the applied 8-bit word corresponds. The DAC samples the data inputs and the FRAME signal approximately 350 ps after each rising edge of the DCI. Therefore, it is necessary to design the board layout such that DCI is only applied after the data and FRAME signals. This is accomplished by a delay line as shown in *Figure 5-7*. Further length adjustments of the data lines can therefore be omitted. A length adjustment between the differential pairs was not necessary, since the propagation time differences of <5 ps are negligible for the rising times of approximately 300 ps.

The data is interpolated 8-fold in the DAC from a sampling rate of 50 Msps to 400 Msps. This fulfils the requirement of at least 100 Msps, as described in 4.5.1. In addition to the digital filters used for interpolation, the DAC includes filters for correcting the phase imbalance between both channels. Furthermore, voltage offset and gain can be adjusted for both channels to compensate for any imbalance between the I and Q channel. Therefore, no additional adjustment needed to be made in the FPGA, simplifying the logic design. The DAC is programmed with an SPI interface, which is connected to the MAX10 FPGA.

5.2.1.3 Upconverter

The analog complex baseband signal from the dual DAC is differentially connected to the input of the upconverter ADRF6780. The local oscillator signal input is DC blocked using capacitors. To program the registers of the ADRF6780, the pins of the SPI interface and the control lines are connected to the FPGA as listed in *Table 5-6*. The output amplitude can be varied since the ADRF6780 has an analog control input. This is controlled via an 8-bit DAC from Texas Instruments [87]. The RF output of the upconverter is connected to the output socket via a balun. The balun enables the transition of the unbalanced coaxial cable to the balanced feed point. An SMA “Edge Launch” socket [88] is used as the output. The size of the center pin is

sized in order to connect (by soldering) the jack to a coplanar waveguide with ground plane as shown in *Figure 5-8*. To improve its ground connection, vias are placed at the edge of the line.

Table 5-6: Main characteristics of the MAX10 Series FPGA and IO-banks

Logic elements	50K
Memory	1638 kb
User flash memory	5888 kb
PLL	4
General Purpose Input Output (GPIO)	500
LVDS	LVDS buffers supporting LVDS using differential buffers: 30 Emulated LVDS buffers supporting a pair of single-ended pins to emulate differential buffers: 241

IO-bank	Circuit component	Voltage
1A, 1B	JTAG, USB	3.3 V
2	Clock distribution	2.5 V
3	DAC LVDS	2.5 V
4	DAC LVDS	2.5 V
5	Upconverter	1.8 V
6	PLL, DAC	3.3 V
7	LEDs	3.3 V
8	DAC for output amplitude	3.3 V

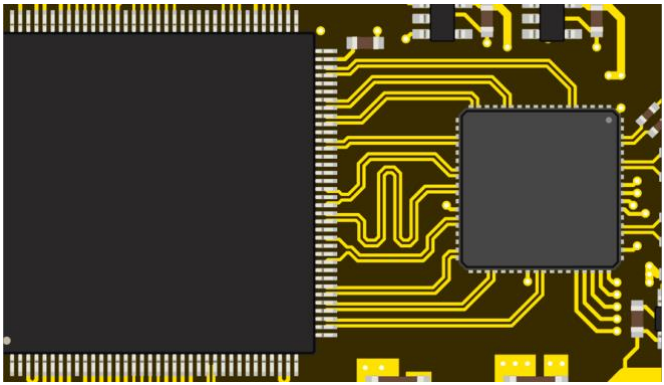

Figure 5-7: Layout (upper layer) of the connection of the DAC (right) to the FPGA (left). Taken from [85]

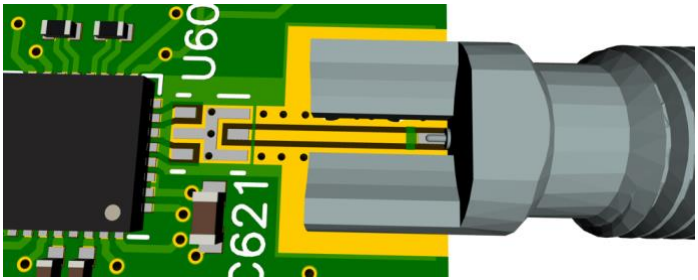

Figure 5-8: 3D assembled PCB with the upconverter (left), balun (outline not shown) and coaxial connector. Taken from [85]

5.2.1.4 Layout

Figure 5-9 shows the upper layer of the assembled board. The PCB's base material is FR408 and the layers are used as follows:

- Layer 1: signals, 50 Ω and 100 Ω differential lines
- Layer 2: ground plane
- Layer 3: signals, voltage supply
- Layer 4: ground plane, voltage supply, signals

The thickness of the dielectric between the outermost layers and the one below is 0.17 mm, allowing transmission lines with compact dimensions. For 100 Ω differential lines a trace width of 0.2 mm and a distance between them of 0.15 mm result. For 50 Ω lines, the trace width is 0.36 mm and the distance to the ground plane is 0.2 mm. The PCB layout was done for Electromagnetic Compatibility (EMC) reasons. The upconverter was placed as close as possible to the output socket to minimize RF loss and ringing. The PLL, which generates the LO signal, was placed as close to the upconverter as the components allowed to keep the high frequency signal path as short as possible. The IC for clock distribution was placed next to the PLL. Linear voltage regulators were placed as close as possible to the ICs to be powered. Blocking capacitors were placed as close as possible to the IC to be blocked to minimize the propagation of interference between circuit parts, otherwise on the bottom side of the board so that routing on the top side could be optimized. FPGA and DAC were placed such that there was sufficient space between the ICs for the necessary electrical length compensation. The switching regulators were placed on the edge of the board opposite to the upconverter.

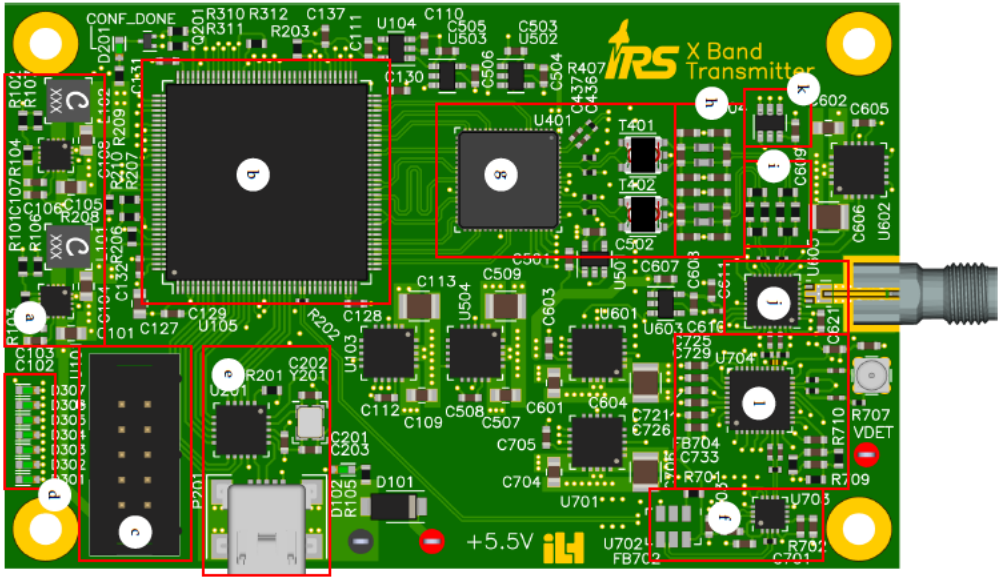

Figure 5-9: Top view of the assembled board (only upper layer presented). The ICs that are not labeled are linear voltage regulators. a) switching regulators for 3.3 V and 3.8 V; b) FPGA; c) JTAG interface for FPGA programming; d) LEDs; e) USB interface; f) clock generation and distribution; g) DAC; h) antialiasing filter; i) attenuator; j) upconverter; k) DAC for output power control; l) PLL. Taken from [85]

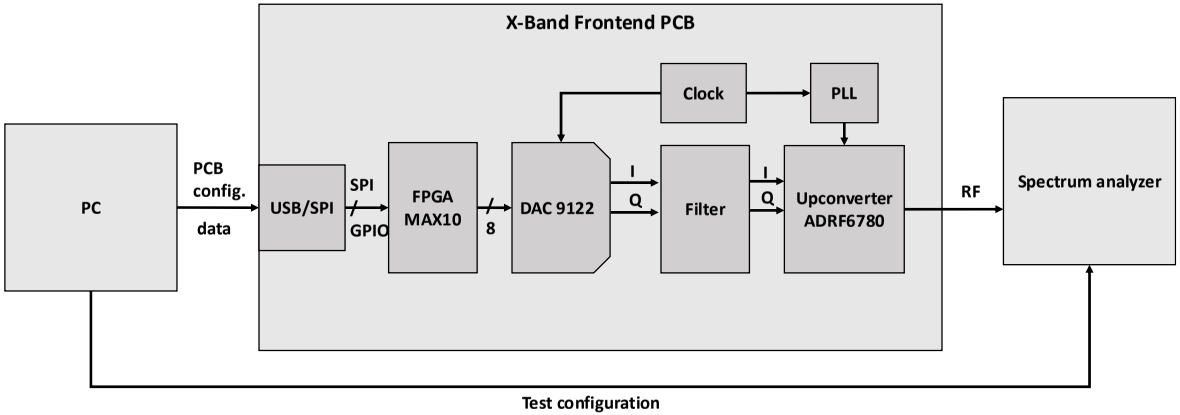

Figure 5-10: Test setup for the characterization of the analogue frontend PCB. The PC writes the desired configuration data into the transmitter and sets the configuration for the spectrum analyzer. The PC is connected to the transmitter via USB and the spectrum analyzer to the transmitter with a 50 Ω coaxial cable

For the single tone signal test, a complex sinusoidal signal of 20 MHz is generated. The spectrum at the output of the transmitter PCB can be seen in *Figure 5-11*. Similar to the evaluation of the ADRF6780 in 4.5.2, a dynamic range of more than 50 dB could be achieved.

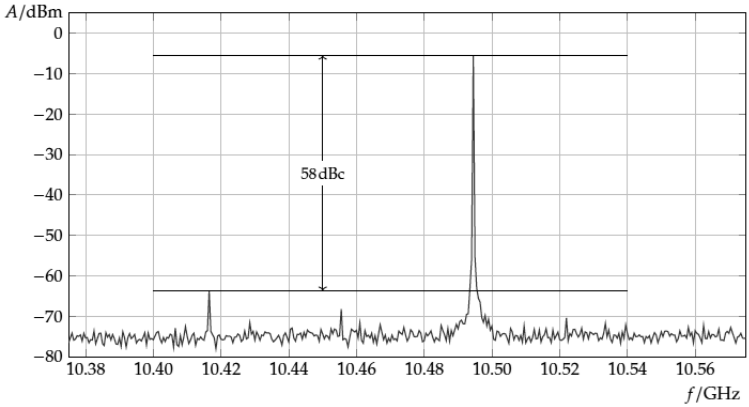

Figure 5-11: Single tone spectrum at the output of the transmitter PCB

The two tone tests were performed to characterize the intermodulation products. The two tone signal test comprises two complex sinusoidal signals at nearby frequencies. The spectrum is free of intermodulation products as can be seen in *Figure 5-12*. Yet, smaller peaks can be seen in *Figure 5-11* and *Figure 5-12* that show the feedthrough from the LO to the output of the upconverter.

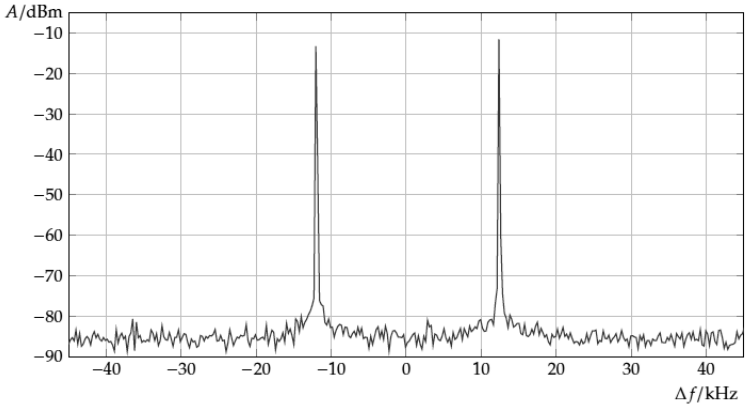

Figure 5-12: Two tone spectrum at the output of the transmitter PCB with an LO of 10.475 GHz

The EVM, as described in Eq. 2-8, is measured to characterize the quality of digital modulation and to evaluate the performance of the signal chain from DAC to upconverter. QPSK, 8PSK, 16APSK and 32APSK test signals were generated and loaded into the FPGA memory to be reproduced. The measured constellation diagrams are shown in *Figure 5-13*. The test showed that for 8PSK the EVM is -34 dB, for 16APSK -35 dB and for 32APSK -36 dB.

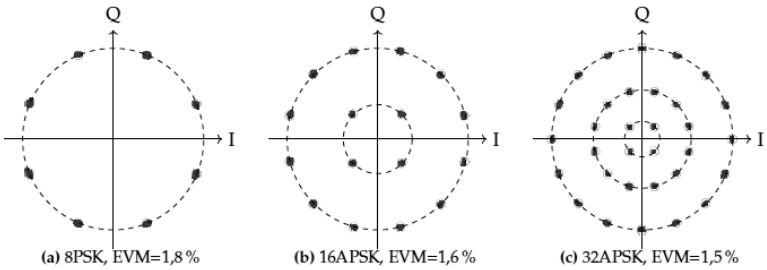

Figure 5-13: Constellation diagrams for a symbol rate of 41.55 Msps

5.2.1.5 Power consumption and thermal characteristics

The power consumption of the transmitter PCB was measured to compare the results to *Table 4-6*. The measured RF output power is 0 dBm, as expected from the datasheet of the ADRF6780 and the tests conducted in 4.5.2 The power consumption for the various operation modes of the transmitter PCB is shown in *Table 5-7*. Each operation mode includes the function groups of all preceding operation modes, consequently the operation mode "PLL" includes also the operation mode "FPGA, clock". The measured power consumption is around 1 W more than expected up to the upconverter stage. This is due to the measured power consumption of the FPGA, since estimated values were assumed for the resources. The power consumption with the DAC active corresponds to the expected values since worst case values from the data sheet for high sampling rates were assumed. This results in approximately 1 W less power consumption than expected and 1.5 W less than the power budget defined in *Table 4-6*. Thus, instead of 10 W, up to 11.5 W could be allocated to the PA module and the adaptive transmitter would still fulfil the requirement of 20 W power consumption as set in the requirements in *Table 4-1*.

Table 5-7: Power consumption of the transmitter PCB

Operation mode	**Expected power consumption**	**Measured power consumption**
FPGA, clock	1 W	1.9 W
PLL	2.7 W	3.9 W
Upconverter	5.7 W	6.5 W
DAC	8.5 W	8.3 W

Figure 5-14 shows the results of a test with a thermal camera. It can be seen that with the upconverter active, the temperature reaches up to 130°C. Yet, this temperature can be limited by adding dedicated copper layers to the PCB, or specifically in the region where the upconverter is or by adding a housing to dissipate the heat, which is currently being trade-offed from the thermal subsystem responsible.

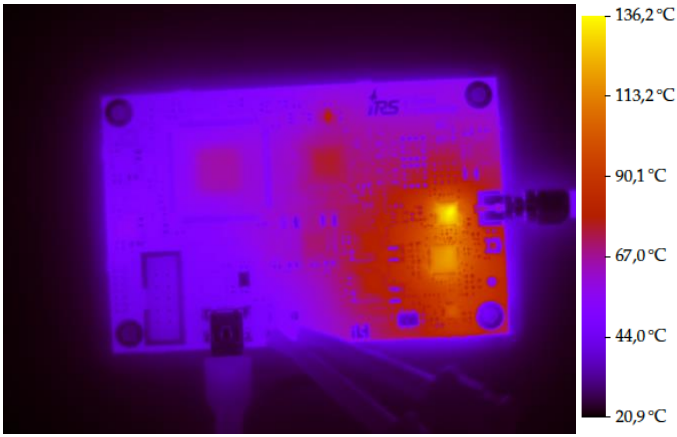

Figure 5-14: Thermal camera result of the transmitter PCB

After building, testing and characterizing the analogue frontend prototype, it is important to analyze the impacts of the test results on the ROMEO mission. The main characteristics of the analogue frontend PCB are listed in *Table 5-8*. The RF power output of 0 dBm corresponds to the test results in 4.5.2 and the RF level budget in *Table 3-6*. The total power consumption with 8.3 W is 0.2 W less than expected for this prototype as well as 1.7 W less than the expected power consumption defined in the power budget in *Table 4-6*. Yet, the analysis with the thermal camera showed that the thermal design should be optimized for the use on the ROMEO mission.

Table 5-8: Main characteristics of the analogue frontend prototype

Feature	Description
Carrier frequency	10.475 GHz
RF power output	0 dBm
Total power consumption	8.3 W
Dimensions	56 x 85 cm
Highest measured temperature during operation	130°C

To test the compatibility of the analogue frontend with the Xtra-Pro, breadboard model transmitter chain tests were conducted as described in the following section.

5.3 Breadboard model transmitter chain tests

A test setup as shown in *Figure 5-15*, was prepared to test the transmit chain from the XTra-Pro to the upconverter. To this purpose, the Zedboard with the AMD Xilinx Zynq-7020 SoC, a DAC AD9122 evaluation board and an upconverter ADRF6780 evaluation board were used. The measurements were carried out with a Rohde & Schwarz FSV3000 signal and spectrum analyzer. It includes the FSW-K70M software that allows to analyze digitally modulated signals as well as to demodulate and evaluate DVB-S2 signals. To analyze the DVB-S2 signal with the FSW-K70M software, the signal and spectrum analyzer filters the analog input signal with an intermediate frequency bandpass filter and, after analog-to-digital conversion, it digitally filters and decimates the signal for further processing with a digital signal processor. For the analysis of DVB-S2 signals, the I/Q samples are buffered and demodulated. To this purpose, the PL header of a frame is detected using the start of frame signal, and the demodulator is configured on the basis of the decoded information regarding modulation and code rate,

i.e. demodulation is possible on a frame-by-frame basis as described in 2.4.1. After the signal has passed the SRRC filter, carrier frequency and phase deviations can be detected and compensated. Based on the demodulated data, the quality of the transmitted signal with respect to the reference constellation can be determined. Before starting a measurement, parameters such as center frequency, symbol rate and roll-off factor must be specified. Note that the signal and spectrum analyzer is not CCSDS compatible, thus only the DVB-S2 implementation was analyzed.

The analog baseband signal at the DAC's output and the RF frequency signal at the upconverter's output were analyzed during the tests and are detailed in section 5.3.1 and 5.3.2, respectively. The Zedboard implementation of 5.1.1 was used for these tests.

5.3.1 Test of the complex baseband signal

EVM and MER, as defined in Eq. 2-8 and Eq. 2-10, were used to analyze the analog complex baseband signal of the DAC output. Signal attenuation was simulated with the gain parameter in the DVB-S2 modulator (igain), resulting in a lower SNR. The DAC AD9122 evaluation board has two integrated 16-bit DACs that convert the digital I and Q data to an analog signal. At its input, the DAC has a 2-channel, 16-bit, eight-word deep FIFO buffer to compensate for delays in the incoming data. After upsampling, the digital signals pass through three adjustable interpolation filters. Each of these filters provides a 2x increase in output data rate and each filter can be individually bypassed or cascaded to provide 1x, 2x, 4x or 8x interpolation ratios. In this case an 8x interpolation ratio is used. This interpolated signal can either be output directly or additionally filtered by a low-pass filter.

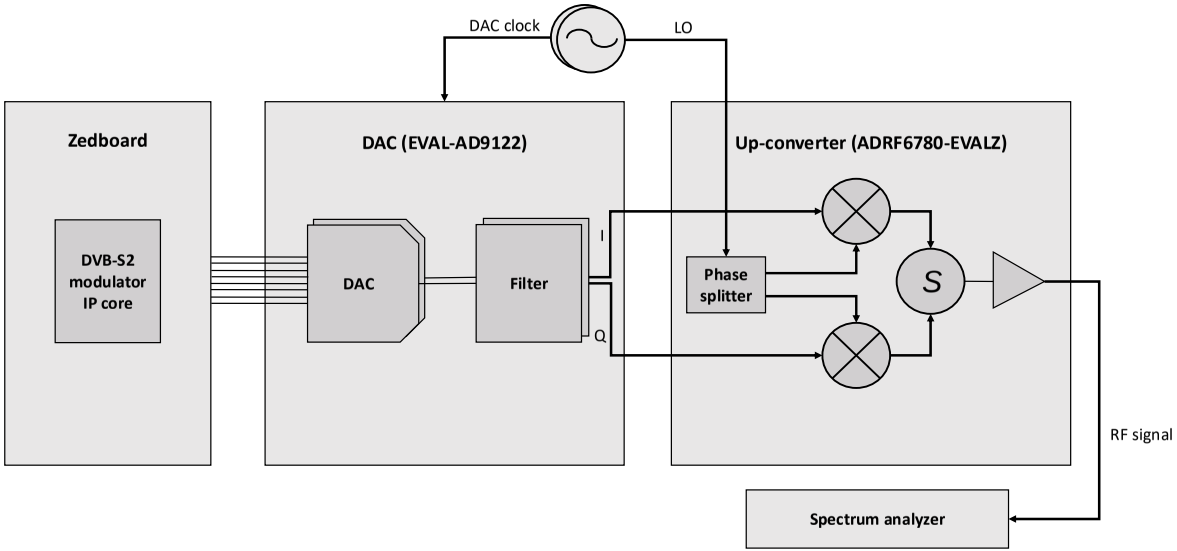

Figure 5-15: Test setup for the breadboard model transmitter chain test. The dashed lines to the spectrum analyzer correspond to the test for the complex baseband at the output of the DAC and the full line to the spectrum analyzer shows the signal path used for testing the upconverter's RF output. The filter in the DAC evaluation board are passband filters

The data transmission between the Zedboard and the DAC uses an FPGA Mezzanine Card (FMC) interface. The input interface of the DAC consists of a 16-bit wide data bus, and the DCI and FRAME signals for synchronization as described in 5.2.1.2. The data is transmitted on the rising and the falling edge of the DCI signal, i.e. at double data rate (DDR). The joint transmission of reference clock and data reduces the influence of delays and runtime differences enabling the use of high data rates without defining additional constraints on the transmission path and clock distribution. However, synchronization is required, which in this case is realized by the DAC's FIFO buffer. It must be ensured that the clock frequencies are identical to avoid data loss due to buffer over- or underflow. The implementation of the DMA described in 5.1.1 was modified by combining the 16-bit wide in-phase and quadrature data into a 32-bit word and forwarding it via an IO function block to the pins of the FMC interface as shown in *Figure 5-16*. Hence, the 32-bit IQ data stream is serialized in order to be transferred at double data rate over the 16-bit wide bus at the same clock rate. The DAC board provides the FPGA clock via the FMC interface as Data Clock Output (DCO).

The clock signal is routed to the mixed-mode clock manager (MMCM) module in the programmable logic. This is necessary to guarantee an identical clock frequency for the FPGA and the DAC. If the clock would be generated by the oscillator on the Zedboard, data loss due to buffer over or underruns might occur due to the frequency inaccuracy of the oscillator.

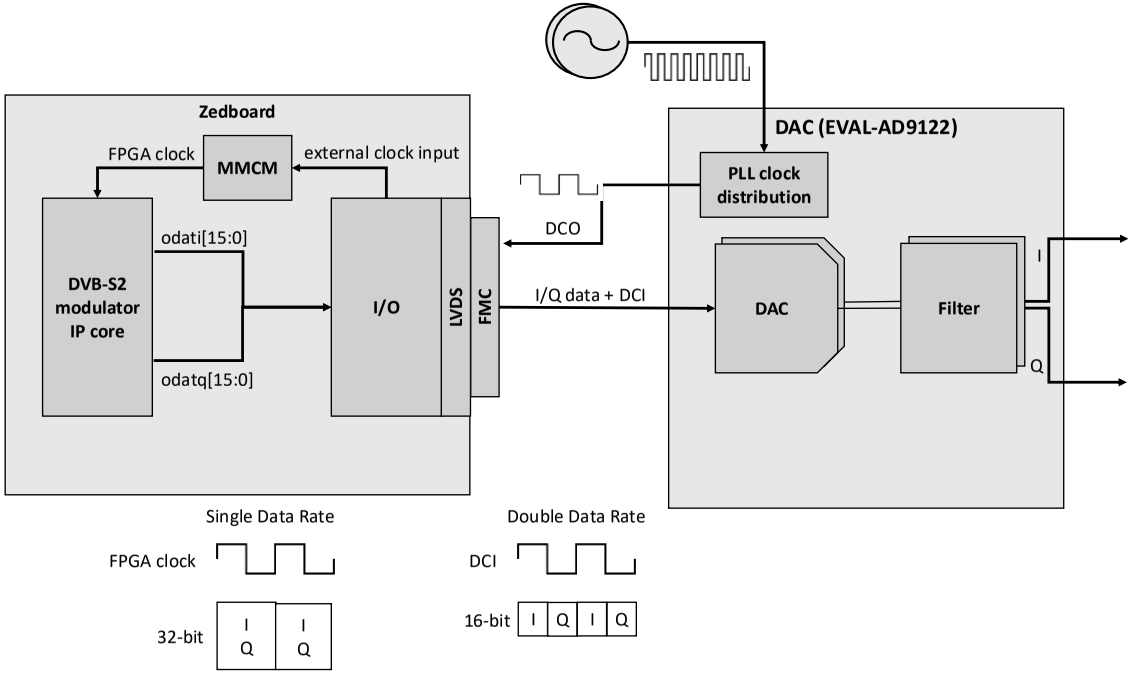

Figure 5-16: Test setup for the DAC in the breadboard model transmitter chain test. The I/O function block was implemented on the Zedboard to forward the 32-bit word to the pins of the FMC interface

The received modulated signal was analyzed using the FSV300, which provided information on modulation accuracy measuring EVM and MER. Furthermore, the peak EVM is measured over time. The EVM figure of <1% in the analysis of a 32APSK 9/10 signal in *Figure 5-17* clearly shows that the DAC does not considerably degrade the transmitted signal of the XTra-Pro's output.

A bit error measurement was used to analyze the relation between the measured signal quality and the required threshold values as shown in *Table 5-9*. An upper threshold for MER and EVM could be observed, due to the implementation of the demodulation process. The resolution of the signal and spectrum analyzer's ADC limits the maximum feasible measured modulation accuracy. As a result, quantization noise leads to inaccurate measurements for very low power signals due to the noise. For measurements with intermediate signal strength, a linear dependency between attenuation (configured with the igain parameter of the DVB-S2 modulator) and MER could be observed. The attenuation on the transmission path determines the EVM of the received signal. The MER should be lower than the SNR since it considers additional inaccuracies of digital modulation schemes rather than just the useful signal power. Assuming that the predominant source of interference is noise, both parameter values are approximately the same. The higher the attenuation, the higher the quantization error of the DAC of the transmitter and of the ADC of the signal and spectrum analyzer since the resolution is not sufficient. Thus, bit errors are generated by quantization noise and not by channel impairments.

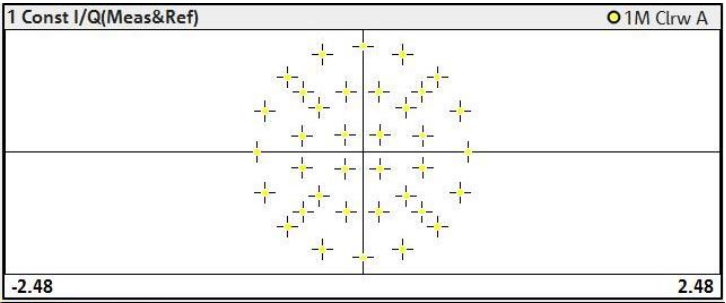

2 Result Summary

		Current	Peak	Unit
EVM	RMS	0.65	0.65	%
	Peak	1.82	1.88	%
MER	RMS	43.76	43.76	dB
	Peak	34.81	34.50	dB
Phase Error	RMS	0.40	0.41	deg
	Peak	-2.82	2.86	deg
Magnitude Error	RMS	0.46	0.46	%
	Peak	-1.67	-1.78	%
Carrier Frequency Error		23.96	24.28	Hz
Symbol Rate Error		---	---	ppm
I/Q Skew		---	---	ps

Figure 5-17: Analysis of an 32APSK 9/10 signal with the FSV3000. The symbol rate was set to 41.55 Msps, the roll-off to 0.2. It can be seen that the signal and spectrum analyzer is able to demodulate the signal correctly. The rms EVM is below 1%

Table 5-9: Measurement of signal quality and bit error rate for attenuated signals. The measurements were made with an 32APSK 9/10 signal as shown in Figure 5-17

Attenuation [dB]	BER	EVM_{RMS} [%]	EVM_{Peak} [%]	MER_{RMS} [dB]	Power [dBm]
0	0	0.65	1.92	43.79	-8.98
10	0	0.70	2.18	43.05	-19.31
20	0	1.20	3.56	38.44	-29.31
30	0	3.29	10.33	29.65	-39.30
35	3.45×10^{-7}	5.81	17.03	24.71	-44.26
40	1.23×10^{-3}	10.22	30.47	19.81	-49.23

5.3.2 Test of the upconverter output signal

After the signal quality of the baseband signal at the DAC's output was examined, the experimental setup of 5.3.1 was expanded to include the upconverter. The test setup is shown in *Figure 5-15* with the full line applicable. The ADRF6780 evaluation board was used that allows direct upconversion or single sideband modulation of an intermediate frequency signal. The input and output interfaces of the upconverter are differential. For this purpose, two wideband baluns are used to match the RF output to the unbalanced input of the signal and spectrum analyzer and also to feed the LO signal of a signal generator. The DAC's differential in-phase and quadrature signals were connected to the upconverters' input. The RF carrier frequency was generated using a signal generator. First, the upconverter was tuned to compensate for amplitude and phase imbalance. This tuning was performed using a 5 MHz test tone generated by the SoC and converted to 3.2 GHz by the upconverter. The amplitude and the phase shift for the in-phase and quadrature components were selected by the DAC. This allowed to minimize the amplitude of the suppressed sideband and of the feedthrough from the LO to the output of the upconverter. After the tuning, the LO feedthrough could be reduced to 40 dBm and the sideband suppression to 30 dBm. For comparison, a typical value of 25 dBm LO feedthrough and 25 dBc sideband suppression is specified in the datasheet of the ADRF6780 upconverter [73].

In comparison to the baseband signal, the RF signal was impaired previous tuning of the in-phase and quadrature components. The differences before and after tuning were measured with the signal and spectrum analyzer and are listed in *Table 5-10*. The EVM before tuning increased to 8% w.r.t the baseband signal, mainly due to a quadrature error, i.e. a phase shift of 7.7° leading to a skewed constellation. Other contributions are the I/Q offset and the I/Q imbalance representing the DC offsets introduced in the I and Q signal

components and the difference in gain between the I and Q signal components leading to an asymmetric constellation, respectively. The phase error could be reduced by adjusting the phase and amplitude at the DAC, reducing the EVM to 4.5%. The difference before and after tuning, mainly the I/Q offset and the quadrature error can be seen in *Figure 5-18* for a 32APSK 9/10 signal. Other contributions to the EVM degradation presumably are due to the signal generator's phase noise and to residual mismatch of the couplers and the limited I/Q balance of the upconverter itself.

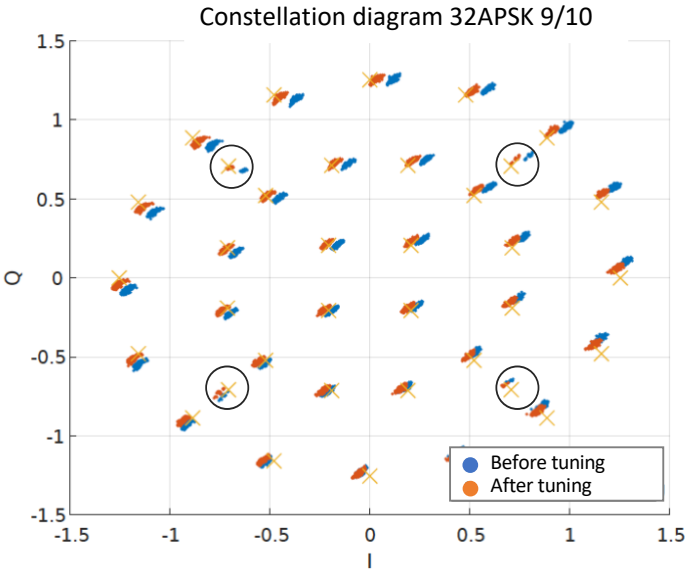

Figure 5-18: Distortion of the constellation before and after tuning of the I/Q-imbalance of a 32APSK 9/10 signal (code rate not visible). The $\pi/2$ QPSK-constellation points, shown with the grey circles, that correspond to the pilot symbols are visible

Table 5-10: Signal quality after the upconverter before and after tuning with an analogue baseband output and with an intermediate frequency as output (after tuning)

	EVM_{RMS} [%]	**EVM_{Peak} [%]**	**I/Q offset [dB]**	**Quadrature error (°)**	**I/Q imbalance [dB]**
Before tuning	8	16.1	-28.8	-7.7	-23.5
After tuning	4.5	10.4	-35.4	-4.2	-28.7
Intermediate frequency	2.2	5.8	-72.5	0.01	-84.2

The signal quality was improved significantly when using an IF of 50 MHz instead of using an analogue baseband output, since the I/Q errors had no effect on the used sideband. However, interference by the carrier itself and by the suppressed sideband occurred. This interference was limited by the bandpass filter of the signal and spectrum analyzer. For the envisaged transmitter, a bandpass filter after the upconverter or after the PA module might be mandatory to fulfil the bandwidth limitation of 50 MHz set by the ITU.

5.3.3 Ground segment

The functionality of the adaptive transmitter for the ROMEO mission also has an impact on the ground segment. Two ground stations with the parameters listed in *Table 3-2* were designed and built for the ROMEO mission. For details on the design and built process, see [89]. The ground stations were designed taking into account worst case link budget conditions for ROMEO as discussed in 3.3 *Figure 5-19* shows the two ground stations of IRS at the University of Stuttgart, including the ground station for ROMEO.

The compatibility between the ground segment and the ROMEO satellite is assured with a CCSDS over DVB-S2, i.e. a CCSDS 131.3-B-1 (as described in 2.4.1.2) compatible modem. A market research showed that there are either CCSDS 131.3-B-1 modems which do not support the ACM mode or DVB-S2 ACM compatible modems without CCSDS compatibility. Thus, a mission-specific modem had to be designed. The company TXMISSION built a modem that meets the requirements of the ROMEO mission listed in *Table 4-1*.

Table 5-11 summarizes the main characteristics of the TXMISSION modem. Besides the CCSDS over DVB-S2 compatibility, the Doppler limits are an important aspect for the ROMEO mission. As shown in *Figure 3-12*, the Doppler shift varies between ±250 kHz and ±270 kHz, and the Doppler rate between ±3 kHz/s and ±5.7 kHz/s. The TXMISSION modem can

operate within these Doppler limits as can be seen in *Table 5-11*.

Figure 5-19: Two ground stations at IRS of the University of Stuttgart. On the left: the 2.5 m S-band ground station which is used for the current satellite mission. On the right: the new 4.5 m ground station developed and built for the ROMEO mission with the parameters of Table 3-2. The STR and MAL ground station are identical

5.3.3.1 ACM control loop

An important aspect is the ACM control loop since an estimation of the signal quality has to be made at the ground segment to define the best-suited MODCOD for the current channel state. A main factor to consider is the loop delay and the MODCOD changes decided by the ACM estimator after the ground modem (as shown in *Figure 3-13*). The loop delay for the ROMEO mission was shown in *Table 3-8*. The accuracy and the execution time have a significant impact on the added of the use of ACM. Furthermore, estimation errors of the ACM control loop have to be considered. Less estimation errors can

reduce the uplink MODCOD change commands by avoiding spurious adjustments in the case of highly fluctuating estimated values.

Table 5-11: Main characteristics of the TXMISSION modem for the ROMEO ground stations

Feature	**Description**
Function	Tx and Rx
Data rate	Up to 500 Mbps (119 Msps, according to MODCOD28 as referred to in Table *A-1*)
Waveforms (according to Table *A-1*)	DVB-S2: QPSK, 8PSK, 16APSK & 32APSK operation per EN 302 307-1. Includes 5%, 10%, 15%, 20%, 25% & 35% roll-off CCSDS DVB-S2 as defined in CCSDS 131.3-B-1
VCM	Variable coding and modulation mode for use with DVB-S2
ACM	Adaptive coding and modulation mode for use with DVB-S2
Frequency range	Tx & Rx: Supports frequencies up to 6 GHz (IF operation at 70 MHz). Tx will be used for the S-band telecommand transmission Tx & Rx: Supports other frequency bands when used with external frequency conversion (which is needed for the operation at 10.475 GHz)
Doppler limits	Up to ±700 kHz, ±9 kHz/s
Others	Interfaces: Gigabit Ethernet Data conversion to IP
Output power	-40 to -5 dBm (S-band uplink only)

The DVB-S2 standard proposes the use of the Signal to Noise Ratio Estimation (SNORE) channel estimator algorithm, which was developed by NASA. This algorithm provides, based on the pilot symbols, an accurate estimation of the signal to noise and interference ratio for the E_s/N_0 range of interest. This algorithm leads to channel estimation delays in the order of 10 ms for an error standard deviation of about 0.2 dB. Since the E_s/N_0 difference between the physical layer schemes is in the order of 1 dB, the DVB-S2 standard recommends an error standard deviation better than 0.3 dB to fully exploit the system capabilities [42].

NASA observed in their SCaN testbed on the ISS that spurious MODCOD adjustment were made by the ACM controller of the used ground modem due to the variance of the signal quality estimation as shown in *Figure 5-20* [17].

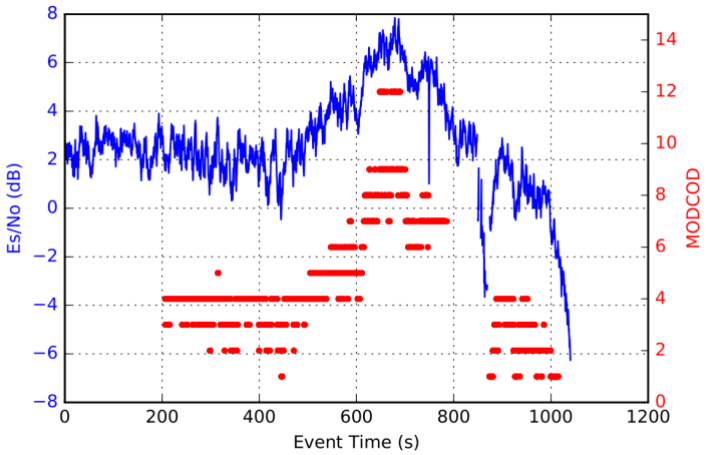

Figure 5-20: Protocol of an ACM controller for adaptive transmission [17]. Due to the variance of the signal quality estimation of the modem, spurious MODCOD adjustments occur

NASA further studied the use of different deep reinforcement learning algorithms for the MODCOD change decision and tested them on the ISS testbed [90], [91]. It was the first time that reinforcement learning for multi-objective optimization on a space test setup was demonstrated. The test onboard the ISS showed that machine learning decisions could be used to configure a link from the ISS testbed to the ground station to achieve multiple objectives regarding data throughput, bandwidth, and power. An average accuracy higher than 80% was achieved during all the different test setups [90]. These algorithms were made available from NASA. These algorithms will be used and optimized for the ROMEO ground segment to improve the ACM control loop and thus the overall mission data throughput. The optimization will further include external sensor data like for example data from a weather station that includes the rain rate. This data as well as learning data from the current satellite mission, will be used on the forthcoming work in the ROMEO project to predict the best MODCOD for the current transmission state for the different IRS ground stations.

5.4 Discussion of the results

In this section the results of the tests made in 5.3 are summarized and discussed. The current status of the tests as well as the concepts developed and the analysis performed in chapter 4 are summarized in *Table 5-12*.

In a first step, the digital signal processing algorithms were tested and verified. An adaptive DVB-S2 modulator was implemented including the CCSDS compatibility according to [61] on a Zedboard. For this purpose, interfaces for control and for input and output of data were developed. The function of the XTra-Pro implementation could be verified by analyzing the EVM and MER of the output data. A video file was stored in the DDR3 RAM of the Zedboard which subsequently was processed

by the DVB-S2 modulator IP core and decoded with the SDRangel tool.

In a second step, the ACM mode of the DVB-S2 IP core was tested successfully. The utilization of the programmable logic for the implementation is < 40% of the LUTs with a triple modular redundancy for the CCSDS IP core. This provided sufficient capacity to further include functions in the PL, like for example attitude and orbital control algorithms of ROMEO. The estimated power consumption of the XTra-Pro was ~2 W. This implementation and evaluation of the digital signal processing algorithms on the Zedboard showed that it meets the requirements of *Table 4-1*. At time of designing the XTra-Pro, testing and evaluating the results, the supervisor IC and the core avionics was still unavailable, and therefore implementation of the digital signal processing, tests and evaluations were performed on an evaluation board with the SoC only. Thus, XTra-Pro must be adapted to the core avionics PCB. This meaned that the implementation had to be expanded to connect the SoC with the supervisor and to the memories that store the scientific data of the mission. Furthermore, the CCSDS over DVB-S2 compatibility has to be analyzed in more detail since the TXMISSION modem was not procured during the time of the thesis and thus, end-to-end tests for the CCSDS over DVB-S2 compatibility could not be performed.

In a third step, a prototype containing the analogue components (except for the PA module) selected in 4.5 was designed, tested and characterized. First, a circuit diagram and a PCB layout were designed comprising the analogue components. The analogue components were controlled by means of a MAX10 FPGA through an SPI interface while the FPGA was controlled through an USB interface. The PCB was successfully tested with a single tone and a two-tone test. The EVM was analyzed for QPSK, 8PSK, 16APSK and 32APSK signals. The RF output power was 0 dBm and the measured power consumption with 8.3 W was 0.2 W less than expected since the

expected power consumption of the DAC was based on the worst case values for high sampling rates. The thermal analysis of the PCB with a thermal camera showed that the temperature in the region of the upconverter reaches 130°C since no focus was put on the thermal requirements for this prototype. Thus, dedicated copper layers will be added on the engineering model (EM) to dissipate the heat. The requirement of maximum 20 W and the RF level budget, as listed in *Table 4-6* and *Table 3-6*, for the adaptive transmitter, considering also the PA module and antenna characteristics are fulfilled.

In a breadboard model test setup, the output signal after the DAC and the high frequency signal after upconversion was tested with a signal and spectrum analyzer. The test showed that the DAC as well as the upconverter do not significantly degrade the EVM and MER. This was evaluated using the EVM figure which was <1% after the DAC and 2% after the upconverter. Yet, it is important to further characterize the EVM and MER since the PA module may introduce signal distortions which are expected to depend on the used MODCOD. Using of higher-order modulation schemes such as 16APSK and 32APSK, signal distortions may be introduced by the PA module due to the non-linearity since the distribution of constellation points over multiple concentric circles increases sensitivity to non-linear distortion as simulated and discussed in 4.5.4. To limit signal distortion as characterized by EVM and MER, the backoff should be adapted to the current modulation scheme. Furthermore, the transmit signal can be pre-distorted to match the non-linearities of the PA module as described in 4.5.4. Furthermore, the PA module and the patch array antenna have to be RF matched.

Different further topics have to be considered in order to enable the use of the adaptive transmitter on the ROMEO mission. An important aspect is the ACM control loop. For the ACM control loop, channel estimation must be performed at the ground station, for example using the deep reinforcement

learning algorithms from NASA as introduced in 5.3.3. The performance of the control loop is determined by estimation accuracy and processing delay. Based on the estimation of the algorithm, a suitable MODCOD is selected at the ground station modem. It is expected that spurious MODCOD jumps can be eased by hysteresis, and the throughput be optimized.

Table 5-12: Current status of the test and verification matrix regarding the requirements that were listed for the adaptive transmitter in Table 4-1

Parameter	**Requirement**	**Verification method**	**Current status**
Frequency band	Ham radio X-Band (10.45 – 10.5 GHz)	Test	Verified with test in 5.2 and 5.3
Bandwidth	50 MHz max.	Test	Verified with test in 5.2 and 5.3
Data Volume	Min. 15 GB/day	Analysis	Verified in the link budget and ACM assessment analysis in 3.4
Data rate	Variable	Test	Verified with test in 4.4.3 and 5.1
RF output power (saturation)	33 dBm, according to 3.3.2	Concept analysis	Verified with concept analysis made in 4.5.4
Antenna gain	Min. 16 dBi, according to 3.3.2	Simulation	Verified with concept and simulation analysis in 4.5.5
Power Consumption	20 W	Concept analysis	Verified with tests and analysis made in 4 and 5
CCSDS compatibility	Yes	Test	Verified with test in 5.1
Coding and modulation	DVB-S2 standard	Test	Verified with tests in 5.1 and 5.3
Radiation tolerance	TID 8.2 krad min., according to [50]	Concept	Radiation shielding equivalent to a 10 mm full sphere of aluminum

6 Conclusion and outlook

In this thesis possible designs for an adaptive ham radio X-band transmitter system with maximum 50 MHz bandwidth and 2 W RF output power for use on a small satellite in a MEO have been investigated. In order to provide the flexibility of adapting the transmitter configuration to the current transmission state, DVB-S2 waveforms with ACM mode implemented on a System on Chip were considered.

The use case on the ROMEO mission was outlined in order to define the requirements of the adaptive transmitter. The ROMEO satellite will be launched into a 600 km SSO orbit and then use its propulsion system to reach an elliptical orbit with an apogee of ca. 3000 km and a perigee of ca. 300 km altitude. An orbit analysis showed the ground station contact times per day for the IRS ground stations of the University of Stuttgart for the different mission phases. This was used to analyze the use of the different DVB-S2 waveforms during the different ROMEO mission phases and to define an operational concept. The link budget analysis showed the most robust DVB-S2 waveform necessary to close the link as well as that the minimum required EIRP for the whole mission of 16.4 dBW, considering 2 dB amplifier backoff. Furthermore, a parametric link budget analysis showed that most of the parameters have a slow variation that can be tracked and compensated through ACM (free space loss, atmospheric loss due to clouds and gases, scintillation effects, satellite and ground station antenna pointing offsets) and rain loss and interferences due to intermodulation or other carriers are parameters with a fast variation that can be difficult to track and should be considered in the ACM margin. Overall, the use of the ACM mode showed that the data volume per day could be increased by 134% up to 436%, depending on the ROMEO mission phase.

A design concept for the adaptive transmitter system was defined that fulfills the ROMEO requirements. First, the

detailed architecture of the XTra-Pro was defined and the implementation of the digital signal processing on it was successfully evaluated. These evaluations included the successful test of the DVB-S2 ACM mode. Since the components of the analogue frontend potentially can degrade the signal quality after the XTra-Pro, several trade-offs were performed in order to select the best-suited components for the analogue frontend. For the PA module and for the patch array antenna, simulations were carried out which showed the influences of these on the other components of the transmit chain and to show the feasibility of a 16.4 dBW EIRP. The evaluation of the remaining components of the analogue frontends was performed on a prototype. This validated the trade-off of the components and showed the feasibility of using them on the adaptive transmitter of ROMEO.

A breadboard transmitter chain test was performed to evaluate the output signal after the DAC and the upconverter, respectively using a signal and spectrum analyzer. The digital signal processing algorithms, which will be used on ROMEO, were implemented on a Zedboard. The test showed that neither the DAC nor the upconverter significantly degrade the EVM and the MER after the digital signal processing. This showed that the design concept made for the adaptive transmitter system fulfils the ROMEO mission requirements.

In conclusion, this thesis has shown an innovative approach and the potential of an adaptive transmitter system for use on a small satellite mission to the MEO. Several additional aspects have been investigated like the interaction between the space and the ground segment, the development of a ground station for the mission and the possible use of machine learning algorithms for the channel state estimation on ground have been introduced. Furthermore, this thesis has shown that standards typically used on GEO satellites, can be adapted for use on LEO and MEO satellite missions. Yet, some additional aspects are worth to be further investigated.

Firstly, it is important to characterize the influence of the PA module on the current design to better manage signal integrity. Thus, a more detailed analysis on the influence of the PA module to the different modulation schemes used is necessary. The transmit signal can also be pre-distorted to counteract the effects of the PA module, depending on the MODCOD.

Secondly, the simulations for the patch array antenna have to be detailed to provide a more realistic design. For example, the influence of the coaxial feed and the microstrip feeding lines have to be further analyzed in order to provide a patch array antenna design with sufficient XPD and boresight gain. The PA module and the patch array antenna also have to be RF matched to not introduce further signal loss in the signal patch.

Thirdly, the design has to be adapted to the core avionics. Once the core avionics board has been designed, the digital signal processing algorithms have to be implemented on the SoC, which also hosts OBDH functionalities.

Fourthly, the adaptive transmitter system has to be compatible to the S-band telecommand and telemetry system and to be able to interact with the ground segment. The S-band system receives the MODCOD change telecommand and has to provide this information to the adaptive transmitter that has to change the MODCOD accordingly to the received telecommand. The ground segment has to provide a reliable ACM algorithm that provides the current channel state information in order to choose the best-suited MODCOD. This has to be investigated by means of different machine learning algorithms, for example like the one provided from NASA.

Finally, there are several more steps to be taken to assure the reliability of the adaptive transmitter for the space environment. This includes environmental tests to assure that the functionality of the adaptive transmitter does not degrade in vacuum, and for the expected temperature range and radiation exposure. This will include thermal-vacuum tests and

radiation tests like failure injection tests, for example to assure that the transmitter still functions after experiencing SEEs.

The increasing number of satellites in orbit come with increasing requirements for high data rate transmissions. An increase in the flexibility of the communication system by adapting its current transmitter configuration to the current channel state information provides more flexibility and in turn increases the mission-return. The potential of the adaptive transmitter, especially of the implemented ACM mode, is not only relevant for the ROMEO mission but also for other space missions, especially for those missions having ground stations located in climatic regions with high rain loss or for satellite constellations where each satellite has a limited ground station contact window.

7 Bibliography

[1] J. Hayes, “Adaptive Feedback Communications,” *IEEE Trans. Commun.*, vol. 16, no. 1, pp. 29–34, Feb. 1968, doi: 10.1109/TCOM.1968.1089811.

[2] A. S. Mohd Anuar, W. N. W. Muhamad, D. Mohd Ali, S. S. Sarnin, and N. A. Wahab, “A review on link adaptation techniques for energy efficiency and QoS in IEEE802.11 WLAN,” *Indones. J. Electr. Eng. Comput. Sci.*, vol. 17, no. 1, p. 331, Jan. 2020, doi: 10.11591/ijeecs.v17.i1.pp331-339.

[3] ETSI EN 302 307-1 V1.4.1 (2014-11), “Digital Video Broadcasting (DVB); Second generation framing structure, channel coding and modulation systems for Broadcasting, Interactive Services, News Gathering and other broadband satellite applications; Part 1: DVB-S2.”

[4] G. Gardikis, N. Zotos, and A. Kourtis, “Satellite Media Broadcasting with Adaptive Coding and Modulation,” *Int. J. Digit. Multimed. Broadcast.*, vol. 2009, pp. 1–10, 2009, doi: 10.1155/2009/879290.

[5] Meixiang Zhang, Sooyoung Kim, Jeong-Ki Pack, and I.-K. Kim, “A dynamic rain attenuation model for adaptive satellite communication systems,” in *2011 IEEE 7th International Conference on Wireless and Mobile Computing, Networking and Communications (WiMob)*, Shanghai, China, Oct. 2011, pp. 74–79. doi: 10.1109/WiMOB.2011.6085350.

[6] P. Skoutaridis, C. Kasparis, and B. Evans, “Adaptive Coding and Modulation for Vehicular Satellite Communications,” presented at the 25th AIAA International Communications Satellite Systems Conference (organized by APSCC), Seoul, South Korea, Apr. 2007. doi: 10.2514/6.2007-3178.

[7] Lee, Jaeyoon, Yoon, Dongweon, and Lee, Woo-Ju, “Adaptive Coding and Modulation Scheme for Ka Band Space Communications,” *J. Astron. Space Sci.*, vol. 27,

no. 2, pp. 129–134, Jun. 2010, doi: 10.5140/JASS.2010.27.2.129.

[8] D. Breynaert, “Analysis of the bandwidth efficiency of DVB-S2 in a typical data distribution network,” *CCBN2005 Beijing*, Mar. 2005.

[9] S. Kim, D. Oh, and J. Park, “Standardization on performance objectives of satellite systems using adaptive coding and modulation,” *Int. J. Satell. Commun. Netw.*, vol. 38, no. 2, pp. 200–208, Mar. 2020, doi: 10.1002/sat.1335.

[10] C. Wang, D. Bian, F. Li, Y. Li, and J. Hu, “Subset Optimization of Adaptive Coding and Modulation Modes According to DVB-S2X,” presented at the 2018 International Workshop on Bioinformatics, Biochemistry, Biomedical Sciences (BBBS 2018), Hangzhou City, China, 2018. doi: 10.2991/bbbs-18.2018.46.

[11] J. P. Choi and V. W. S. Chan, “Adaptive communications over fading satellite channels,” in *ICC 2001. IEEE International Conference on Communications. Conference Record (Cat. No.01CH37240)*, Helsinki, Finland, 2001, vol. 9, pp. 2635–2639. doi: 10.1109/ICC.2001.936628.

[12] Recommendation ITU-R S.2131-1, “Method for the determination of performance objectives for satellite hypothetical reference digital paths using adaptive coding and modulation”.

[13] K. Devaraj, R. Kingsbury, M. Ligon, J. Breu, V. Vittaldev, B. Klofas, P Yeon, and K. Colton, “Dove High Speed Downlink System,” presented at the Small Satellites Conference, SSC17–VII–02.

[14] M. Darmetko, S. Kozlowski, K. Kurek, J. Skarzynski, K. Modelski, K. Szczygielska, and M. Stolarski, “Adaptive communication system using software defined radio,” in *2015 IEEE MTT-S International Microwave and RF*

Conference (IMaRC), Hyderabad, Dec. 2015, pp. 185–187. doi: 10.1109/IMaRC.2015.7411441.

[15] J. Downey, M. Evans, J. Downey, R. Reinhart, and D. Mortensen, "Bandwidth-Efficient Communication through 225 MHz Ka-band Relay Satellite Channel," presented at the 34th AIAA International Communications Satellite Systems Conference, Cleveland, OH, Oct. 2016. doi: 10.2514/6.2016-5737.

[16] A. Lamoral Coines and V. P. G. Jiménez, "CCSDS 131.2-B-1 Transmitter Design on FPGA with Adaptive Coding and Modulation Schemes for Satellite Communications," *Electronics*, vol. 10, no. 20, p. 2476, Oct. 2021, doi: 10.3390/electronics10202476.

[17] J. A. Downey, M. A. Evans, and N. S. Tollis, "DVB-S2 Experiment Over NASA's Space Network," 2017, [Online]. Available: https://ntrs.nasa.gov/api/citations/20170006587/downloads/20170006587.pdf?attachment=true

[18] J. P. Millerioux, J. L. Issler, C. Dudal, G. Moury, and J. M. Soula, "DVB-S2: A versatile COTS and CCSDS standard for telemetry applications," presented at the ESA TTC Conference, 2016.

[19] E. Inceoz, R. Tutgun, and A. M. Y. Turgut, "FPGA Based Transmitter Design Using Adaptive Coding and Modulation Schemes for Low Earth Orbit Satellite Communications," in *2020 IEEE 5th International Symposium on Telecommunication Technologies (ISTT)*, Shah Alam, Malaysia, Nov. 2020, pp. 39–44. doi: 10.1109/ISTT50966.2020.9279382.

[20] S. Kozlowski, K. Kurek, J. Skarzynski, K. Szczygielska, and M. Darmetko, "Investigation on adaptive satellite communication system performance using SDR technique," in *2018 22nd International Microwave and Radar Conference (MIKON)*, Poznan, Poland, May 2018, pp. 363–366. doi: 10.23919/MIKON.2018.8405226.

[21] Y. Wong, S. Schaire, S. Bundick, P. Fetterer, T. Perrotto, P. Celeste, and B.A. Hamilton, “NASA Near Earth Network (NEN) DVB-S2 Demonstration Testing for Enhancing Higher Data Rates for CubeSat/Small Satellite Missions at X-band and Ka-band,” p. 13.

[22] S. Kozłowski, K. Kurek, J. Skarzyński, K. Szczygielska, and M. Darmetko, “Verifying a concept of adaptive communication with LEO satellites using SDR-based simulations,” *Int. J. Microw. Wirel. Technol.*, vol. 11, no. 7, pp. 602–608, Sep. 2019, doi: 10.1017/S1759078719000552.

[23] M. Fernandez, A. Latiri, T. Dehaene, G.Michaud, C. Dudal, P. Lafabrie, A. Gaboriaud, J.-L. Issler, F. Rousseau, A. Ressouche, and J.-L. Salaun, “X Band Transmission evolution towards DVB-S2 for Small Satellites,” presented at the Small Satellites Conference SSC16-VII-6.

[24] C. Sauer, J. Dickinson, and M. Epperly, “A reconfigurable, radiation tolerant S-Band radio for space use,” in *2011 Aerospace Conference*, Big Sky, USA, Mar. 2011, pp. 1–6. doi: 10.1109/AERO.2011.5747365.

[25] Y. Wang, Q. Zhang, M. Zhang, and L. Wang, “Analysis and Simulation of Adaptive Coding and Modulation for Remote Sensing Satellite,” in *2018 IEEE 3rd Advanced Information Technology, Electronic and Automation Control Conference (IAEAC)*, Chongqing, China, Oct. 2018, pp. 567–570. doi: 10.1109/IAEAC.2018.8577644.

[26] L. D. Earley, “Communication in Challenging Environments: Application of LEO/MEO Satellite Constellation to Emerging Aviation Networks,” in *2021 Integrated Communications Navigation and Surveillance Conference (ICNS)*, Dulles, VA, USA, Apr. 2021, pp. 1–8. doi: 10.1109/ICNS52807.2021.9441549.

[27] S. H. Blumenthal, “Medium Earth Orbit Ka Band Satellite Communications System,” in *MILCOM 2013 - 2013 IEEE Military Communications Conference*, San Diego, CA,

USA, Nov. 2013, pp. 273–277. doi: 10.1109/MILCOM.2013.54.

[28] P. Angeletti, R. De Gaudenzi, and M. Lisi, “From ‘Bent Pipes’ to ‘Software Defined Payloads’: Evolution and Trends of Satellite Communications Systems,” presented at the 26th International Communications Satellite Systems Conference (ICSSC), San Diego, CA, Jun. 2008. doi: 10.2514/6.2008-5439.

[29] B. Azarbad and A. Binti, “DVB-S2 Model in Matlab: Issues and Impairments,” in *MATLAB - A Fundamental Tool for Scientific Computing and Engineering Applications - Volume 2*, V. Katsikis, Ed. InTech, 2012. doi: 10.5772/46473.

[30] K. Leconte, N. Van Wambeke, and H. Gonzalez, “Use of Adaptive Coding and Modulation for aeronautical communications,” in *2010 5th Advanced Satellite Multimedia Systems Conference and the 11th Signal Processing for Space Communications Workshop*, Cagliari, Italy, Sep. 2010, pp. 429–435. doi: 10.1109/ASMS-SPSC.2010.5586855.

[31] M. Smolnikar, T. Javornik, M. Mohorcic, and M. Berioli, “DVB-S2 Adaptive Coding and Modulation for HAP Communication System,” in *VTC Spring 2008 - IEEE Vehicular Technology Conference*, Marina Bay, Singapore, May 2008, pp. 2947–2951. doi: 10.1109/VETECS.2008.309.

[32] “Prospects for the Small Satellite Market,” Euroconsult Report, Apr. 2021.

[33] “Satellites to be Built & Launched by 2030,” Euroconsult Report, Dec. 2021.

[34] “New satellite market forecast anticipates 1,700 satellites to be launched on average per year by 2030 as new entrants and incumbents increase their investment in space,” Dec. 07, 2021. https://www.euroconsult-ec.com/press-release/new-satellite-market-forecast-anticipates-1700-satellites-to-be-launched-on-average-

per-year-by-2030-as-new-entrants-and-incumbents-increase-their-investment-in-space/ (accessed Jun. 08, 2022).

[35] V. S. Chippalkatti, R. C. Biradar, and S. S. Rana, “Recent Technology Trends in Satellite Communication Subsystems,” in *2021 IEEE International Conference on Electronics, Computing and Communication Technologies (CONECCT)*, Bangalore, India, Jul. 2021, pp. 1–5. doi: 10.1109/CONECCT52877.2021.9622696.

[36] C. E. Shannon, “A Mathematical Theory of Communication,” *Bell Syst. Tech. J.*, vol. 27, pp. 379–423, 623–656.

[37] A. J. Jerri, “The Shannon sampling theorem—Its various extensions and applications: A tutorial review,” *Proc. IEEE*, vol. 65, no. 11, pp. 1565–1596, 1977, doi: 10.1109/PROC.1977.10771.

[38] R. G. LYONS, *Understanding digital signal processing*. 3/E. Pearson Education India, 1997.

[39] G. Maral, M. Bousquet, and Z. Sun, *Satellite communications systems: systems, techniques and technology*, 5th ed. Chichester, West Sussex, U.K: John Wiley, 2009.

[40] CCSDS 131.2-B-1, “Recommended Standard: Flexible advanced coding and modulation scheme for high rate telemetry applications,” Mar. 2012.

[41] L. Jordanova, L. Laskov, and D. Dobrev, “Influence of BCH and LDPC Code Parameters on the BER Characteristic of Satellite DVB Channels,” *Eng. Technol. Appl. Sci. Res.*, vol. 4, no. 1, pp. 591–595, Feb. 2014, doi: 10.48084/etasr.394.

[42] ETSI TR 102 376-1 V1.2.1 (2015-11), “Digital Video Broadcasting (DVB); Implementation guidelines for the second generation system for Broadcasting, Interactive Services, News Gathering and other broadband satellite applications; Part 1: DVB-S2.”

[43] CCSDS 131.3-B-1, “CCSDS Space Link Protocols over ETSI DVB-S2 Standard,” 2013.
[44] S. Fasoulas, “Bahnmechanik für Raumfahrzeuge,” Technische Universität Dresden, Apr. 2009.
[45] “ITU-R Recommendations.” https://www.itu.int/pub/r-rec/en (accessed Jun. 08, 2022).
[46] Recommendation ITU-R P.840-6, “Attenuation due to clouds and fog”.
[47] Recommendation ITU-R P.676-9, “Attenuation by atmospheric gases”.
[48] Recommendation ITU-R P.838-3, “Specific attenuation model for rain for use in prediction methods”.
[49] T. Löffler, J. Burgdorf, S. Pätschke, J. Hildebrandt, L. Bötsch-Zavřel, J. Petri, H. Kuhn, M. Lengowski, and S. Klinkner, “Research and Observation in Medium Earth Orbit (MEO) with a cost-effective microsatellite platform,” *72nd Int. Astronaut. Congr. IAC Dubai United Arab Emir.*, 2021.
[50] “Preliminary Radiation Environment Analysis of ROMEO,” Internal Report, Institute of Space Systems, University of Stuttgart, V1.
[51] Recommendation ITU-R P.837-7, “Characteristics of precipitation for propagation modelling”.
[52] T. Löffler, J. Burgdorf, and S. Klinkner, “Orbit-raising strategies for cost-efficient access to lower Medium Earth Orbit without risking space debris,” in *Acta Astronautica*, 2021, vol. 185, pp. 37–41. doi: https://doi.org/10.1016/j.actaastro.2021.04.041.
[53] F. Lacoste, “ITU-R Propagation models software library,” *CNES*, Sep. 2010. https://logiciels.cnes.fr/sites/default/files/usermanual.pdf (accessed Jun. 08, 2022).
[54] International Amateur Radio Union, “Amateur and Amateur-Satellite Service Spectrum.” https://www.iaru.org/wp-

content/uploads/2020/01/Amateur-Services-Spectrum-2020_.pdf (accessed Jun. 08, 2022).

[55] "AD9161 datasheet. 11-Bit/16-Bit, 12 GSPS, RF Digital-to-Analog Converters," *Analog Devices*. https://www.analog.com/media/en/technical-documentation/data-sheets/AD9161-9162.pdf (accessed Jun. 08, 2022).

[56] "EV12DS460AZP datasheet. Commercial and Industrial Grade. Low power 12-bit 6.0Gsps Digital to Analog. Converter 4/2:1 Multiplexer. Datasheet DS1167," *Teledyne e2v*. https://www.e2v.com/resources/account/download-datasheet/4125 (accessed Jun. 08, 2022).

[57] "Vorago M4 datasheet. VA41620 – Radiation Hardened Arm® Cortex®-M4 w/ FPU MCU," *Vorago Technologies*. https://www.voragotech.com/products/va41620 (accessed Jun. 08, 2022).

[58] "Using lvaux mode in xq ruggedized ultrascale+ devices for airborne systems," 2019. https://www.xilinx.com/support/documentation/user guides/ug584- xq-lvaux-mode.pdf (accessed Jun. 08, 2022).

[59] N. Franconi, S. Sabogal, A. George, M. Hassouneh, J. Mitchell, and C. Wilson, "A Novel RF Architecture for Simultaneous Communication, Navigation, and Remote Sensing with Software-Defined Radio," *Small Satell. Conf. SSC20-WKVIII-02*.

[60] "Zynq-7000 SoC Datasheet: Overview," *Xilinx*. https://www.mouser.com/datasheet/2/903/ds190-Zynq-7000-Overview-1595492.pdf (accessed Jun. 08, 2022).

[61] CCSDS 130.12-G-1, "CCSDS Protocols over DVB-S2— Summary of Definition, Implementation, and Performance," 2016.

[62] “IPrium DVB-S2 modulator core.” https://www.iprium.com/bins/pdf/iprium_ug_dvbs2_modulator.pdf (accessed Jun. 08, 2022).
[63] “ADALM-PLUTO datasheet,” *Analog Devices*. https://www.analog.com/en/design-center/evaluation-hardware-and-software/evaluation-boards-kits/ADALM-PLUTO.html#eb-overview (accessed Jun. 08, 2022).
[64] “DVB-S2/S/S2X/T/T2/C/C2 Single-Tuner, USB Multi-standard-tuner Empfangsbox, TBS-5520 SE,” *TBS-Technology*. https://tbs-technology.de/shop/DVB-S2-S-S2X-T-T2-C-C2-Single-Tuner-USB-Multi-standard-tuner-Empfangsbox-TBS-5520-SE (accessed Jun. 08, 2022).
[65] “AD9122 datasheet. Dual, 16-Bit, 1230 MSPS, TxDAC+ Digital-to-Analog Converter,” *Analog Devices*. https://www.analog.com/media/en/technical-documentation/data-sheets/AD9122.pdf (accessed Jun. 08, 2022).
[66] “AD9142 datasheet. Dual, 16-Bit, 1600 MSPS, TxDAC+ Digital-to-Analog Converter,” *Analog Devices*. https://www.analog.com/media/en/technical-documentation/data-sheets/AD9142.pdf (accessed Jun. 08, 2022).
[67] “AD9146 datasheet. Dual, 16-Bit, 1230 MSPS, TxDAC+ Digital-to-Analog Converter,” *Analog Devices*. https://www.analog.com/media/en/technical-documentation/data-sheets/AD9146.PDF (accessed Jun. 08, 2022).
[68] “AD9783 datasheet. Dual 12-/14-/16-Bit, LVDS Interface, 500 MSPS DACs,” *Analog Devices*. https://www.analog.com/media/en/technical-documentation/data-sheets/AD9780_9781_9783.pdf (accessed Jun. 08, 2022).
[69] “HMC8191 datasheet. 6 GHz to 26.5 GHz, Wideband I/Q Mixer,” *Analog Devices*. https://www.analog.com/media/en/technical-

documentation/data-sheets/hmc8191.pdf (accessed Jun. 08, 2022).

[70] "HMC1056 datasheet. GaAs MMIC I/Q Mixer 8-12 GHz," *Analog Devices*. https://www.analog.com/media/en/technical-documentation/data-sheets/hmc1056.pdf (accessed Jun. 08, 2022).

[71] "ADRF6780 datasheet. 5.9 GHz to 23.6 GHz, Wideband, Microwave Upconverter," *Analog Devices*. https://www.analog.com/media/en/technical-documentation/data-sheets/ADRF6780.pdf (accessed Jun. 08, 2022).

[72] "NCR2-123 datasheet. 1:2 LTCC Transformer, 4700 - 1200 MHz," *Mini-Circuits*. https://www.minicircuits.com/pdfs/NCR2-123+.pdf (accessed Jun. 08, 2022).

[73] "ADRF6780-EVALZ Evaluation Board User Guide UG-920," *Analog Devices*. https://www.analog.com/media/en/technical-documentation/user-guides/ADRF6780-EVALZ_UG-920.pdf (accessed Jun. 08, 2022).

[74] "LMX2594 datasheet. 15-GHz wideband PLLatinum™ RF synthesizer with phase synchronization and JESD204B support," *Texas Instruments*. https://www.ti.com/lit/ds/symlink/lmx2594.pdf?ts=1648715966694&ref_url=https%253A%252F%252Fwww.google.com%252F (accessed Jun. 08, 2022).

[75] "SG5032VAN Crystal Oscillator (SPXO) datasheet," *Seiko Epson Corporation*. https://support.epson.biz/td/api/doc_check.php?dl=brief_SG3225EAN_en.pdf (accessed Jun. 08, 2022).

[76] "Si53306 datasheet. 1:4 Low-Jitter Universal Buffer/Level Translator," *Silicon Labs*. http://www.silabs.com/documents/public/data-sheets/Si53306.pdf (accessed Jun. 08, 2022).

[77] “Solid state power amplifiers 101,” Feb. 2017. https://www.satelliteevolutiongroup.com/articles/amplifier-technology.pdf (accessed Jun. 08, 2022).
[78] A. Pandey, *Practical microstrip and printed antenna design*. Artech House, 2019.
[79] L. Bötsch, “Development of a Patch-Array Antenna in the Amateur Radio X-Band for Small Satellite Applications.” Master Thesis IRS-20-S-098, University of Stuttgart, Institute of Space Systems, Dec. 2020.
[80] “Zedboard Product Brief (Datasheet),” *Avnet*, Apr. 2022. https://www.avnet.com/wps/portal/us/products/avnet-boards/avnet-board-families/zedboard/ (accessed Jun. 08, 2022).
[81] P. Keil, “Implementierung und Verifikation des adaptiven DVB-S2 Standards für eine MEO-Mission.” Bachelor Thesis, University of Stuttgart, Institute of Telecommunications, Jun. 2020.
[82] “SDRangel SDR and signal analyzer tool product description,” Apr. 2022. https://www.sdrangel.org/ (accessed Jun. 08, 2022).
[83] “ESA HDL IP Cores Portfolio Overview.” https://www.esa.int/Enabling_Support/Space_Engineering_Technology/Microelectronics/ESA_HDL_IP_Cores_Portfolio_Overview (accessed Jun. 08, 2022).
[84] CCSDS 131.0-B-3, “TM Synchronization and Channel Coding,” *Blue Book*, 2017.
[85] L. Kramer, “Entwicklung eines X-Band Transmitter-Frontends für Satellitenanwendungen.” Master Thesis, University of Stuttgart, Institute of Robust Power Semiconductor Systems, 2018.
[86] “Intel MAX 10 FPGA Device Datasheet,” *Intel Cooperation*, Apr. 2022. https://d2pgu9s4sfmw1s.cloudfront.net/DITA-technical-publications/PROD/PSG/m10_datasheet-683794-666319.pdf (accessed Jun. 08, 2022).

[87] “DAC081S101 datasheet. 8-Bit Micro Power Digital-to-Analog Converter with Rail-to-Rail Output,” *Texas Instruments*. https://www.ti.com/lit/ds/symlink/dac081s101.pdf?ts=1651766053862&ref_url=https%253A%252F%252Fwww.google.com%252F (accessed Jun. 08, 2022).

[88] “142-0761-881 datasheet. High frequency end launch SMA jack assembly, PC mount, 10 mil pin,” *Cinch Connectivity Solutions*. https://www.belfuse.com/product/part-details?partn=142-0761-881 (accessed Jun. 08, 2022).

[89] M. A. Boettcher, K. Leidig, S. Klinkner, Y.-C. Chak, S. Pätschke, A. S. Mohd, and H. Salim, “Design of a low-cost S/X dual band satellite ground station for small satellite missions,” presented at the IAA 2020.

[90] P. V. R. Ferreira, R. Paffenroth, A. M. Wyglinski, T. M. Hackett, S. G. Bilen, R. C. Reinhart, and D. J. Mortensen, “Multiobjective Reinforcement Learning for Cognitive Satellite Communications Using Deep Neural Network Ensembles,” *IEEE J. Sel. Areas Commun.*, vol. 36, no. 5, pp. 1030–1041, May 2018, doi: 10.1109/JSAC.2018.2832820.

[91] P. V. R. Ferreira, R. Paffenroth, A. M. Wyglinski, T. M. Hackett, S. G. Bilen, R. C. Reinhart, and D. J. Mortensen, “Reinforcement Learning for Satellite Communications: From LEO to Deep Space Operations,” *IEEE Commun. Mag.*, vol. 57, no. 5, pp. 70–75, May 2019, doi: 10.1109/MCOM.2019.1800796.

[92] L. Bötsch-Zavřel, private communication

Appendices

A.DVB-S2

Table A-1: MODCOD (MCD) numbers according to the modulation and coding combination of [3] with its corresponding Spectral Efficiency (SE) as user bits per symbol and required E_b/N_0 for quasi-error-free transmission for normal frame length

MCD	Modulation & code rate	SE [-]	E_b/N_0 [dB]
1	QPSK ¼	0.49	0.746
2	QPSK 1/3	0.656	0.588
3	QPSK 2/5	0.789	0.277
4	QPSK 1/2	0.989	1.049
5	QPSK 3/5	1.188	1.481
6	QPSK 2/3	1.322	1.887
7	QPSK ¾	1.487	2.306
8	QPSK 4/5	1.587	2.674
9	QPSK 5/6	1.655	2.993
10	QPSK 8/9	1.766	3.729
11	QPSK 9/10	1.789	3.895
12	8PSK 3/5	1.778	2.996
13	8PSK 2/3	1.981	3.652
14	8PSK ¾	2.228	4.431
15	8PSK 5/6	2.479	5.408
16	8PSK 8/9	2.646	6.464
17	8PSK 9/10	2.679	6.7

18	16PSK 2/3	2.637	4.759
19	16APSK 3/4	2.967	5.487
20	16APSK 4/5	3.166	6.025
21	16APSK 5/6	3.3	6.425
22	16APSK 8/9	3.523	7.421
23	16APSK 9/10	3.567	7.607
24	32APSK 3/4	3.703	7.044
25	32APSK 4/5	3.952	7.672
26	32APSK 5/6	4.12	8.132
27	32APSK 8/9	4.398	9.258
28	32APSK 9/10	4.453	9.563

B. List of software tools

Table B-1: Software tools description

Software	Version	Software Vendor
MATLAB	R2022a	Mathworks
MATLAB is a programming and numeric computing platform. MATLAB features several toolboxes specific for digital signal processing. Furthermore, different functions to analyze the atmospheric loss according to the ITU recommendations [46]–[48], [51] are available.		
Simulink	R2022a	Mathworks
Simulink is an add-on simulator from MATLAB that can be used without writing code. Simulink is based on a block diagram environment. The Simulink tool is used for evaluation of the PA module.		
ASTOS		ASTOS Solutions
ASTOS is a specific tool for space applications. Among others, it provides features for trajectory optimization, visibility, eclipse and coverage analysis, among others. ASTOS is used for the ground station visibility and contact times for the ground stations of the IRS network.		
PROPA	DLL_2017	CNES
PROPA is a Dynamic Link Library (DLL) from CNES to compute propagation losses for Earth to Space (or viceversa) transmission links. It contains functions based on the ITU Recommendation models [46]–[48], [51].		
Vivado	2018.3	AMD Xilinx
The Vivado Design Suite is a development environment for SoCs and FPGAs in order to ease system-level integration and implementation. Vivado was used to implement the digital signal processing, mainly the DVB-S2 and the CCSDS PTME IP core.		

Altair Feko		Altair
Altair Feko is a high frequency electromagnetic simulation tool which was used for the simulation of the patch (array) antennas. Feko provides numerous solvers that can be used depending on the application. These include the method of moments (MOM), multilevel fast multipole method (MLFMM), the finite element method (FEM), the uniform theory of diffraction (UTD) and physical optics (PO). For the simulations for this thesis, the MOM, which is the basic solver of Feko, was chosen. Since the simulated structure was not electrically large, it provided sufficient available resources (i.e. platform memory, time) to solve the simulation.		

C. PROPA functions and parameters

Table C-1: Description of the input and the output of the PROPA functions, based on [53]

A_{gas}	
Input	Frequency (GHz) Elevation (radians) Temperature (K) Water vapor density (g/m^3)
Output	Atmospheric gas attenuation (dB)
Comment	Frequency $\leq$ 350 GHz Elevation $\geq$ 5°
A_{rain}	
Input	Latitude (°) Frequency (GHz) Elevation (radians) Unavailability (%) Station height (km) Rain height (km) Rain intensity exceeded for the unavailability of an average year (mm/h) Tilt angle (°)
Output	Rain attenuation (dB) exceeded for the unavailability of an average year
Comment	Frequency $\leq$ 55 GHz 0.001 $\leq$ Unavailability $\leq$ 5%
A_{cloud}	
Input	Frequency (GHz) Elevation (radians) Total columnar content of liquid water (kg/m^2)
Output	Clouds attenuation (dB) exceeded for the unavailability of an average year
Comment	Frequency $\leq$ 200 GHz 1% $\leq$ Unavailability $\leq$ 50%

A_{scint}	
Input	Wet term of refraction co-index Frequency (GHz) Elevation (radians) Unavailability (%) Station height (km) Antenna efficiency Antenna diameter (m)
Output	Scintillation attenuation (dB) exceeded for the unavailability of an average year
Comment	7 GHz $\leq$ Frequency $\leq$ 20 GHz Elevation $\geq 4^{\circ}$ 0.01 $\leq$ Unavailability $\leq$ 50% 0 $\leq$ Antenna efficiency $\leq$ 1

D. Detailed link budgets

In the following table the corresponding worst cases for the ground stations STR and MAL are calculated for the maximum link range (of the ROMEO mission) that allows a margin of minimum 3 dB. For this, an availability of 99.9% is considered as well as the different ITU models presented in 2.5.2. It can be clearly seen that the STR ground station can close the link for the whole mission (the link range corresponds to an altitude of 3025 km and an elevation of 5°) while the MAL ground station can only support the mission for a link range up to 1730 km. Thus, the STR ground station acts as the anchor ground station while the MAL ground station acts as a support ground station. Yet, the difference in the atmospheric loss of both ground stations will allow to test the performance and effectiveness of the ACM control loop.

Table D-1: Detailed link budgets for the ground stations STR and MAL

Parameter	**STR**	**MAL**
Availability [%]	99.90	99.90
Transmitter parameters		
Rolloff [-]	0.20	0.20
Downlink frequency [GHz]	10.475	10.475
Antenna gain [dBi]	16.00	16.00
Transmission loss [dB]	1.00	1.00
Transmitter power (saturation) [dBW]	3.00	3.00
OBO [dB]	2.00	2.00
Downlink EIRP (saturation) [dBW]	18.40	18.40
Downlink EIRP (backoff) [dBW]	16.40	16.40
Downlink propagation		
Link range [km]	6375.70	1730.00
Free space loss [dB]	188.94	177.61
Gaseous attenuation [dB]	0.14	0.18
Cloud attenuation [dB]	0.29	0.75

Atmospheric scintillation [dB]	0.42	0.85
Rain attenuation [dB]	3.91	15.28
Total atmospheric loss [dB]	4.35	16.24
Total loss [dB]	193.29	193.85
Receiving ground station		
Northern latitude [°]	48.75	2.84
Eastern longitude [°]	9.10	101.51
Height above sea level [km]	0.44	0.00
Antenna diameter [m]	4.50	4.50
Antenna gain [dBi]	52.32	52.32
Effective Noise Temperature, clear sky [K]	285.00	285.00
G/T, clear sky [dB/K]	27.80	27.80
C/N0 [dBHz]	78.53	77.90
Bandwidth and system margin		
Modulation	QPSK	QPSK
Coding	¼	¼
Spectral efficiency [-]	0.49	0.49
Symbol rate [Msps]	41.55	41.55
Bit rate [Mbps]	20.36	20.36
Bandwidth [MHz]	49.86	49.86
Eb/N0 [dB]	5.44	4.81
Eb/N0 required [dB]	0.75	0.75
Implementation loss [dB]	1.00	1.00
Degradation loss [dB]	1.00	1.00
Pointing loss [dB]	1.00	1.00
Margin [dB]	**3.70**	**3.07**

E. Antenna simulations results

Microstrip patch antennas consist of a metallic radiation patch that can be printed on a grounded substrate or be suspended above a ground plane. The patches can have different geometries, like for example a rectangle, a triangle, a disk, a ring, etc. The patch material must be electrically conducting. The substrate consists of low dielectric constant materials and high thickness to achieve maximum radiation, better efficiency and larger bandwidths.

The microstrip patch radiates form fringing fields at its edges as shown in the following figure. The patch is excited by the feed which establishes a charge distribution between the ground plane (negative charge) and the patch (positive charge). The microstrip patch antennas are characterized by the patch length, the patch width, the input impedance, the gain and the radiation characteristics. The patch length L of a patch with a rectangular geometry is typically $0.3\lambda_0 < L < 0.5\lambda_0$, where λ_0 is the free-space wavelength. The patch's thickness is typically $t << \lambda_0$ and the height h of the dielectric substrate is typically $0.003\lambda_0 \leq h \leq 0.05\lambda_0$. Typical dielectric constant values ϵ_r for the substrate are $2.2 \leq \epsilon_r \leq 12$. The more loosely bound the fields around the patch are, the more efficient the radiation is, and the larger the bandwidth is. The lower the dielectric constant and the thicker the substrate, the more loosely bound the fields around the patch are, and the more efficient the radiation is, and the larger the bandwidth is. The element size, on the other hand, increases [78].

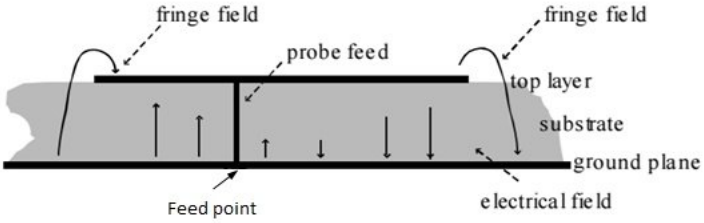

Figure E-1: Microstrip patch antenna layout [78]

For a single patch antenna, two types were compared and simulated in Altair Feko: a truncated patch and an almost-square patch. These patches create circular polarization by their shape: The truncated patch achieves circular polarization by introducing truncations on two opposite corners of the patch and the almost square patch by increasing slightly the patch length compared to the patch width. For the feeding concept, a microstrip line feed and a coaxial feed were considered. The microstrip line feed is an electrically conducting metallic strip that connects directly the patch with a power source. Microstrip line feeds are easy to fabricate and to model but cause undesired cross polarization due to spurious feed radiation. When using a coaxial feed, the outer conductor is connected to the ground plane and the inner conductor is soldered to the radiating patch. The coaxial feeds have less spurious radiation but they are difficult to model and require soldering which could cause disturbances.

The truncated patch antenna matched the requirements better than the almost square patch. After selecting a single patch antenna type, different patch array antenna types were simulated and compared with the different feeding methods. First, a 2x2 array was simulated with coaxial feeding for each path and then increased to an 2x4 array. The same procedure was applied for the microstrip feeding concept. The microstrip feeding concept fed by a single coaxial link achieved the best

performance according to the requirements in *Table 4-1*. A maximum boresight gain of 14.5 dB was achieved in the left-hand polarized direction over the entire frequency range, and the difference from the right-hand polarized direction was between 16.77 dBi and 19.54 dBi. The XPD was always in the range of 20 dB. The 4x4 patch array antenna with microstrip feeding concept achieved a maximum boresight of 16.7 dBi. However, the XPD was reduced to ca. 15 dB. This lower XPD value compared to the 2x4 microstrip line feed configuration can be explained by the cross-coupling of the numerous coaxial feeds which interact via the ground plane.

Overall, the simulations showed that it is feasible to use a patch array antenna for the ROMEO mission. Yet, the achieved gain figures in the simulations are smaller than the calculated gain figures. This is due to possible cross coupling between patches and mismatch. This must be considered since part of the RF power is sent with the wrong polarization. However, further simulations are necessary to better understand the performance of the patch array and to simulate the RF matching between the PA module and the patch array antenna. The further simulations, development, functional testing as well as environmental tests like thermal-vacuum tests for the patch array antenna will be further investigated in another PhD thesis.

The following figures show the simulation results for the investigated patch array antennas configurations [92], which were based on [79]. *Figure E-3* shows the LHCP and RHCP gain for a center frequency of 10.475 GHz.

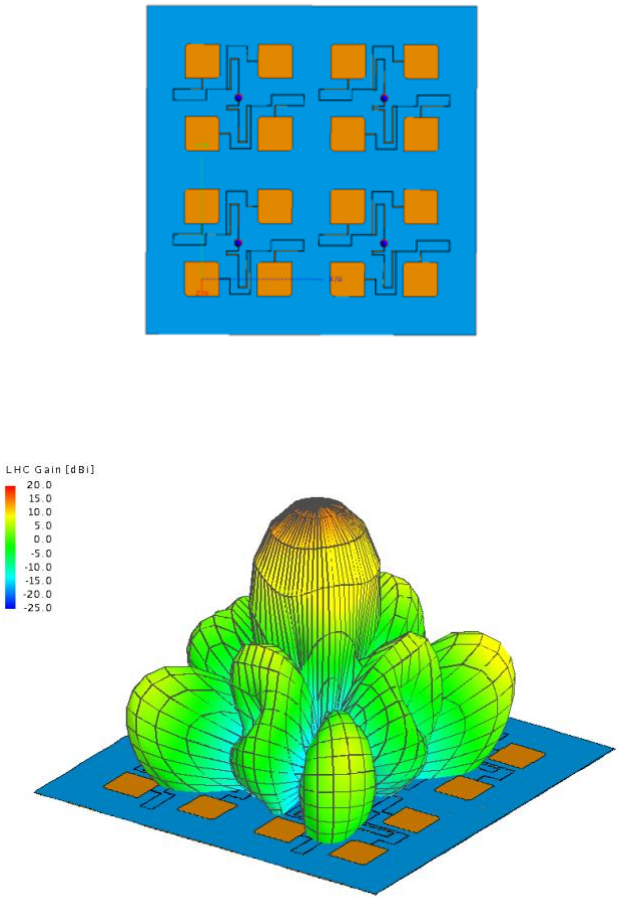

Figure E-2: Feko model of the 4x4 array with microstrip line feeding. The element-spacing is 0.5λ and the array was simulated for the center frequency of 10.475GHz (upper panel) and its radiation pattern (lower panel) [92]

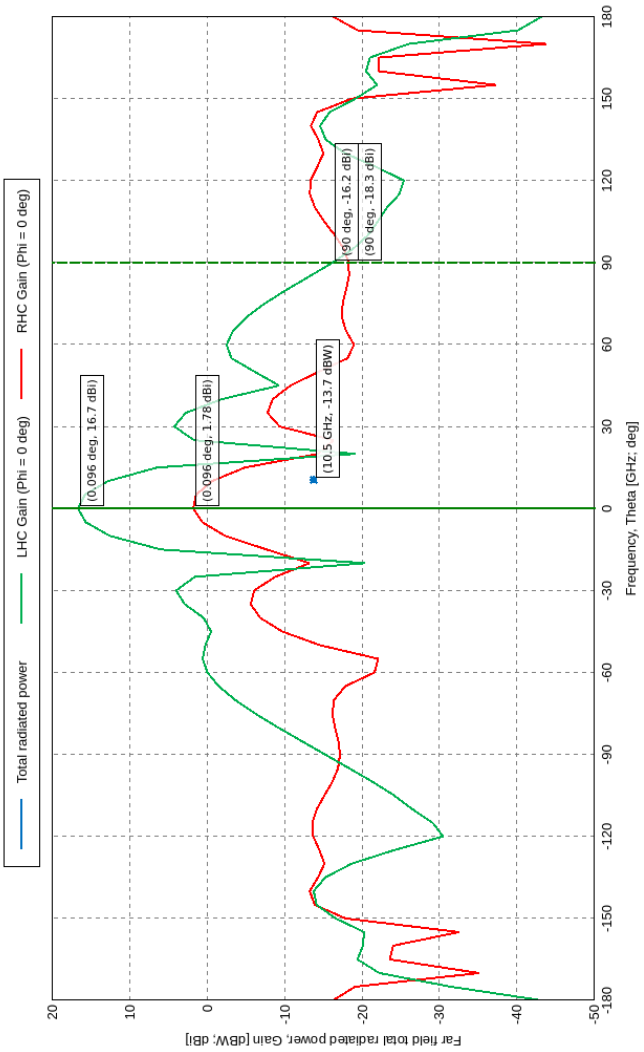

Figure E-3: LHCP and RHCP gain at the center frequency of 10.475GHz [92]

F. Circuit diagrams of the analogue frontend prototype

All the circuit diagrams of the analogue frontend prototype where done during a master thesis and are taken from [83].

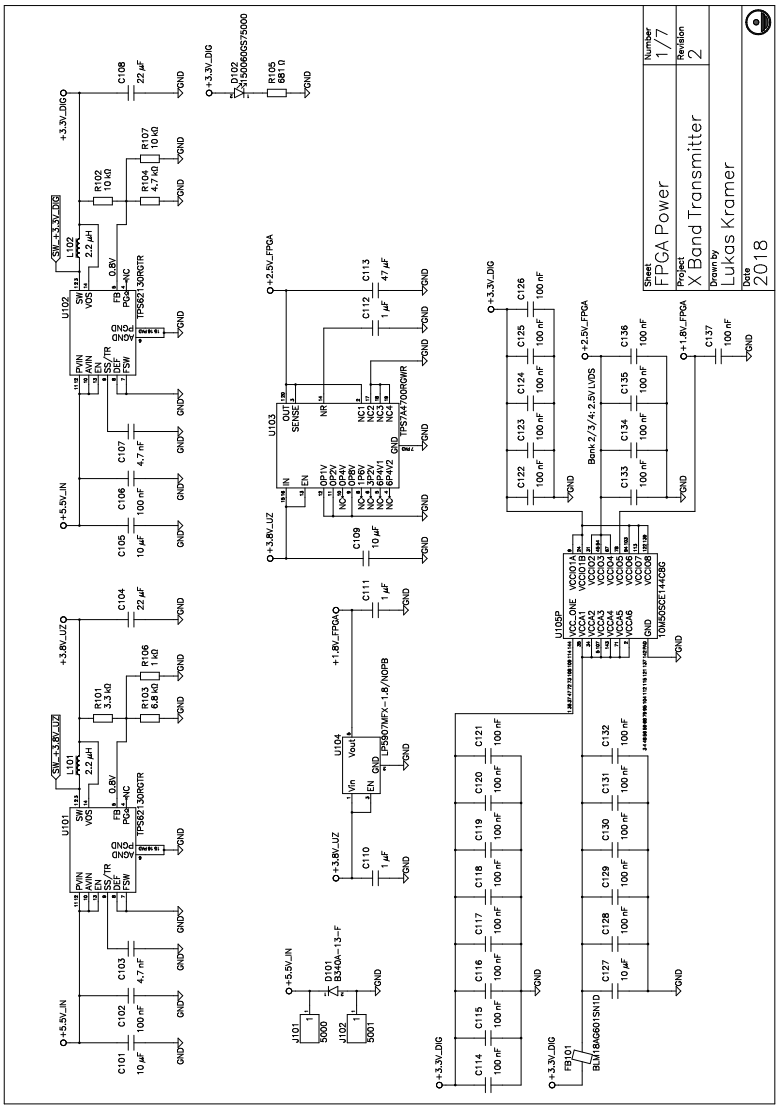
Sheet
FPGA Power
Number
1/7
Project
X Band Transmitter
Revision
2
Drawn by
Lukas Kramer
Date
2018

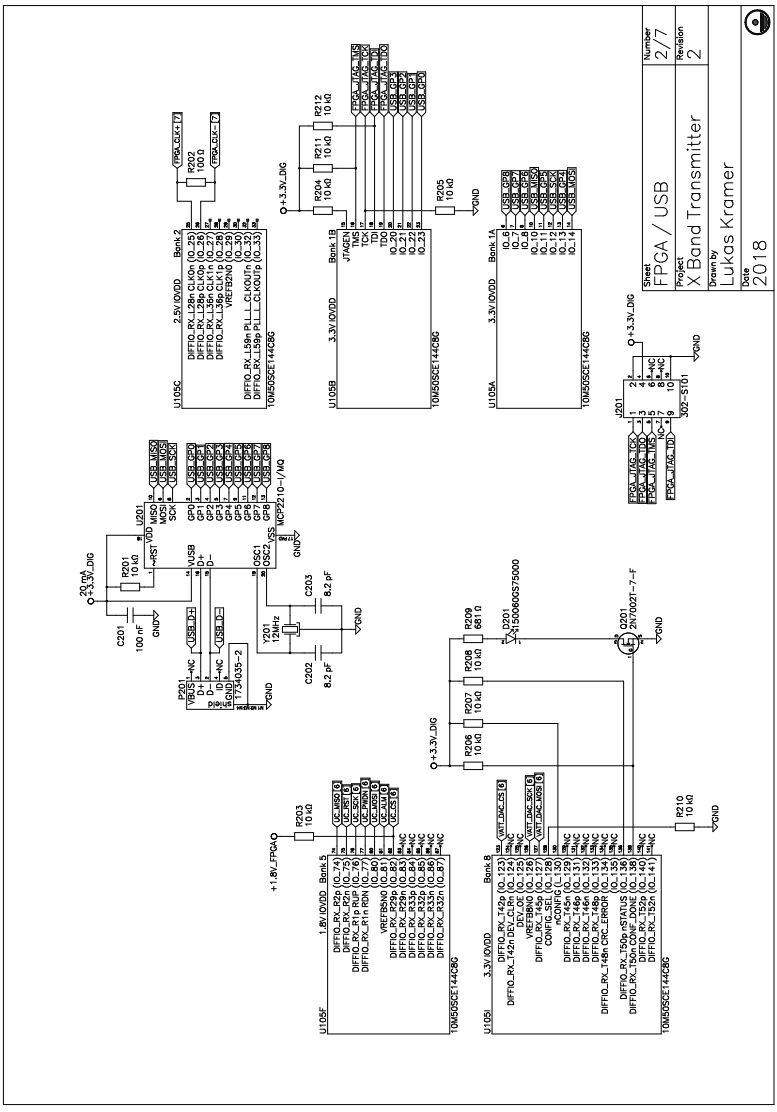
Sheet
FPGA / USB
Number
2/7
Project
X Band Transmitter
Revision
2
Drawn by
Lukas Kramer
Date
2018

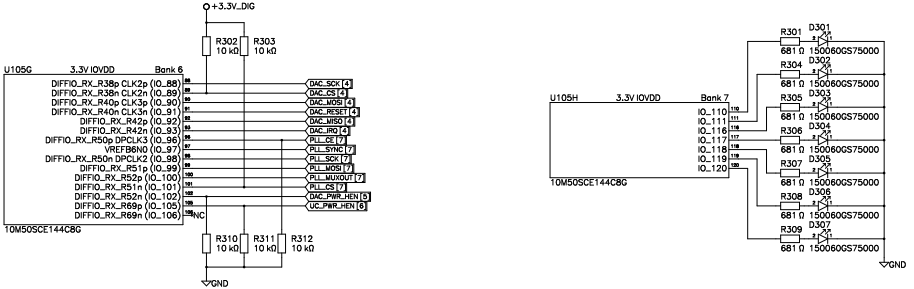

Sheet: FPGA	Number: 3/7
Project: X Band Transmitter	Revision: 2
Drawn by: Lukas Kramer	
Date: 2018	

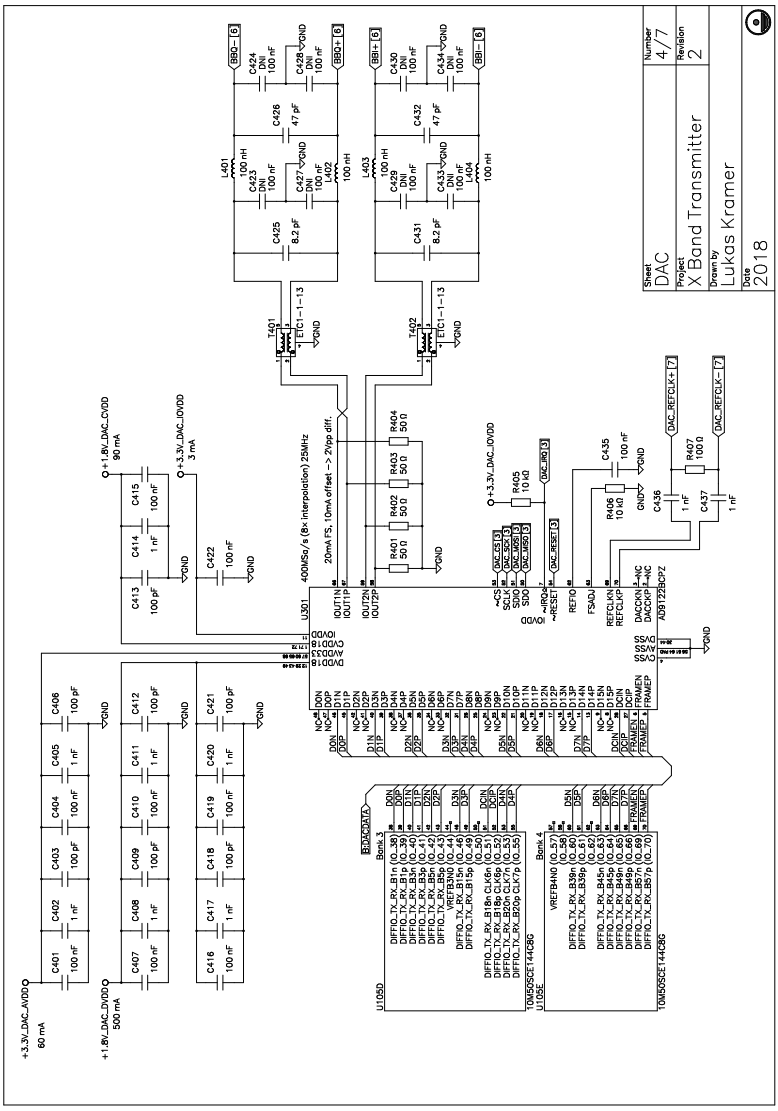
Sheet
DAC
Number
4/7
Project
X Band Transmitter
Revision
2
Drawn by
Lukas Kramer
Date
2018

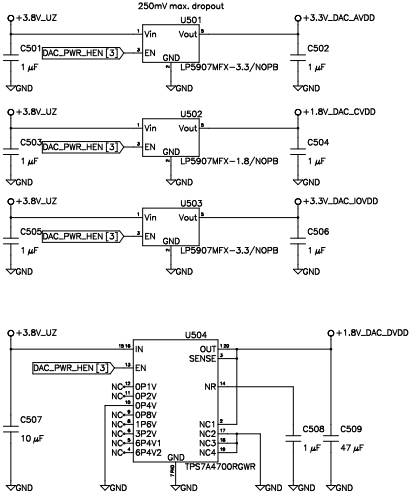

Sheet: DAC power	Number: 5/7
Project: X Band Transmitter	Revision: 2
Drawn by: Lukas Kramer	
Date: 2018	

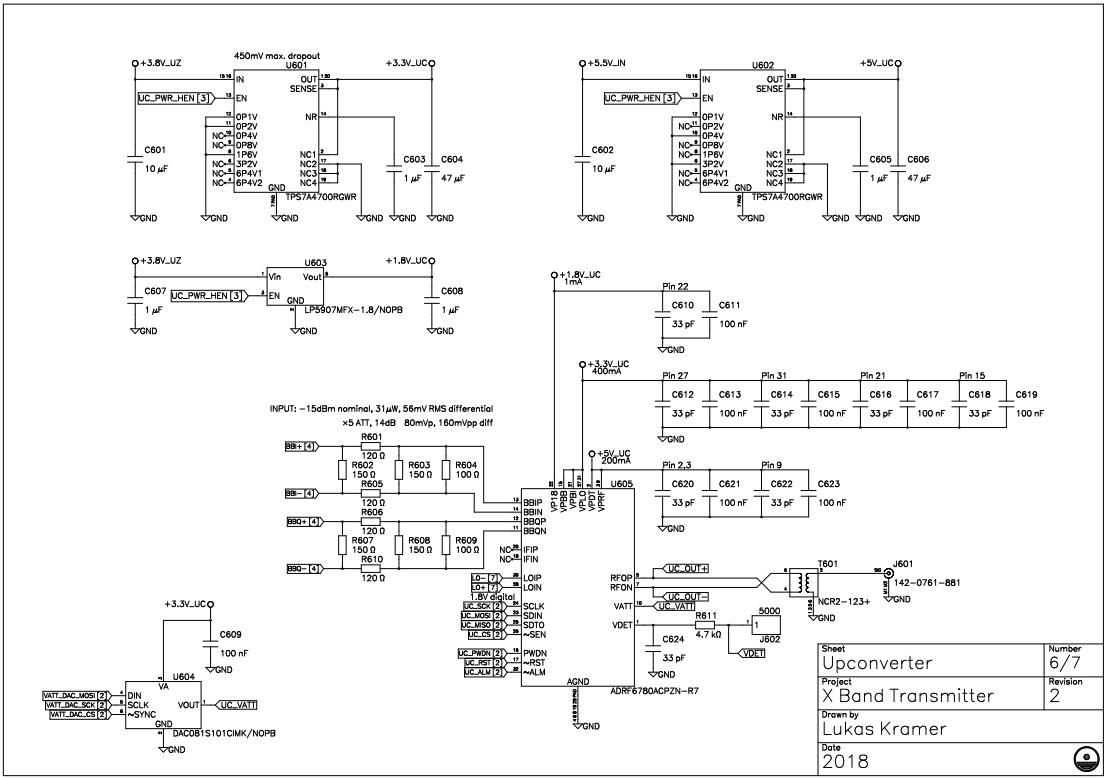

Sheet: Upconverter	Number: 6/7
Project: X Band Transmitter	Revision: 2
Drawn by: Lukas Kramer	
Date: 2018	

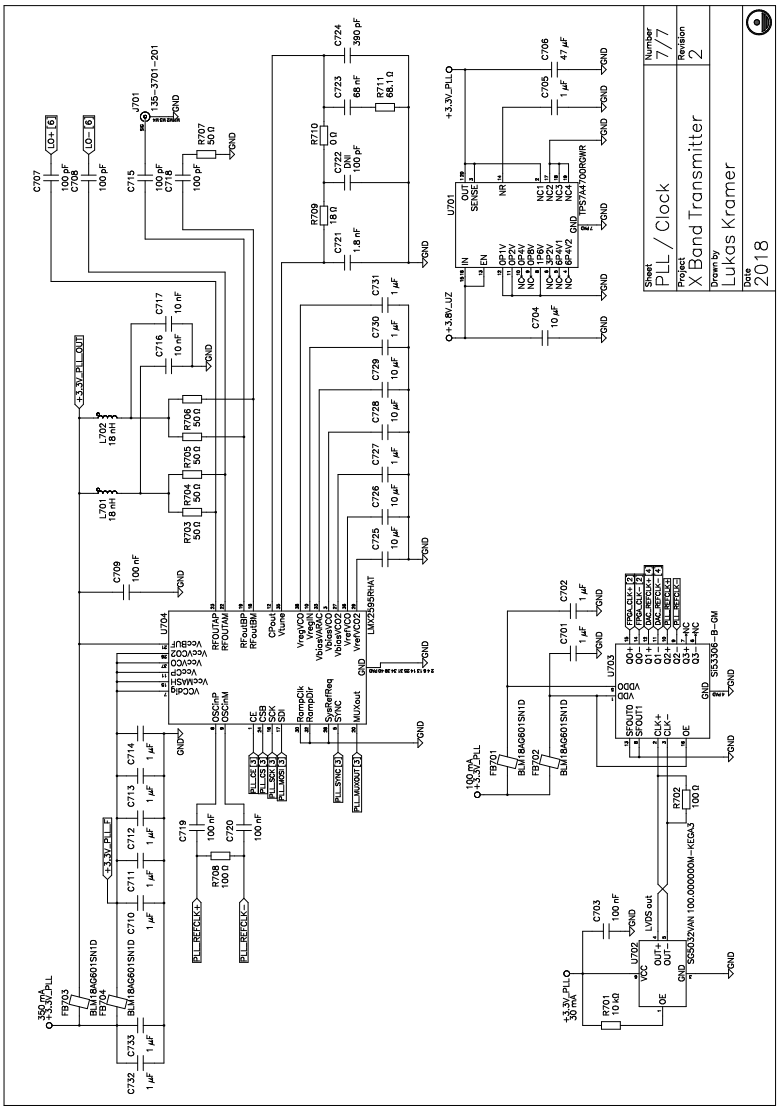
Sheet
PLL / Clock
Number
7/7
Project
X Band Transmitter
Revision
2
Drawn by
Lukas Kramer
Date
2018

G. PA module simulations

The PA module simulations were conducted with Simulink, which is an add-on simulator of MATLAB. The following simplifications were made in order to simplify the simulations:

- The PA module was modelled as a discrete time system despite being an analogue circuit
- The quantization noise of the DAC is modelled with the AWGN block
- The DVB-S2 signal is represented only with the modulation scheme

The parameters of the pre-amplifier were set to the datasheet parameters of the NBB-300 amplifier and of the parameters of the driver amplifier were set to the datasheet parameters of the QPA2610 amplifier. The block diagram for the simulation can be found in Figure G-1 and the parameters that were used for the Simulink simulations can be found in *Table G-1*.

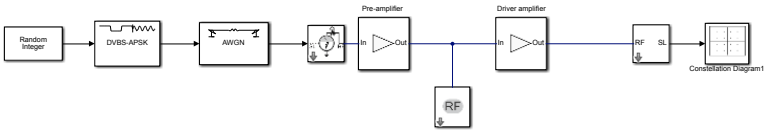

Figure G-1: Simulink model for 16APSK and 32APSK including a pre-amplifier and a driver amplifier. To simulate a QPSK or 8PSK modulation scheme, the DVBS-APSK block is replaced with the corresponding QPSK and 8PSK block

Table G-1: Parameter values of the pre-amplifier and the driver amplifier as simulated with Simulink

Parameter	**Value**
Pre-amplifier	
Gain [dB]	9.5
IP3 [dBm]	27.1
Input impedance [Ohm]	50
Output impedance [Ohm]	50
Driver amplifier	
Gain [dB]	23.5
IMD3 [dBc]	-15
Input impedance [Ohm]	50
Output impedance [Ohm]	50

To minimize the EVM of the PA module, the baseband signal processing technique DPD was used. DPD is based on a memory polynomial which corrects the nonlinearities of the PA. Since the PA module characteristics will vary over time and operating conditions, an adaptive DPD testbench was implemented. With an adaptive DPD design, a DPD coefficient estimator samples the PA input and output in order to perform matrix computations to derive a set of DPD coefficients. The DPD coefficient estimator applies these coefficients to the DPD memory polynomial and outputs a predistorted signal. The algorithm used in this design, the recursive least square algorithm, requires a feedback loop to estimate the error. The error is the difference between the estimated PA input and the measured PA input, which the algorithm attempts to drive to zero. This leads to the best estimate of the DPD coefficients. However, the benefit of fast convergence comes at the cost of high computational power.

In *Table G-2* the parameters and their corresponding values for the DPD coefficient estimator used in the Simulink simulation are shown.

Table G-2: Parameter values of the DPD coefficient estimator as simulated with Simulink

Parameter	**Value**
Desired amplitude gain [dB]	33
Polynomial type	Memory polynomial
Degree	3
Memory depth	5
Algorithm	Recursive least squares
Source of forgetting factor	Property
Forgetting factor	0.999
Initial coefficient estimate	-

In order to account for the DPD technique, the block diagram presented in Figure G-1 had to be expanded with the DPD technique. Figure G-2 shows the block diagram including the DPD feedback loop consisting of the DPD coefficient estimator block as well as block called “DPD” that applies the estimated coefficients from the estimator block and outputs a predistorted signal.

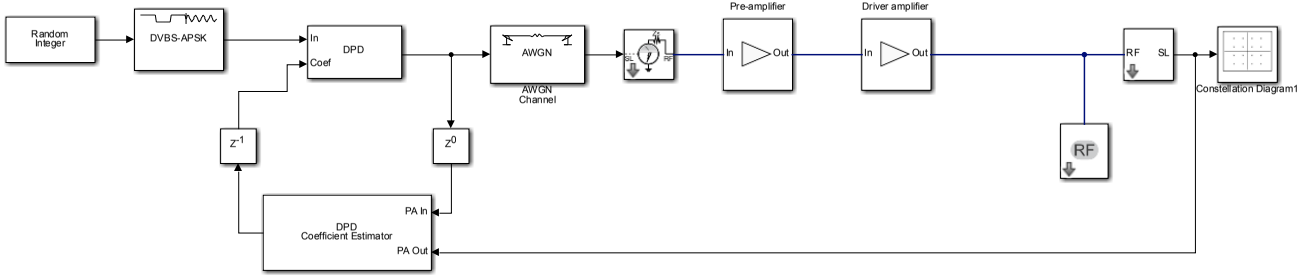

Figure G-2: Simulink model for 16APSK and 32APSK including a pre-amplifier and a driver amplifier and the DPD block. To simulate a QPSK or 8PSK modulation scheme, the DVBS-APSK block is replaced with the corresponding QPSK and 8PSK block

The following figures compare the EVM of a QPSK and a 32APSK signal with and without the use of a DPD algorithm.

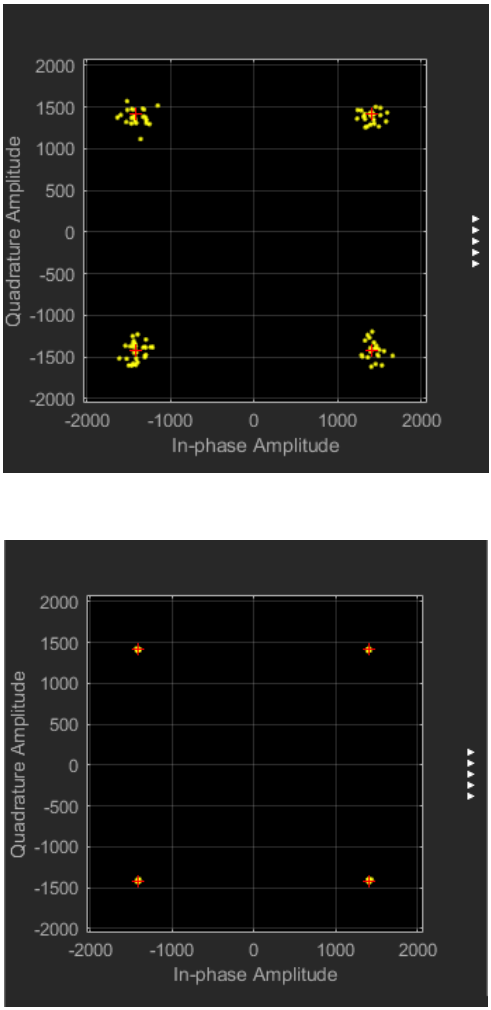

Figure G-3: Comparison of a QPSK modulated signal with an attenuation of 10 dB without (left panel) and with (right panel) the use of a DPD algorithm. The EVM without DPD is 9.7% and with DPD 0.4%

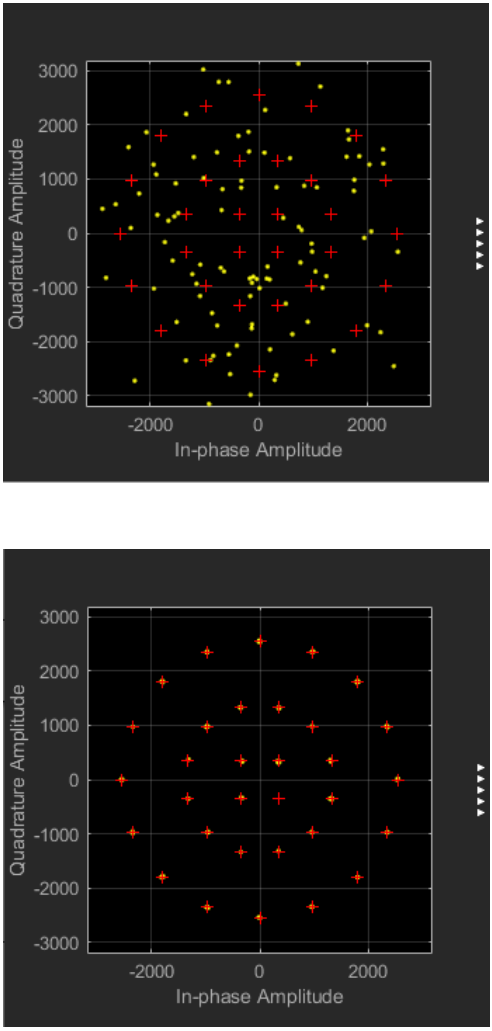

Figure G-4: Comparison of a 32APSK modulated signal with an attenuation of 10 dB without (left panel) and with (right panel) the use of a DPD algorithm. The EVM without DPD is 20.4% and with DPD 0.8%

In the following table the results for the Simulink analysis of a QPSK and a 32APSK signal with and without the adaptive DPD algorithm are shown. The term attenuation refers to the decreased value of the AWGN block that is included in the block diagram without and with DPD. This should reflect the introduction of quantization noise of the DAC. Thus, the higher the introduced attenuation, the higher the EVM value measured after the PA module which would difficult the reception at the on-ground receiver. In general, it can be clearly seen that the DPD algorithm significantly improves the EVM, for example reducing the EVM for a QPSK signal from 23.5 % to 0.7 % when using an attenuation of 20 dB.

Table G-3: Results of the Simulink analysis for the PA module. The EVM is shown for the baseline with a variable gain pre-amplifier and a driver amplifier without DPD and with DPD. The attenuation corresponds to the values of the AWGN block included in the block diagram

Attenuation	**Baseline EVM [%]**		**DPD EVM [%]**	
	QPSK	**32APSK**	**QPSK**	**32APSK**
0 dB	3.3	6.8	0.4	0.6
10 dB	9.7	20.4	0.4	2.8
20 dB	23.5	63.7	0.7	6.9